UNIVERSITY OF GAZİANTEP
GRADUATE SCHOOL OF
NATURAL & APPLIED SCIENCES

THERMAL GRADIENTS IN CONCRETE BOX GIRDERS

M. Sc. THESIS
IN
CIVIL ENGINEERING

BY
SALIH KHUDAIR AL-REBEH

NOVEMBER 2014

Thermal Gradients in Concrete Box Girders

M.Sc. Thesis
In
Civil Engineering
University of Gaziantep

Supervisor
Prof. Dr. Mustafa ÖZAKÇA

By
Salih Khudair AL-REBEH

November 2014

REPUBLIC OF TURKEY
UNIVERSITY OF GAZİANTEP
GRADUATE SCHOOL OF NATURAL & APPLIED SCIENCES
CIVIL ENGINEERING DEPARTMENT

Name of the thesis: Thermal gradients in concrete box girders

Name of the student: Salih Khudair AL-REBEH

Exam date: November 21, 2014

Approval of the Graduate School of Natural and Applied Sciences

Prof. Dr. Metin BEDIR
Director

I certify that this thesis satisfies all the requirements as a thesis for the degree of Master of Science.

Prof. Dr. Mustafa GÜNAL
Head of Department

This is to certify that we have read this thesis and that in our opinion it is fully adequate, in scope and quality, as a thesis for the degree of Master of Science.

Prof. Dr. Mustafa ÖZAKÇA
Supervisor

Examining Committee Members	Signature
Prof. Dr. Mustafa ÖZAKÇA	....
Assist. Prof. Dr. Nildem TAYŞI	....
Assist. Prof. Dr. Ömer Yavuz BOZKURT	....

I hereby declare that all information in this document has been obtained and presented in accordance with academic rules and ethical conduct. I also declare that, as required by these rules and conduct, I have fully cited and referenced all material and results that are not original to this work.

Salih Khudair AL-REBEH

ABSTRACT

THERMAL GRADIENTS IN CONCRETE BOX GIRDER

AL-REBEH, Salih Khudair
M. Sc. in Civil Engineering
Supervisor: Prof. Dr. Mustafa ÖZAKÇA
November 2014, 121 pages

In this study, a three dimensional thermal analysis using the Finite Element method was carried out to assess the heat conduction in deep concrete box-girder bridges taking into account the prevailing conditions like ambient temperature, solar radiation incident and the velocity of the wind. The temperature distributions and differentials arising from the three dimensional Finite Element model were compared with the site measurements that were available in literature. The current Finite Element analysis has predicted the concrete temperatures effectively with maximum temperature errors ranged from 0.17^{o}C in the North web to 1.71^{o}C in the top flange. The three dimensional Finite Element model was used with meteorological data to carry out numerical measurements of temperature distributions in order to compute thermal gradients in deep concrete box-girders under the summer conditions of Gaziantep, Turkey. The proposed model was then used to study the effect of the cross-section geometry on the temperature distributions and the temperature gradients in deep concrete box girder bridges. The analyzed geometrical parameters are the thickness of the top slab, the thickness of the bottom slab, the width of the cantilever wing and the depth of the box girder. Moreover, some observations related to the vertical and transverse temperature gradients were presented.

Key words: Air temperature, deep box-girder, finite element thermal analysis, solar radiation, temperature gradient

ÖZET

BETONARME KUTU KİRİŞLERDE SICAKLIK DAĞILIMI

AL-REBEH, Salih Khudair
İnşaat Mühendisliği Yüksek lisans
Danışman: Prof. Dr. Mustafa ÖZAKÇA
Kasim 2014, 121 sayfa

Bu çalışmada; ortam sıcaklığı, güneş radyasyonu, rüzgarın hızı ve benzerleri hakim koşulları da dikkate alarak derin betonarme kutu kiriş köprülerde ısı iletimini belirlemek için üç boyutlu sonlu elemanı metotu kullanılarak termal analiz gerçekleştirilmiştir. 3D sonlu elemanlar modelinden elde edilen sıcaklık dağılımları ve farkları literatürdeki mevcut arazi ölçümleri ile karşılaştırılmıştır. Mevcut sonlu elemanlar analizi beton kutu kiriş köprüdeki sıcaklıkları 0.17^{o}C (kuzey webde) ile 1.71^{o}C (üst flanşda) hata aralığında etkili olarak öngördü. Gaziantep ilinde yaz aylarında yapılan meteorolojik ölçümler kullanarak, bu üç boyutlu sonlu elemanlar modeli ile derin betonarme kutu kirişlerde sıcaklık dağılımları hesaplamış ve termal gradyanlar elde edilmiştir. Önerilen üç boyutlu sonlu elemanlar modeli daha sonra, kesit geometrisinin derin betonarme kutu kiriş köprülerde sıcaklık dağılımına ve termal gradyana olan etkisini incelemek için kullanılmıştır. Analiz edilen geometrik parametreler; alt ve üst tablanın kalınlığı, konsol kanat genişliği ve kutu kirişin derinliğidir. Ayrıca, dikey ve yatay sıcaklık değişimleri ile ilgili bazı gözlemler sunulmuştur.

Anahtar Kelimeler: Hava sıcaklığı, derin kutu kirişli, sonlu elemanlar termal analiz, solar radyasyon, sıcaklık gradien.

To My Family, they should receive my greatest appreciation for their enormous love. They always respect what I want to do also give me their full support encouragement over the years.

ACKNOWLEDGEMENTS

First of all, great thanks to Allah his Majesty for enabling me to complete this work.

This thesis is a milestone in my academic career. I have been fortunate learn theories and concepts which would have been impossible if I had not extensively carried out the needed research. I am grateful to a number of people who have guided and supported me throughout the research process and provided assistance for my venture.

I would like to express my respect and regards to my supervisor, Prof. Dr. Mustafa ÖZAKÇA, for guidance, advice, encouragement and suggestions during the preparation of this thesis.

All my words cannot express about my thanks to all my friends, for their interest during this thesis especially for the Ph.D. students Sallal, Farid and Hesham.

Finally, my special thanks are reserved for my wife for her understanding, patience and great help.

TABLE OF CONTENTS

Page

LIST OF FIGURES

Page

LIST OF TABLES

Page

LIST OF SYMBOLS, ABBREVIATIONS AND NOMENCLATURE

C	Specific heat of the material, J/(kg.°C)
Cs	Stefan-Boltzman radiation constant (=5.669×10-4 W/m2•K4)
hc	Convection heat transfer coefficient
hr	Conduction heat transfer coefficient
hd	Depth of cross section
hp	Blacktop thickness (mm)
Is	Total solar radiation incident upon the surface at time t, W/m2
Ib	Direct solar radiation, or beam radiation, on a horizontal surface
Id	Diffused solar radiation on a horizontal surface
Ig	Reflected solar radiation from surrounding objects
k	Thermal conductivity coefficient
kx	Thermal conductivity along x-axis
ky	Thermal conductivity along y-axis
kz	Thermal conductivity along z-axis
n_x, n_y and n_z	Direction cosines
q	Quantity of heat flow
qs	Quantity of heat gain from the sun: solar radiation
qc	Quantity of heat gain/loss due to temperature difference between the air and the boundary surface
qr	Quantity of heat re-radiation from the boundary surface to the surrounding air
Q	Quantity of internal heat

t	Time
T	Surface temperature
Ta	Ambient air temperature
T_{top}	Temperature at the top surface of a concrete cross section
T_{bot}	Temperature at the bottom surface of a concrete cross section
x,y,z	Local axis Cartesian coordinates
α_a	Absorptive coefficient
β	Reflection factor
θ	Inclination angle of surface
αt	Coefficient of thermal expansion
Δ	Change in specified parameter
Ψ	Curvature about specified axis
ϑ	Wind speed
ϵ	Emissivity coefficient
ρ	Density of the material, kgtm3
AASHTO	America Association of State Highway and Transportation Officials
ACI	American concrete institute
ASCE	American Society of Civil Engineers
BS	British standards code
E-W	East-West
FE	Finite Element
FETAB	Finite Element Thermal Analysis of Bridges
LRT	Light Rail Transit
MWNZ	Ministry of Works of New Zealand
NCHRP	National Cooperative Highway Research Program
N-S	North-South
NW	Northwest

OHBDC	Ontario Highway Bridge Design Code
PCI	Precast Concrete Institute
PEI	Prince Edward Island
PTI	Post Tensioning Institute
PWC	Public Works Canada
SE	Southeast
TC	Thermocouple
3D	Three dimensional

CHAPTER 1

INTRODUTION

1.1 General

It is recognized since a long time that bridge structures exposed to climatic conditions show a substantial structural response. The effects of the temperature in bridge structures are affected by each of the daily (short-term) and seasonal (long-term) changes in temperature. Daily and seasonal fluctuations in the average temperature in concrete bridges lead to temperature gradients over the depth of the girder cross-section. If the bridge structure is unrestrained at the supports and subjected to a linear temperature gradient, the girder section undergoes to free longitudinal movement without producing any internal thermal stresses. These effects of daily and seasonal changes in the average temperature have been accommodated by providing expansion joints, sliding or flexible bearings, and flexible substructures. However, if the temperature gradients are nonlinear, an internal thermal stresses will be produced in the cross-section of the structure regardless of whether the structure is restrained at the supports or not.

In this study, the focus will be on the prediction of the temperature distribution in concrete box-girder bridge due to the daily climatic variations, which include solar radiation, surrounding air temperature, and wind speed. The temperature distributions in a bridge have constant temperature changes along its length, while a bridge has an arbitrary temperature distribution over its cross-section.

1.2 Thermal Gradients in Concrete Box-Girder Bridges

Due to changes in the surrounding environment, bridges continuously lose and gain heat. The heat transfer occurs through three principal mechanisms: radiation from the sun, convection of heat between the surface and the ambient air, and re-radiation of the surface to or from the surrounding environment, as shown in Figure1.1.

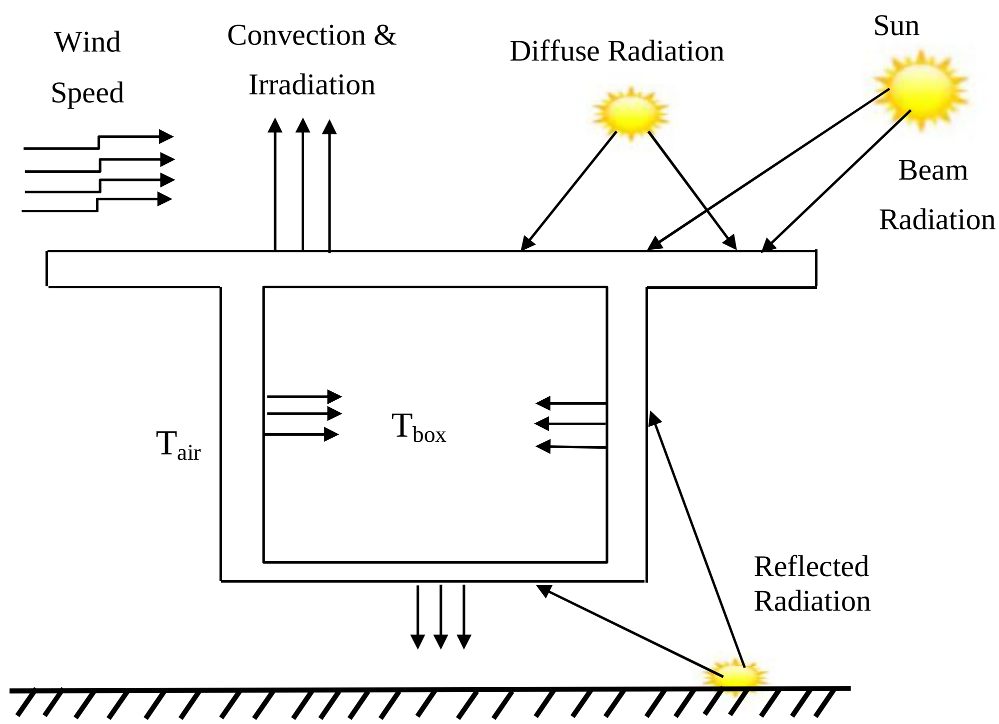

Figure 1.1 The principal mechanism of heat transfer in c box-girder section throughout the summer's days

Changes in the climatic conditions combined with daily thermal cycle cause the thermal gradients in the bridge superstructure. Thermal gradient defined as a temperature distribution over the depth of the girder section relative to the minimal temperature, predicted or measured, which takes as the zero reference point of the thermal gradient.

During the daylight**,** particularly in summer**,** a net rise of heat energy occurs**,** which leads to an increase in temperatures within the structure so that the upper surface becomes hotter than the internal surfaces, because of concrete is relatively weak conductor of heat, the heat flow between the inner concrete layers is very slow. This increase in temperature produces thermal gradients over the bridge girders. These gradients are defined as positive temperature gradients. On the contrary**,** net loss of heat energy that takes place usually along the cooling phase during the hours of the night**,** which leads to a decrease in temperature in the bridge structure and therefore creating negative thermal gradients of temperature with hotter soffit than top.

1.3 Objectives and Scope

In this study, the influences of the daily variation in the ambient air temperature and the change of the intensity of solar radiation on the thermal budget in deep box-girder bridges were studied using a three dimensional (3D) Finite Element (FE) model of an existing bridge. The temperature distributions along and across the slabs and the webs of the girder and the vertical temperature gradients were investigated for the climate of Gaziantep, Turkey. In addition, the proposed model was then used to study the effect of the cross-section geometry on the temperature distributions and the temperature gradients in deep concrete box girder bridges.

This thesis is divided into seven chapters. Current chapter provides evidence of the need to study the effects of heat on concrete bridges. Background and summarizes of previous research, which have been conducted in the field of thermal performance of bridges, are presented in Chapter 2. Chapter 3 presents the principles of heat transfer, which are common in most publications about thermal actions. 3D thermal analysis using the FE method was verified with climate and concrete temperature data from an existing bridge is presented in Chapter 4. In Chapter 5, the proposed FE model was used to evaluate the temperature distribution in deep concrete box-girders using the thermal weather conditions of Gaziantep, Turkey. The weather data including solar radiation, wind speed and air temperature on June 2 were gathered from a special weather station was installed in the campus of Gaziantep University. Geometrical parametric studies, which conducted to evaluate the effects of the certain geometry of cross-section on the temperature distribution and the temperature gradient, are presented in Chapter 6. Finally, the results are summarized in Chapter 7.

CHAPTER 2

LITERATURE REVIEW

2.1 Introduction

As in the case with many topics in the field of engineering, the design of bridges for temperature impacts witnessed several changes. For early design of steel bridges, the effects of temperature were neglected. Bridges are usually simply supported structures, which allows for large movements. Eventually, the longitudinal expansion and contraction can be processed using the average increase and decrease in an expected natural temperature, and then a linear relationship between the temperature variations and the depth of the bridge girder was used.

During the last three decades, there was a growing awareness that the variation of temperatures across the depth of box Girder Bridge is linear. As a result, the continuity of structure lead to self-equilibrating stress (Eigen stresses) through the members of structure and bending stresses that can be very high.

Leonhardt [1, 2] reviewed many bridges damaged by the influence of temperature. Taken in consideration that simple rectangular section with a linear temperature distribution from the upper fiber to the lower fiber, in elastic material, plane sections will remain plane. The deformation that arises from linear and nonlinear temperature distributions is completely different for the linear temperature distribution. The resulting strain in the structure induced by linear temperature distribution is linear, this is consistent with the plane sections will remain plane assumption. Therefore, the self-equilibrating stresses do not develop. However, if the thermal distribution is non-linear, stresses develop as plane sections are imposed to remain plane (see Figure 2.1).

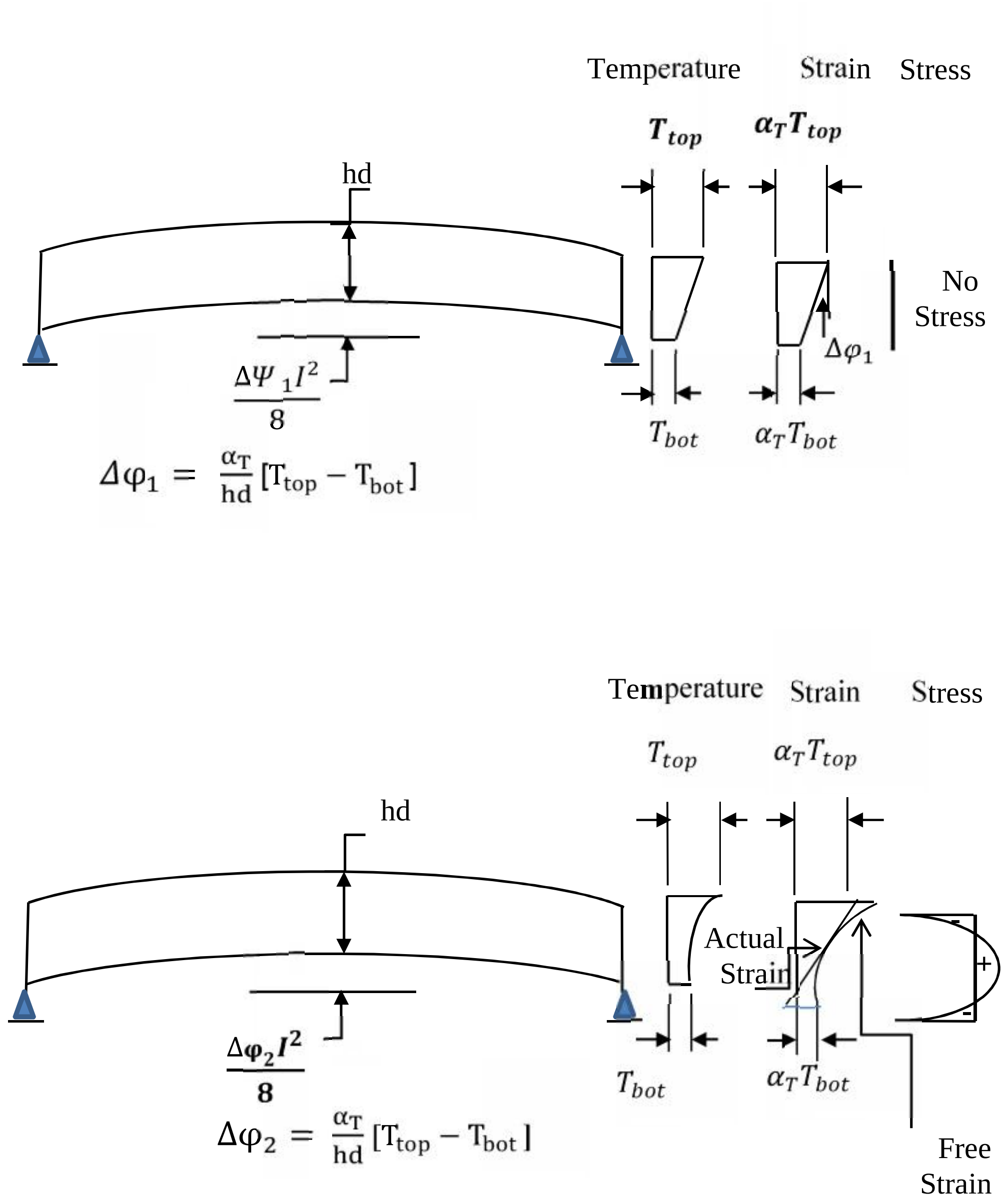

Figure 2.1 Strain and stresses in a simply supported beam resulting from an increase of temperature, which changes linearly and non- linearly over the depth. Ghali et al. [3]

Priestley [4] pointed out that the engineers realized the principles of thermal stresses for a period, even before the Newmarket Viaduct in Auckland in New Zealand that subjected to damage induced by the temperature effect. Since then the researchers in

New Zealand started to investigate the large stresses that can be produced by temperature distributions.

2.2 Temperature Distributions in Bridges

If an accurate thermal distribution is obtained, (i.e. the difference at the temperature within the depth of the cross section of the bridge), a suitable design can be achieved. Priestley [4] noted that the temperature changes in bridges were at specific time thought to be a simple problem. The longitudinal contraction and expansion were taken into account and attention by the use of flexible pavements or sliding bearings. However, after appearing several prestressed concrete box girder bridges in New Zealand began to show notable cracking induced by temperature variations in the 1960's, researchers began to consider this issue closely.

Priestley [5] studied many thermal distributions, these thermal distributions with a constant temperature increase through the slab with no temperature increase in the girders or walls. In addition, thermal gradients with a linear temperature increase only in the deck slab, and then a set of polynomial equations, which represented the thermal changes as a continuous function from the top slab to the bottom slab.

The hypotheses utilized by Priestley in the calculation summarized below

1. A plane section will remain plane that is right for elastic materials. The hypotheses also applied for concrete, under the condition that the shear deformations do not occur.

2. The temperature changes through the depth, but is constant throughout the cross-section in each level. Priestley reported that this hypothesis is only valid for particular conditions, where the bridge is located if the intensity of solar radiation will produce a transverse thermal gradient it should be taken in consideration.

3. The material properties are independent from heat. This hypothesis is efficient for effective temperature ranges (-30°C to 30°C).

4. The principle at of superposition is valid, which applied in many engineering computations in the elastic range.

Figure 2.2 illustrates the design thermal gradient proposed by Priestley [5].

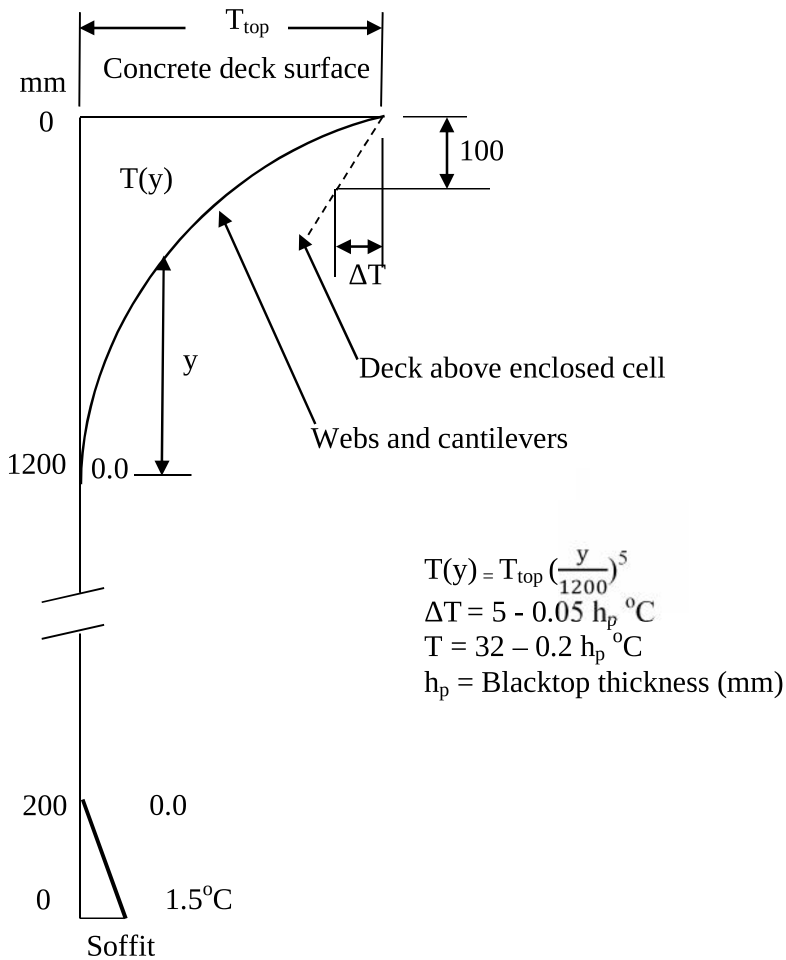

Figure 2.2 Design of thermal gradient proposed by Priestley [5]

Priestley [6] developed an experimental model relied on the Fourier heat transfer equation, and boundary equations, to calculate the thermal response, using this model, he conducted analysis for a group of seven bridge cross sections. As a result, design thermal distribution was obtained.

2.3 Temperature Gradient and Previous Research

There are many investigations conducted to improved analytical method and experimental work. Literature review was widely conducted by Imbeson et al. [7], El-Alam and Massicotte [8] on the impact of temperature on the bridge structure. The following is a brief summary about the previous researches until 2012, which were submitted methods of analysis and parametric studies or carry out comparisons with the measured field data.

Narouka et al. [9] conducted tests on composite steel bridge led to determine a nonlinear temperature distribution across the depth of the cross-section of the bridge. The authors found that the maximum negative gradient was approximately ($9^{o}C$).

Barber [10] proposed a formula that is able to estimate the maximum temperature of bridges pavement. This formula included the air temperature, severity of solar radiation, wind speed, surface temperature and the thermal characteristics of the pavement.

Zuk [11] tried to determine the maximum temperature of the pavement surface of a bridge situated in Virginia City using an adjusted version of Barber formula. The author also proposed an equation to compute the maximum vertical temperature gradient between the top and the bottom surfaces of composite steel bridges in Virginia. Field studies showed good matching between the field measurements and the suggested equation.

Priestley [4] studied the impact of various available proposed temperature gradients and compared the results with available measured data. One of these proposed gradients is the one suggested by Maher [12]. This assumption was depended on various measurements, which obtained from three bridges located in Britain. The author also studied the temperature distribution depended by the Ministry of Works of New Zealand (MWNZ) [13], where the differences in temperature with depth of the top slab are nonlinear distributions (second, fourth, and sixth-degree parabolas). By using this study, Priestley found that the sixth order parabola gives the more accurate thermal gradient compared with available measured data. He also founded that temperature varies along the top 1200 mm to 1500 mm of the bridge. As shown in Figure 2.3.

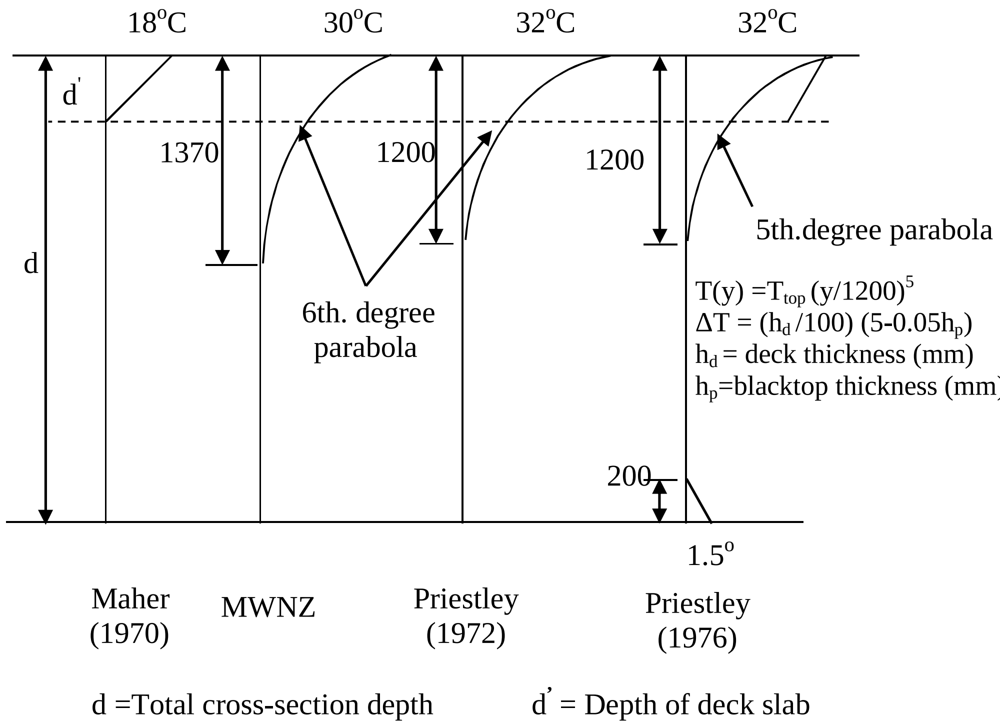

Figure 2.3 Temperature gradients in box girder bridge proposed by Maher [12], MWNZ [13] and Priestley [4, 5].

Emerson [14] studied one-dimensional heat flow through a concrete bridge deck slab using the finite difference method from available data associated with intensity of solar radiation, surrounding air temperature and wind speed .The thermal gradients obtained by this method completely match with a measured prototype thermal gradients.

Lanigan [15] calculated the thermal distribution in the bridge structures by developing a two-dimensional finite element program. He also found that the results taken from the numerical program were matched well with measurements conducted on tests models.

Reynolds and Emanuel [16] study the various parameters, which affect the estimation of temperature gradient between the internal and external surfaces of the bridge. The authors also reported the results of different experimental and analytical studies conducted to investigate the thermal response of bridges.

Radolli and Green [17] calculated the thermal gradients in concrete deck slab bridges and (I) girders using one-dimensional finite difference method. The authors found that the thermal gradient obtained by this method and field measurements were exactly matched. They also suggested simplified and accurate formulas to compute temperature distributions in order to use in the design.

Hunt and Cooke [18] predicted the thermal gradients in bridge surfaces using a semi-analytical method. They proposed that the horizontal thermal distribution could be neglected in this kind of structures. The authors found that comparison between the proposed method and the field measurements carried out by Priestly [4] on pre-stressed concrete box girder bridge was matched well.

Priestley [5] studied the problem of the shape of the temperature gradients and the resulted stresses in the bridge structure. Based on his monitoring and verification in New Zealand, the author suggested a revised temperature distribution to that proposed in 1972. it consisted of three separate parts. In the first part, the author assumed that the temperature differences decreased nonlinearly from a maximum to a minimum through the top surface of the deck slab of the box girder bridge over the depth of 1200 mm, and the nonlinear difference represented by a fifth-order parabola. The second part used only to a top slab, in which temperature differences were assumed to reduce linearly. In the third part, linear differences in temperature were applied at the bottom slab over the depth 200 mm of cross-section of the box girder bridge. As shown in Figure 2.3.

Hambly [19] offered simplified and accurate method for calculating the temperature gradient within cross sections of the concrete box girder bridge, and then the resultant stresses. The author pointed out that the air temperatures inside the air cell of the concrete box girder bridge sections vary between 1 to 2°C. The author pointed that in design, this degree can be assumed fixed. The author also pointed out that the cracking in reinforced concrete sections of bridge, this cracking may not be true or accurate to overlap the thermal stresses with dead and live loads. Each will lead to a various level of cracking. He suggested that the strains induced by each load case be computed first, with the suitable stiffness, then added before calculating the total final stresses.

Emerson [20] presented the results of a study conducted in the British Transport and Road Research Laboratory employing a one-dimensional heat transfer to study the effects of various parameters on the thermal distributions through bridge structures. The author found that the resulting temperature through the bridge structure depended on the emissivity and the absorptivity of the receiving surface for the heat flux, and she found that the wind speed is another significant parameter that can affect the convection mode of heat exchange, high wind speed reduce temperature of the bridge surfaces.

Dilger and Ghali [21] pointed out that many of the bridge designers realized that temperature gradients across concrete bridge sections have a linear distribution, and led to high stresses. However, there is a few directives in design codes on how to accurate compute them. Therefore, the authors proposed a numerical method, employing two-dimensional finite elements with taken in consideration climatic data to calculate the thermal distribution within the bridge cross-section.

Elbadry and Ghali [22, 23] employed the two dimensional finite element method to calculate the temperature distribution through the cross-section of a box girder bridge exposed to climatic conditions including the intensity of solar radiation, average wind speed, surrounding air temperature, and the latitude and longitude of the site. The authors improved a computer program Finite Element Thermal Analysis of Bridges (FETAB), which was first introduced by the authors in 1982. FETAB can represent any model to any cross-section of arbitrary shape or any material. The program simulates the cross section as an assembly of constant heat flow three-dimensions and/or one-dimension quadrilateral heat conduction elements. One-dimensional imaginary linear boundary elements are employed to simulate the climatic boundary conditions. The authors used the program in a parametric study to check the influence of direction of bridge axis, extreme air temperature, average wind speed, cover of surface and depth of the cross-section and shape. They found that the most extreme temperature domain, develops under the conditions of summer season , when the daily rate of surrounding air temperature is high, the daily average of wind speed is the minimum and the deck slab was covered by wearing asphalt surface.

Dilger, et al. [24] studied the thermal influences on a composite box girder bridge utilizing a one-dimensional finite difference method. The authors studied various climatic parameters that affect the thermal distribution, which included the shade length induced by the cantilever top slab and the air inside the air cell of the concrete box girder bridge sections. Furthermore, they found that the extreme thermal gradients exist under conditions of the winter and spring.

Imbsen et al. [7] studied the influence of different thermal distributions on a various set of actual cross-sections of the bridge. Their study included a review of the different available temperature gradients in current bridge design codes, and the authors also recommended four various thermal gradients located in different regions in the United States.

Clark [25] studied the frequency occurrence of temperature distributions in a box girder bridge over the 50 years. He explained that extreme temperature distribution was associated with the maximum and minimum values of the surrounding air temperature.

Hirst and Dilger [26] used a theoretical model to calculate the temperature distribution within the cross section of a bridge. The theoretical method employs program FETAB, which was first introduced by Elbadry [27] at the University of Calgary. The Comparison between the results of the theoretical model and the field data taken from three bridges located in Australia and Canada, and have different cross-sections indicates the validity of the proposed model for a number of bridge kinds and climate systems. They showed that the structural effects for temperatures are outside the scope of their study but the proposed model can be virtually utilized as a first stage in that broader analysis.

Potgieter and Gamble [28] carried out field measurements for the Kishwaukee River Bridge at Rockford, Illinois, and employed analytical model to calculate the temperature gradient in a bridge deck at different times. The authors investigated the implications of nonlinear thermal distributions in box girder bridges induced by the intensity of solar radiation, wind speed and ambient air temperature. Moreover, the authors used weather data from 26 stations scattered throughout the United States to calculate critical temperature distributions in bridges located at those stations. They found that the temperature gradients of up to 32^{o}C, the value included in MWNZ Specifications, were obtained for a bare concrete deck located in the desert in Southwest United States, and found that the coastal areas have moderate climates response. The authors concluded that the temperature gradient is the different between the maximum temperature during the day, which is at the top of the deck slab, and the minimum temperature, at some section below in the cross section but in general not at the bottom. They developed the relationship between curvature- depth and residual stress-depth induced by the nonlinear thermal gradients in bridge structures in order to use in the bridges design at various sites in the United States.

Mirambell and Aguado [29] proposed an analytical model based on two-dimensional finite difference method to calculate temperature gradients and thermal stresses. In addition, the authors compared the results, which obtained from the proposed model with the field results got by other authors, and found good agreement between them. The authors concluded that the unicellular are similar to the multicellular concrete box girder bridges in thermal response, and both cross-section kinds have the same qualitative influence.

Waldron et al. [30] developed the computer program, introduced by Elbadry and Ghali [27], to calculate the environmental parameters obtained from field measur-ement or taken from local weather station to determine the time various boundary conditions. They found that the comparison between the temperature gradient obtained from the program and the experimental data collected for a period of one year for the Cogan Spur Viaduct in South Wales in England were matched well.

Fu, et al. [31] introduced analytical results taken from a parametric study carried out on three kinds of composite bridges exposed to climatic conditions. The authors employed the analytical program ADINA-T in this study, included the influence of convection coefficient, the ratio of the slab-overhanging portion to slab depth, and the diurnal ambient air temperature uncertain in this study. They found that the ratio between the slab overhang to the slab depth is the most effective variable on the thermal distribution through the bridge deck

Branco and Mendes [32] found that the nonlinear temperature gradients that appear in bridges were not easily evaluated, which can be led to structural dilemmas. The authors referred to that a discussion of current design-code provisions presented an approach studies in Southwest Europe. They proposed the evaluation of the temperature gradients considers a numerical tech for finding a solution for the Fourier equation and its related boundary conditions, this technique depended on the finite-element method. Moreover, the authors found that the geometry of the bridge, the thermal properties of concrete and asphalt, the site of the bridge, and the environment conditions should be taken into account. They concluded that for special studies, in which a careful assessment of thermal impacts was important, the numerical technique could also be applied to determine the design values, depended on the geometry and materials of the concrete bridge structure and taken into account the local climate conditions.

Molesini and Massicotte [33] examined the thermal response of the Grand-Mere Bridge situated in Quebec, Canada, which saw sharp deflection combined with centralized cracking. The authors modified the computer program FETAB, [FETAB-2]. The measured minimum and maximum climatic air temperature, wind speed, rate sky opacity, and snow existence for every day of the analysis over a period of three years were considered in the analysis. They found that four various temperature differences can be happened in the cross section of a bridge, two of them lead to thermal stresses that may lead to cracking of concrete and further degradation of the concrete structure. El-Alam and Massicotte [8] used FETAB-2 to study the frequency occurrence of the critical temperature distribution that may be developed during a period of 50 year for the mentioned bridge.

Saetta et al. [34] introduced a numerical procedure depended on the finite element method to carry out thermal analysis of concrete structures. The authors modeled the climatic boundary conditions as an equivalent convective interchange between the surface of the structure and the surrounding environment. They proposed that a suitable imaginary temperature is added to the surrounding air temperature to take into account the influence of heat from the sun. They found that the comparison between temperature distributions taken from the proposed model and field measurement for a box girder bridge were matched well.

Al-Kerwi [35] proposed a temperature gradient model for Iraq weather conditions using a fifth power distribution. She analyzed two continuous precast prestressed concrete bridges based on the proposed model in addition to three models from the literature, based on solar model and climatological data of Baghdad city.

Barr et al. [36] observed temperature variations in precast pre-stressed concrete girders during both fabrication, service period, and evaluated the effects of the temperature variations on stresses, strains, and cambers. They found that curing temperatures reduces the original pre-stressing stress by 3 to 7% and the initial camber by 26 to 40%.

Suzuki, et al. [37] investigated actual bridge temperatures in terms of relationship to the surface freezing process by studying a real bridge in Nagano Prefecture, Japan. The authors showed the impact of wind during the times of the day makes the surface temperature of bridges less than that at the road. Thus, the reason why only bridge surfaces may freeze while roads do not can be explained by the fact that the surface temperatures of bridges are usually lower than those of roads, which can be attributed to their energy budget patterns caused by the wind speed differences between bridges and roads . Moreover, the authors supposed that the wind speed at the bridge is estimated to be stronger than that over flat land or a road. The authors supposed that bridge body temperatures are influenced by the ambient environment. In the winter, the bridge surface was found to be about 2°C lower than the road surface temperature just before sunset.

Wang and Fang [38] carried out field measurement on Pre-stress concrete box girder bridge and conducted a numerical FE simulation using the commercial FE package ANSYS. The author showed that the temperature distributions and its difference in concrete box girder bridges induced by solar radiation, ambient temperature and concrete temperature fields. The author applied the heat fluxes on the surface of concrete box girder, and all the thermal loads as convection loads. The authors compared the results obtained from numerical analysis with the help of the heat transfer theory and FE methods with field measurements, and a good correlation was found. Moreover, they reported that the proposed numerical model can analyses the field of temperature of concrete box girder bridges under solar radiation, with high accuracy.

Larsson [39] carried out field temperature measurements in a concrete slab placed outdoor and conducted a numerical FE simulation using the commercial FE program Bridge/Plus to predict the dynamic thermal conditions in concrete structures. Moreover, he showed that the proposed method is able to describe accurately the different boundary condition such as convection, solar radiation and re-radiation. The author concluded that the model could describe with well accuracy. He presented that the curried out model can describe the impacts of various climatic factors in extreme conditions, with good accuracy, and it is suitable to be used in more studies in other concrete structures with other sets of climatic data.

Wang, et al. [40] carried out field measurement on box girders of continuous rigid frame bridges and conducted a numerical FE simulation using the commercial FE package ANSYS. They found that the simulated temperature field matches the measured observations with high accuracy, moreover they concluded that the temperature analysis of concrete box girder can be perform depending on the trusty climatic data for any area.

Lee and Kalkan [41] carried out experimental and analytical studies over a one year period on prestressd concrete bridge girders to study both the vertical and the lateral temperature gradients with extreme climatic conditions, included the intensity of solar radiation, wind speed and air temperature. The authors found that the comparison between the temperature distributions value taken from the analytical model and the field measurement value showed good agreement. The authors proposed analytical equations that can be used to calculate large vertical and lateral temperature gradients in precast prestressed concrete girders bridges subjected to various thermal environmental loads from daily weather data, and they found that lateral temperature gradients identified to be a second-degree decrease from the maximum surface temperature. Moreover, they estimated the thermal deformations caused by both the vertical and lateral temperature gradients using an analytical method that belong to the one-dimensional heat flow theory.

Larsson and Thelandersson [42] studied the thermal changes in a concrete structure using the FE model. The validation of the model was used with field measurements in a concrete slab along with local thermal data from the Swedish Meteorological and Hydrological Institute. The authors found that thermal gradients resulted from environment variations are one of the main reasons for deformations in concrete structure, which occur along the longitudinal and transverse directions throughout the structure. If these deformations are restrained, stresses will be produced which may lead to notable cracking. The authors also found that The daily changes in the thermal gradient is computed by the FE-model and it is very suitable to be used in estimating critical values for linear thermal gradients based on the recorded data from weather stations. In addition, the authors showed that the critical values of linear thermal gradient were essentially impacted by two different environmental factors. The maximum positive temperature distribution resulted from high intensity of the solar radiation, which took place from April to September. The maximum negative temperature distribution was impacted by the amount of clouds covered.

Lee [43] carried out an experimental and analytical study on a prestressed concrete girder bridge. The analytical model was used to calculate the vertical and transverse thermal gradients in four standards prestressed concrete "I" girder sections at selected cities in United States. In addition, he conducted a numerical finite element simulation using the commercial FE package ABAQUS. The author indicated that the model was used to suggest vertical and transverse thermal gradients to calculate the thermal movement of prestressed concrete girders. He found that the numerical results match with the field measurements, and the numerical model could be used to compute the seasonal thermal gradient in standard prestress concrete bridge graders at respective area in the United States. The author reported that both the vertical and the lateral thermal gradients were evolved to assist engineers in estimating the thermal behavior of pre-stressed concrete bridge girders during the construction process.

Zhang et al. [44] used the ANSYS APDL parametric design language to develop a secondary visual module for the analysis of temperature field in pre-stress concrete box girders. Comparative study with field measurements of a variable section pre-stress concrete box girder bridge showed that the used FE simulation can objectively reflect the actual boundary conditions with high accuracy and can meet the requirements of practical design and analysis in engineering.

Carboni and Lacarbonara [45] used the finite element multi-physics package COMSOL to evaluate the thermo-elasto-dynamic behavior of concrete box grader bridge. A 3D model was simulated to evaluate the temperature field due to solar and environmental exposure and its effects on the natural frequency of the bridge. They observed negative variations of the natural frequencies in summer due to the heating of the structure, which reach a maximum around 3:00 pm., while, in winter, positive variations were observed due to the cooling of the structure during the early hours of the morning until 9:00 am, beyond which the variation start to decrease up to about 3:00 pm.

2.4 Proposed and Design Temperature Distributions

Maher [12] suggested a first-degree distribution of temperature through the top slab of the concrete box-girder bridge, which relied on the experimental studies in Australia and United Kingdom. He proposed the changes only across the flange section, because he thought that this part is very important. Figure 2.4 illustrates the linear thermal distributions in the top flange of the box girder bridge.

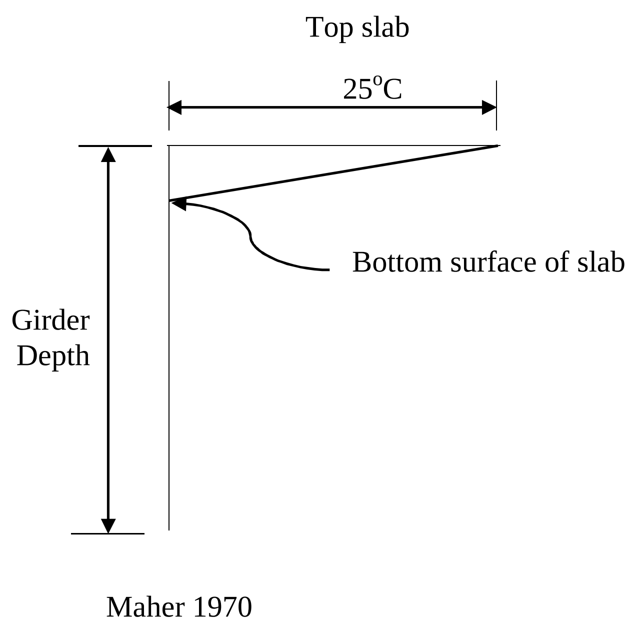

Figure 2.4 Temperature distribution proposed by Maher [12]

Before 1973, concrete bridges in the United Kingdom were designed for an extreme thermal difference of 8.3^{o}C, which varies linearly throughout the section. Emerson [28] pointed that this was not enough and hence a non-linear thermal differences based on twelve years of field studies in seven bridges with different depths located in England and Wales. The effects of the depth of surfacing layer included using the adjustment in the computations. In 1978, a multiple straight line was suggested in another study by Emerson [47], which was depended by the design-loading document BS5400. These thermal distributions were based on the extreme climate conditions over a period of twelve year and can be extended in the future. Figure 2.5 illustrates the different thermal distributions in the British Code.

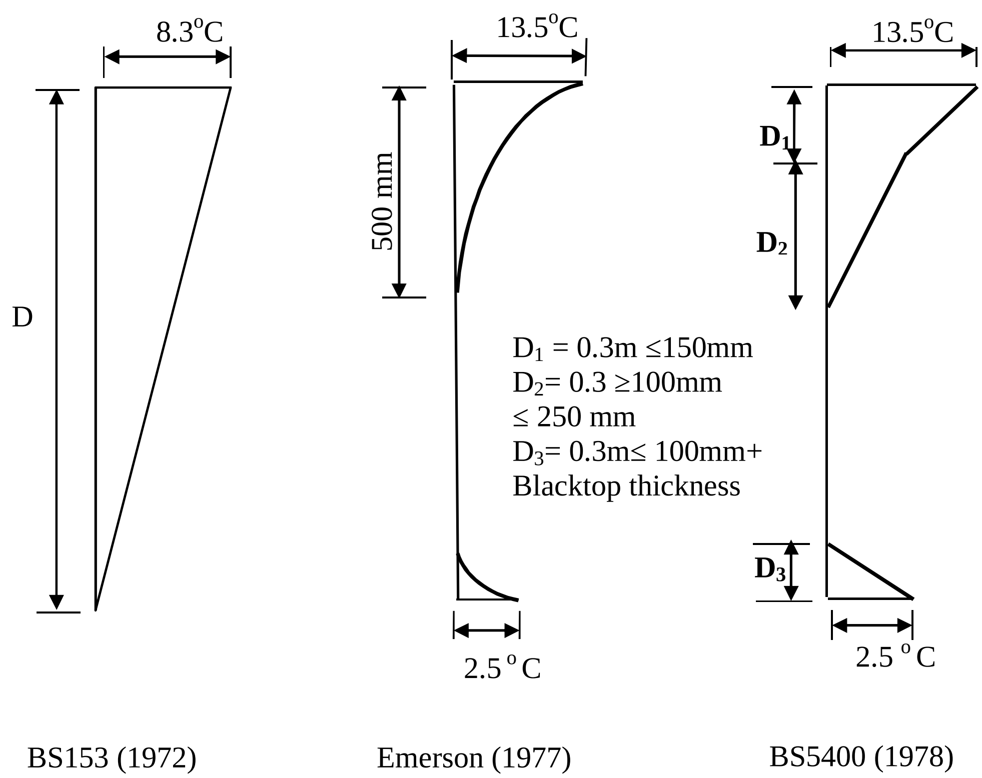

Figure 2.5 Thermal gradients suggested by the British Standards Code and Emerson [46].

The America Association of State Highway and Transportation Officials (AASHTO) bridge specifications reviewed relevant guidelines to the thermal response of bridge structures resulting from ambient climatic conditions. Before 1989, AASHTO presented only uniform temperature variation and did not mention temperature gradients for the design of bridges. Roberts-Wollman et al. [48] noted that the bridge designers, who felt concerned about the influences of temperature gradients in concrete bridges, usually used Priestley model (Priestley, 1976), As shown in Figure 2.2, or used the values of the vertical and transverse temperature distributions are 10°C and 15°C, respectively. These values reported by the Post Tensioning Institute (PTI, 1977), While the temperatures contained in the PTI manual are not suitable for identifying appropriate temperature differences in bridge structures. Figure 2.6 shows thermal gradients suggested by the National Cooperative Highway Research Program (NCHRP).

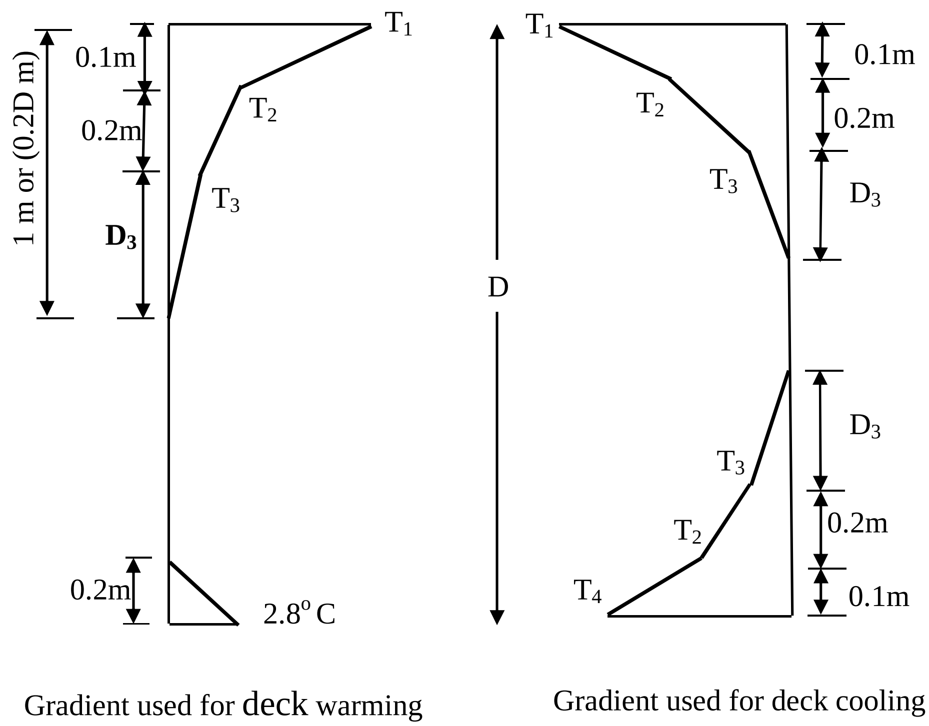

Figure 2.6 Thermal gradients suggested by the NCHRP

In 1989, the AASHTO [49], according to the (NCHRP) Report 276, presented uniform bridge temperatures and thermal distributions and issued the AASHTO Guide Specifications, the effects of temperature in concrete bridge cross sections (1989) for the design of reinforced and pre-stressed concrete bridge superstructures. The AASHTO specifications (1989) Presented the peaks of effective values for bridge temperatures based on the peaks of natural air temperatures at the site of bridge, and the maximum temperature variations were identified in four zones according to solar radiation for the United States. Figure 2.7 shows the vertical temperature of the concrete cross sections, which proposed by AASHTO [49].

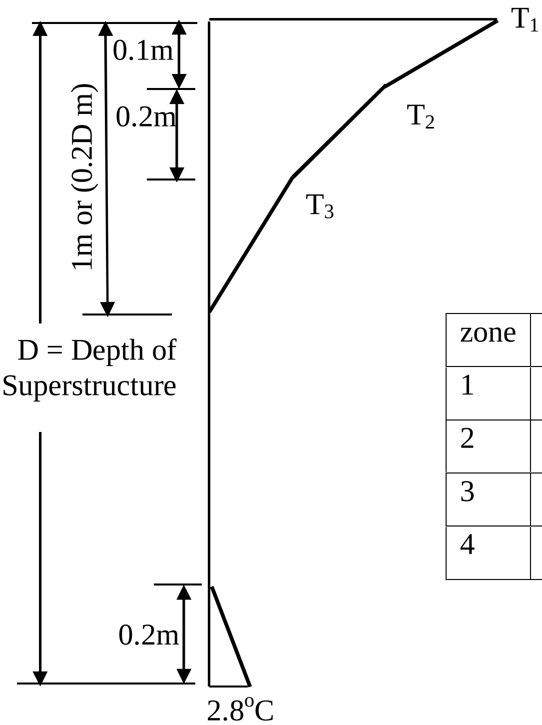

zone	T1 (°C)	T2 (°C)	T3 (°C)
1	30	7.7	2.8
2	25.5	6.6	2.2
3	22.7	6.1	2.2
4	21.1	5	1.6

Figure 2.7 Vertical thermal gradients for concrete cross sections AASHTO [49]

In 2007, the AASHTO [50], in accordance with the AASHTO [49], presented in more simplified way the uniform bridge temperatures and vertical thermal gradients. AASHTO [50] determines peak temperatures related with uniform temperature movements. For concrete decks with concrete girders, the peak values of temperatures are identified as 44.5°C and 5.5°C in a moderate weather and 0.0°C and 44.5°C in a cold weather. according to the AASHTO [50], the climatic conditions is specified during a year by the number of freezing days, which is defined as the daily rate for temperature is less than 18°C, if the total number of freezing days during the year less than 14 days, the climatic conditions is considered a moderate. In addition, AASHTO [50] presents the vertical thermal gradient.

Figure 2.8 illustrates the vertical thermal gradients in concrete girder with concrete slabs. The values of the temperature gradient, T1 and T2, are identified according to the solar radiation zones in the United States

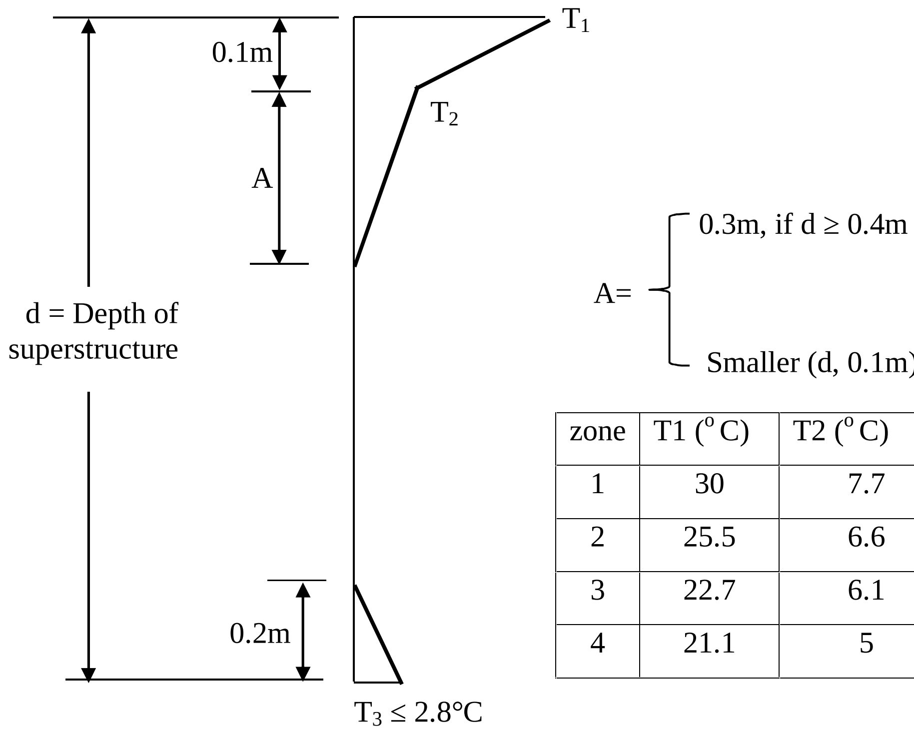

zone	T1 (^{o}C)	T2 (^{o}C)
1	30	7.7
2	25.5	6.6
3	22.7	6.1
4	21.1	5

Figure 2.8 Vertical thermal gradients for concrete superstructures, AASHTO [50]

Dimension A in Figure 2.8 is 0.3 meter for concrete girder, which are 0.4 meter, or more in depth. For concrete shallow sections with girder depth is less than 0.4 meter, dimension A is the smaller 0.1 meter or the depth of concrete girder. The value of T3 in Figure 2.9 can be taken as 0.0^{o}C, unless an experimental study in the specific location may be conducted to determine a suitable value.

CHAPTER 3

MECHANISM OF HEAT TRANSFER IN BRIDGES

3.1 General

Exposed concrete bridge structures continuously gain and lose heat energy through three principal mechanisms of heat transfer: radiation from the sun, convection of heat between the external surfaces of the bridge and the ambient air, and re-radiation from the surfaces to the surrounding environment. The solar radiation reaches the surfaces of the bridge, mainly through direct beam radiation, diffuse radiation from the sky, and reflected radiation from the ground and other surrounding objects. The incoming radiation reaching the exposed surfaces may be reflected back or may penetrate the surface, absorbed and converted to heat. The quantity of absorbed energy depends on the nature and color of the receiving surface, where the dark rough surfaces have higher absorbance from the light and smooth surfaces.

3.2 Basic Equations of Heat Transfer

The temperature field within a bridge is governed by Fourier heat conduction differential equation. For a bridge with internal heat source, the heat conduction equation can be expressed as follows, Ghali et al. [25].

$$\frac{\partial}{\partial x}\left(K_x \frac{\partial T}{\partial x}\right) + \frac{\partial}{\partial y}\left(K_y \frac{\partial T}{\partial y}\right) + \frac{\partial}{\partial z}\left(K_z \frac{\partial T}{\partial z}\right) + Q = \rho C \frac{\partial T}{\partial t} \quad (3.1)$$

Where: T is the temperature of a body at any point (x, y, and z) at any instant (t). K_x, K_y and K_z are the thermal conductivities of concrete in the x, y and z direction, which is the rate of heat flow by conduction per unit area per unit temperature gradient. The units of K are *W/ m ^oC*. Q is the amount of heat generated within the body (e.g. by hydration of cement) per unit volume, *W/m^3*. ρ is the density of concrete, *kg /m^3*. C is the specific heat of concrete, that is, the quantity of heat required to increase the temperature of the unit mass of the material by one degree. The unit of C is *J/ kg ^oC.*

The thermal boundary conditions associated with the well-known Fourier's equation (3.1), can be expressed in the following form:

$$K_x \frac{\partial T}{\partial x} n_x + K_y \frac{\partial T}{\partial y} n_y + K_z \frac{\partial T}{\partial z} n_z + q = 0 \qquad (3.2)$$

Where: n_x , n_y, n_z are direction cosines of the unit outwards vectors normal to the boundary surfaces. q is the rate of heat transfer between the surrounding environment and the exposed concrete surfaces per unit area, in *W/ m*^{2}.

For the special case of isotropic, homogeneous, and temperature independent materials $K_x = K_y = K_z$ = constant, then Eq. (3.1) can be written as:

$$K\left(\frac{\partial^2 T}{\partial x^2} + \frac{\partial^2 T}{\partial y^2} + \frac{\partial^2 T}{\partial z^2}\right) + Q = \rho C \frac{\partial T}{\partial t} \qquad (3.3)$$

In addition, Eq. (3.2) can be reduced as:

$$K\left(\frac{\partial T}{\partial x} n_x + \frac{\partial T}{\partial y} n_y + \frac{\partial T}{\partial z} n_z\right) + q = 0 \qquad (3.4)$$

3.2.1 Boundary conditions

The heat energy transferred between the exposed surface elements and the surrounding environment is made up from three components of the principle mechanism of heat transfer. The sum of these components differs with time and the position of the point on the boundary surfaces and is given as:

$$q = q_c + q_r - q_s \qquad (3.5)$$

3.2.1.1 Convection

h_c is the heat lost to, or gained from, the ambient air by convection because of the difference between bridge surface temperature and the ambient air temperature, it can be calculated using Newton’s law of cooling as:

$$q_c = h_c(T - T_a) \qquad (3.6)$$

Where h_c is the convection heat transfer coefficient with dimension $W/m^2 K$. The surface coefficient of convective heat transfer relies mainly on wind speed and to a less degree on many variables such as surface roughness and geometric configuration of the exposed structure [51]. Field study and experimental formulas are commonly used to identify its value. Ibrahim [52] used the following experimental formula originally recommended by Kehlbeck [53] to identify the convection coefficient values for bridge structures.

$$h_c = \begin{cases} 3.83\vartheta + 4.67 & \text{(Top surface of bridge deck)} \\ 3.83\vartheta + 2.17 & \text{(Bottom slap)} \\ 3.83\vartheta + 3.67 & \text{(Outer walls)} \\ 3.5 & \text{(inside surface of the box)} \end{cases} \tag{3.7}$$

where: ϑ is wind speed in m/s.

3.2.1.2 Solar radiation:

q_s is the heat gain due to solar radiation received by the exposed surfaces, which can be expressed in the following form:

$$q_s = \alpha_a \ I_s \tag{3.8}$$

where: α_a is a dimensionless solar radiation absorptivity coefficient of the surface material, which relies on the nature of the surface. The value of α_a is less than 1.0. I_s is the total (or global) solar radiation (direct and indirect) striking the earth's surface at time t. It consists mainly of three components: the beam (direct) radiation I_b (W/ m^2), the sky diffuse radiation I (W/ m^2) and reflected radiation (ground radiation) I_r (W/ m^2). Its value can be taken from climatological data, obtained from tables published, or computed from mathematical equations.

$$I_s = I_b + I + I_g \tag{3.9}$$

I_g is the contribution from surrounding reflected radiation (ground reflected radiation). The reflected radiation relies on the ground cover. The proportion of total radiation, which is reflected by the ground, is a function of the properties of the adjacent elements such as the type of vegetation or the existence of water. These properties are expressed by the reflection factor. The ground radiation on a tilted surface can be given by the following expression.

$$I_g = \beta I_s \left(\frac{1 - \cos\theta}{2}\right) \quad (3.10)$$

where: β is the reflection factor of the surrounding surfaces I_s is the total heat flux on the horizontal surfaces surrounding and θ is the inclination angle of surface.

Table 3.1 Values of reflection factor (β) for different surrounding surface

Surrounding Surface	Reflection factor (β)
Fresh snow	0.8 -0.9
Old snow	0.6-0.7
Calm water surface	0.05 - 0.18
Concrete	0.17 - 0.27
Sand	0.15 - 0.45
Sea and Ocean	0.05 - 0.12

3.2.1.3 Thermal irradiation:

q_r is the amount of radiation exchanged between bridge surfaces and the ambient air, which is given by Stefan-Boltzmann's law as:

$$q_r = C_s \epsilon (T^4 - T_a^4) \quad (3.10)$$

It is possible to modify equation (3.8) and to make it linear equation according to Newton's law of convection as follows:

$$q_r = h_r (T - T_a) \quad (3.11)$$

where: h_r is the conduction heat transfer coefficient given by:

$$h_r = C_s \epsilon [(T + T^*)^2 + (T_a + T^*)^2](T + T_a + 2T^*) \quad (3.12)$$

Where: T and T_a are the absolute temperatures of the surface and of the ambient air, respectively, T^* is the constant which is equal to 273 used to convert temperature from degree Celsius (°C) to degree Kelvin (K). C_s Symbolize to the Stefan-boltzman constant, which equals to 5.67 x 10^{-8} ($W/m^2 . k^4$), ϵ is a dimensionless coefficient of emissivity of the surface, and its value is between 0.0 and 1.0, the latter value is for an ideal radiator, the blackbody (W/m^2).

There are many laws that can be described the convection coefficient (Table 3.2) and all of those laws are relied on the same principle about the convection coefficient, which can be divided in two parts:

The first part that is associated to natural convection and the second part relying on the velocity of the wind (v), which is related to forced convection.

Table 3.2 Various methods to compute the heat transfer coefficient of radiation according to some leading researchers

Authors	**Expressions**	**Unities**
Branco et al. [32]	$h_r = \varepsilon[4.8+0.075(T_a-5)]$ if $T_a > 5°C$ $h_r = 4.8\varepsilon$ if $T_a < 5°C$	Celsius (°C)
Elbadry& Ghali [22]	$h_r = C_s\, \alpha e[(T+T^*)^2 + (T_a + T^*)^2] (T + T_a + 2T^*)$	Celsius (°C)
Mendes [54]	$h_r = 4\varepsilon\sigma T_m^3$ $T_m = (T + T_a)/2$	Kelvin (K)
Silveira [55]	$h_r = 4\varepsilon\sigma T_a^3$	Kelvin (K)

The final expression of the heat exchange can be written as:

$$q = h_c(T - T_a) + \alpha_a I_s + \alpha_a \beta I_s \left(\frac{1 - \cos\theta}{2}\right) + C_s \epsilon (T^4 - T_a^4) \quad (3.13)$$

Finally, the FE package COMSOL Multiphysics [56] used to solve the heat flow equation (3.1) after applying the thermal boundary conditions expressed by equation (3.2).

CHAPTER 4

FINITE ELEMENT MODEL AND COMPARATIVE STUDY

4.1 General

This research proposed FE model for the temperature prediction of box girder bridges exposed to climatic conditions based on the heat transfer assumptions (the temperature distribution along the longitudinal axis of the bridge is assumed to be constant) and FE method. The temperature results derived from the present method are compared with the experimental results presented by Sveinson [57]. The comparison between analytical results and experimental results has been carried out for the deepest cross-section. To verify the ability of the proposed model to predict the temperature distribution and temperature gradient in a bridge girder at different time given the transient weather conditions, field measurements including thermocouple readings for temperature, were collected over an eighteen months, which began in January 1998 for a concrete box girder bridge located in the New Brunswick, Canada.

4.2 Problem Definition

Due to the availability of almost all of the required input data, an experimental and numerical study conducted on Confederation Bridge, which is located in the New Brunswick, Canada by Sveinson [57] and that was chosen for comparison purposes in present study. In this study, [57] was used two cross-sections of the box-girder in the experimental part because the recorded data was available for two cross sections of the main girder during an eighteen months period of the beginning 1998 to mid-1999, the deepest cross section which is adjacent to a pier and the shallow cross section at mid span between piers, while in the presenting of the numerical study, only the deep cross section S1 was chosen as shown in Figure 4.1.

The main part of the Confederation Bridge consisted of 46 successive spans with total length of 12900 m. The central span is 250 m long and has a depth varying from

4.5 m at mid-span to 14 m at the pier, with a simply supported ends and drop-in precast section each second span. Field measurements of changes in temperatures were available for the deepest cross-sections located at the pier, which were gathered during an eighteen months period since the beginning of 1998 to the middle of 1999.

On the other hand, the author was used the computer program FETAB to simulate the problem and carried out further structural analysis and parametric studies. As shown in Figure 4.1, fourteen sets of thermocouples were installed across the top and bottom slab and the two webs, five sets have five thermocouples each, while nine sets have three thermocouples each.

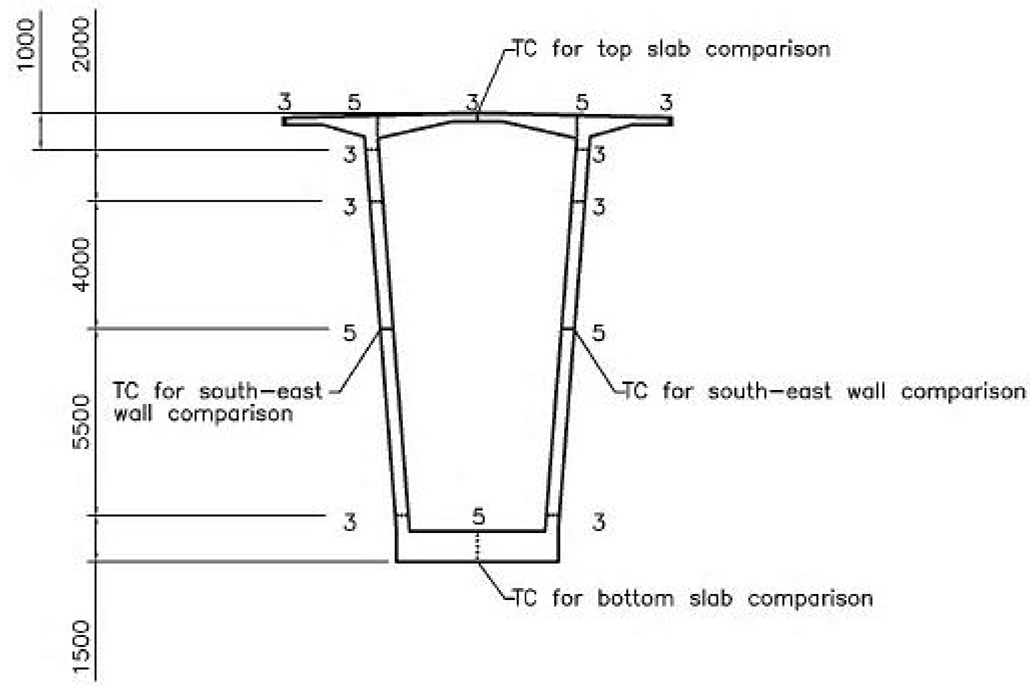

Figure 4.1 Distribution of the thermocouples locations for the cross-section S1 of the main girder of the confederation bridge carried out by Sveinson [57].

The latitude of the test location is 46^{o} 12' 55" and longitude is 63^{o} 44' 45". The longitudinal axis of the girder lies on the southwest-northeast direction. Therefore, the vertical surfaces of the girder webs are facing the northwest and southeast direction.

Because of the difficulty of measuring thermal properties of concrete, the author used some recommended values from the literature and utilized it in the FE model. The used thermal conductivity, specific heat, and concrete density were 1.7 *W/m.K*, 1000 *J/kg.K* and 2400 kg/m^3 respectively. The emissivity and absorptivity coefficients were assumed 0.9 and 0.5 respectively.

The used compressive strength, the coefficient of thermal expansion and the modulus of elasticity for the concrete bridge were 55 MPa in 28 day, 8.3×10^{-6} /°C and 38.7 GPa, respectively. The author was chosen three days to present his experimental results these are June 10, 1998, August 9, 1998 and February 4, 1999, while in the presenting of the numerical study, the obtained results on only the August 9 was chosen.

For the existing data on August 9, 1998, which fall on day 221, the maximum and the minimum values of daily air temperatures that happened on this day were 26.8°C and 21.6°C, respectively, and the average wind speed for this day was 29.5 m/s.

Figure 4.2 display the predicted and recorded temperatures at the thermocouple locations for the deep section S1, on August 9, 1998 at 15:00. After the deep cross section modeled, comparison conducted between the computer results from FETAB and available recorded temperature data to evaluate the accuracy of the computer model for the same thermocouple locations, where thermocouples were installed in the selected cross sections of the Confederation Bridge during the construction period.

As shown in Figure 4.2 that the predicted and recorded temperatures were usually within a degree of each other. This can be justified by the fact that the coefficient of convection used in this investigation depended on the actual recorded wind speed so that the impacts resulting from the wind speed during and after construction phase have been observed.

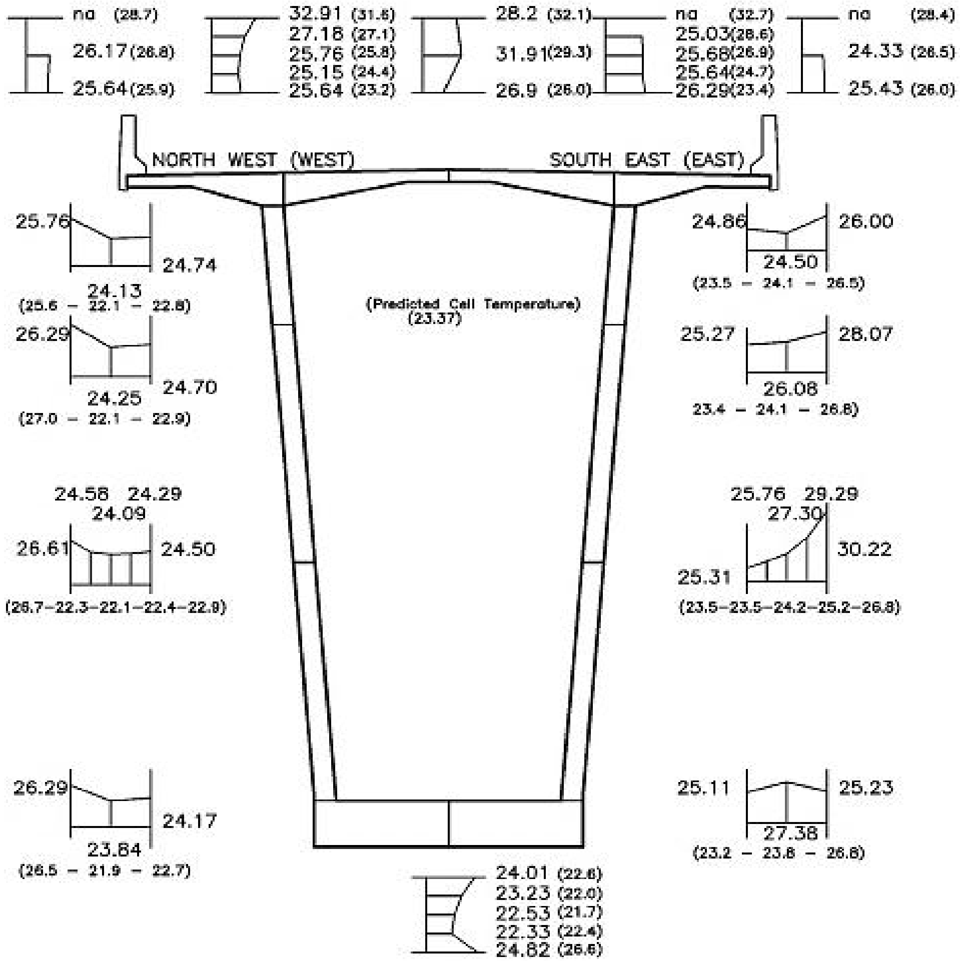

Figure 4.2 Recorded and predicted temperature for cross-section S1, August 9, 1998 at 15:00 hours. Sveinson [57]

4.3 Finite Element Modeling

In order to account the variations in temperature in concrete structures with large sets of data, a 3D FE model was developed. The model was used with meteorological data to carry out numerical measurements of temperature distributions in order to compute thermal gradients in deep concrete box girder bridge under the summer conditions of Gaziantep city. The main problem when predicting temperature distributions in concrete bridge structure is description the boundary conditions and the environmental exposure. The FE analysis package, COMSOL Multiphysics [56], was used in this study. In COMSOL choosing element type is only required to define the type of the shape function whether Lagrange element or Hermitian element. In addition, the order of the shape function should be defined whether linear, quadratic, cubic, quartic or quantic. Since radiation is a nonlinear problem, then nonlinear element should be used. For heat transfer with radiation, the default element order is quadratic. The temperature distributions of the structure were simulated with the heat transfer module of COMSOL. The convection heat transfer between the boundary surfaces of the bridge and the ambient air was simulated using the convection boundary load in the heat transfer module of COMSOL. The radiation heat exchange between the exterior surfaces of structure and the ambient air was simulated using the surface-to-ambient radiation node in the heat transfer module. Solar radiation was molded using the source node by defining the location, the time data and the maximum solar incidence. The wind speed, the maximum and the minimum air temperature and the intensity of solar radiation were obtained from a local meteorological station (installed in the campus of Gaziantep university), which was installed to collect the meteorological data such as ambient air temperature, wind speed, and solar radiation.

The temperature variation across the bridge boundaries is governed by Fourier heat conduction differential equation. On the other hand, the heat conduction differential equation is time-dependent. Thus, it is essential to define an initial condition, which is represented the variation in temperature across the bridge boundaries at the initial time. In the current research, the initial temperature was considered uniform and equal to the surrounding air temperature at the initial time.

The material thermal properties and thermal loads were assumed equal to those considered by Sveinson [57], which are shown in the Table below:

Table 4.1 Thermal material properties and thermal loads values

K (w/m K)	C (J/kg K)	ϵ	α_a
1.7	1000	0.9	0.5
Maximum T_a (^oC)	Minimum T_a (^oC)	Wind speed (m/s)	(β)
28.6	21.6	29.5	0.1

The values of the heat transfer coefficient of convection, h_c, for the various surfaces of the box section are calculated using Equation (3.7). The other information that is necessary in the analysis is day of the year = 221, latitude = 46° 12' 55" N, longitude = 63^o 44' 45" W, altitude = 40.8 m. The orientation of the longitudinal axis of the bridge with respect to the north = 45°.

Figure 4.3 shows the dimensions of the deep section of the box-girder and the locations of thermocouples. The concrete temperatures were measured by eight groups of thermocouples along the depth of the girder and across the top and bottom flange (A, B, C, D, E, F, G and H), as shown in Figure 4.3. Groups (D, E and F) were installed across the top flange, group (A) was installed across the bottom flange and the remaining four groups were installed across the two walls (the northwest and southeast wall). Groups (A, D and F) have five thermocouples each, while the remaining groups have three thermocouples each.

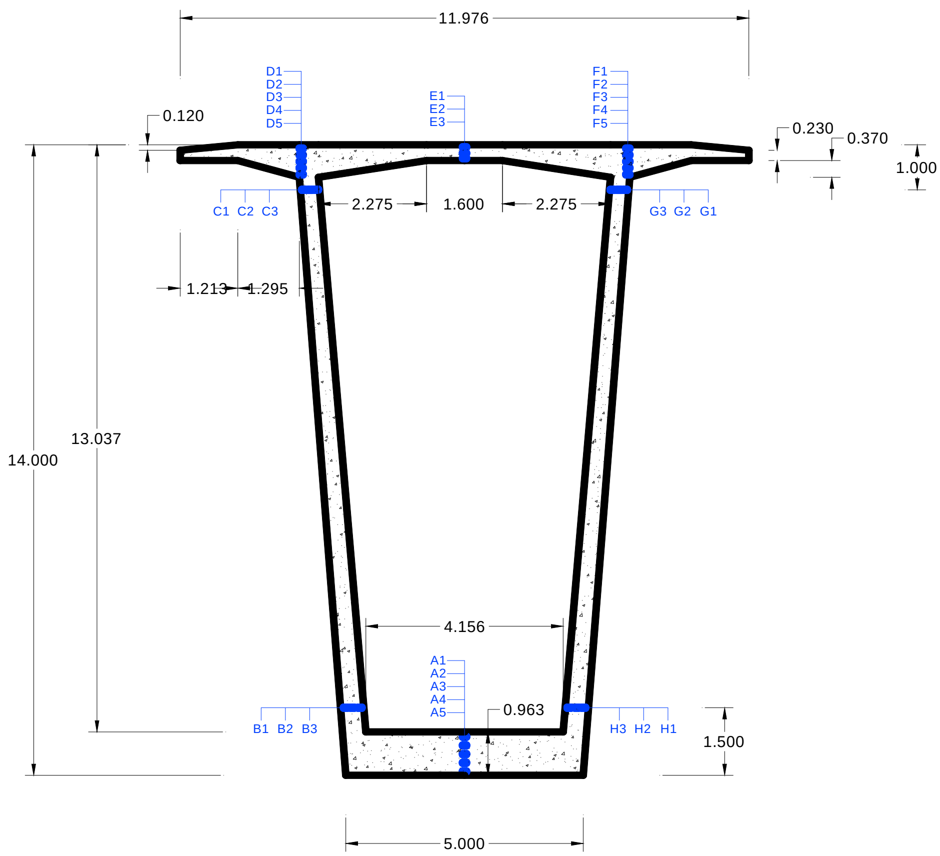

Figure 4.3 Dimensions of the deep section of the box- girder and the locations of thermocouples.

4.4 Verification of the Finite Element Model

To verify the ability of the FE analysis conducted in this study in order to predict the temperature distributions and the temperature gradients in the cross-section of box-girder bridges, the comparison was conducted between the temperature values obtained from the thermal analysis of the current study and those gathered from site measurements.

In this study, the temperature distributions arising from the FE model were compared with the site measurements that were presented by Sveinson [57] on the Confederation box girder bridge located in the New Brunswick, Canada, on 9 August at 15:00.

The Average Absolute Errors (AAE) and the Maximum Absolute Error (MAE) are the statistical measurements that were used in this study to validate the accuracy of the current FE thermal analysis that can be computed by the following expression.

$$\mathrm{AAE} = \frac{\sum \mathrm{T_p} - \mathrm{T_m}}{\mathrm{n}} \tag{4.1}$$

Where:

T_P is the value of predicted temperature, which obtained from FE model.
T_m is the value of measured temperature, which taken from field data.
n is the total number of the predicted and measured temperature values.

Table 4.2 shows the computed AAE values for the eight groups of thermocouples, which ranged from 0.129^{o}C (thermocouples Group G in the northwest wall) to 1.11^{o}C (thermocouples Group F in the top flange) of the study model. The MAE for all thermocouple groups are shown in Table 4.2, which also ranged from 0.171^{o}C in the northwest wall (thermocouples Group G) to 1.711^{o}C in the top flange (thermocouples group D). The values of AAE and MAE indicate that the predicted temperatures in this study are very close to the actual measured temperatures at the same locations.

Table 4.2 AAE and MAE between the predicted temperatures values and the measured temperatures values at all thermocouples groups

Location	Set of sensor	Predicted temperature	Experimental temperature	Absolute Error	AAE	MAE
Top slab	E	27.150	28.2	1.05	0.830	1.049
		31.282	31.91	0.63		
		26.084	26.9	0.82		
	D	31.198	32.91	1.711	0.908	1.711
		26.519	27.18	0.660		
		25.046	25.76	0.713		
		24.766	25.15	0.383		
		24.568	25.64	1.071		
	F	31.213	Na	-	1.110	1.574
		26.559	25.03	1.529		
		25.111	25.68	0.568		
		24.869	25.64	0.770		
		24.715	26.29	1.574		
Bottom slab	A	26.071	24.82	1.251	0.925	1.251
		23.489	22.33	1.159		
		23.123	22.53	0.593		
		22.906	23.33	0.423		
		22.813	24.01	1.196		
NW web	G	24.715	24.86	0.144	0.129	0.171
		24.671	24.5	0.171		
		26.074	26	0.074		
	H	24.096	25.11	1.013	0.813	1.013
		24.374	25.23	0.855		
		26.807	27.38	0.572		
SE web	B	24.494	24.17	0.324	0.827	1.678
		25.518	23.84	1.678		
		26.769	26.29	0.479		
	C	24.568	24.74	0.171	0.294	0.462
		24.592	24.13	0.462		
		26.008	25.76	0.2485		

Table 4.3 shows the computed AAE and MAE values across the top flange, the webs, and the bottom flange of the study model. The largest MAE is 1.71°C in the top flange (groups D, E and F) and the smallest MAE 1.03°C in the northwest wall (groups G and H). Therefore, the magnitudes and the variations of the predicted results match well with the experimental results.

Table 4.3 AAE and MAE between the values of the predicted and measured temperatures along all thermocouples sections

Section	AAE	MAE
TOP Flange	0.948	1.711
Bottom Flange	0.925	1.251
northwest web	0.471	1.013
southeast-East web	0.560	1.678

Figure 4.4 shows the predicted and measured vertical temperature distributions across the bottom flange on August 9 at 13:00. The maximum difference of 1.25°C occurred at the bottom surface of the bottom slab (thermocouple A5), while the minimum difference of 0.423°C occurred at the internal surface (thermocouple A2). Therefore, the shape of the predicted temperatures in the bottom slab was in very good agreement with those of the measurement.

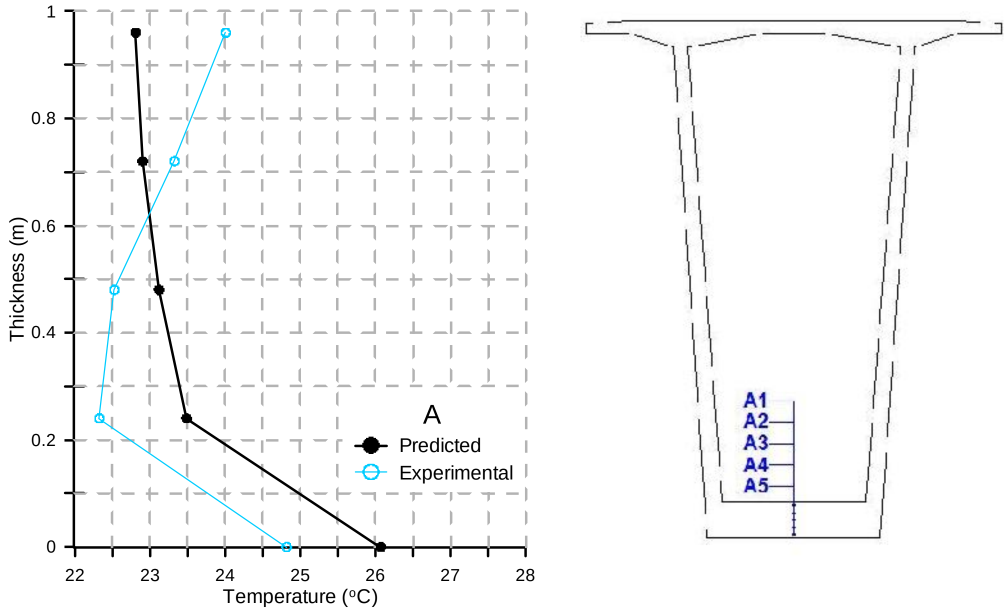

Figure 4.4 Comparison between the FE temperatures and the field temperatures, set (A)

Figure 4.5 depicts the comparison between the measured and predicted vertical temperatures along the depth of the south side of the top flange of the study model The maximum difference of 1.71°C occurred at the top surface of the top slab (thermocouple D1), while the minimum difference of 0.383°C in the internal surface (thermocouple D4). Therefore, the predicted temperatures in this model are very close to the actual measured temperatures at the south side of the top slab.

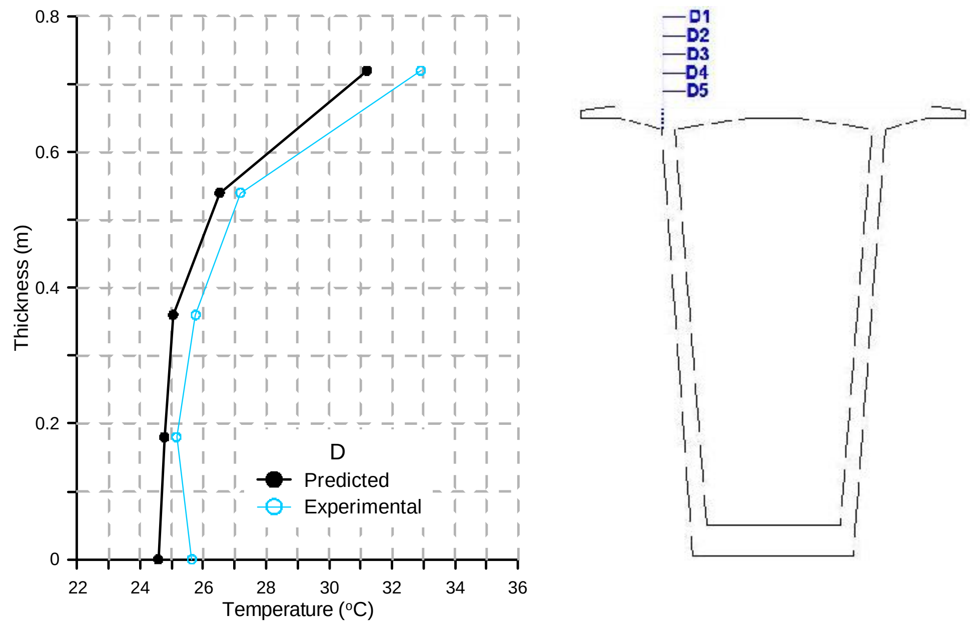

Figure 4.5 Comparison between the FE temperatures and the field temperatures set (D)

Figure 4.6 depicts the comparison between the measured and predicted vertical temperatures along the depth of the north side of the top flange of the study cross section. The largest difference of 1.57°C occurred at the bottom surface of the top flange (thermocouple F5), while the smallest difference of 0.52°C occurred at the internal surface (thermocouple F3). As a result, the shape of the predicted vertical temperatures on the north side of the top flange was in very good agreement with the experimental results.

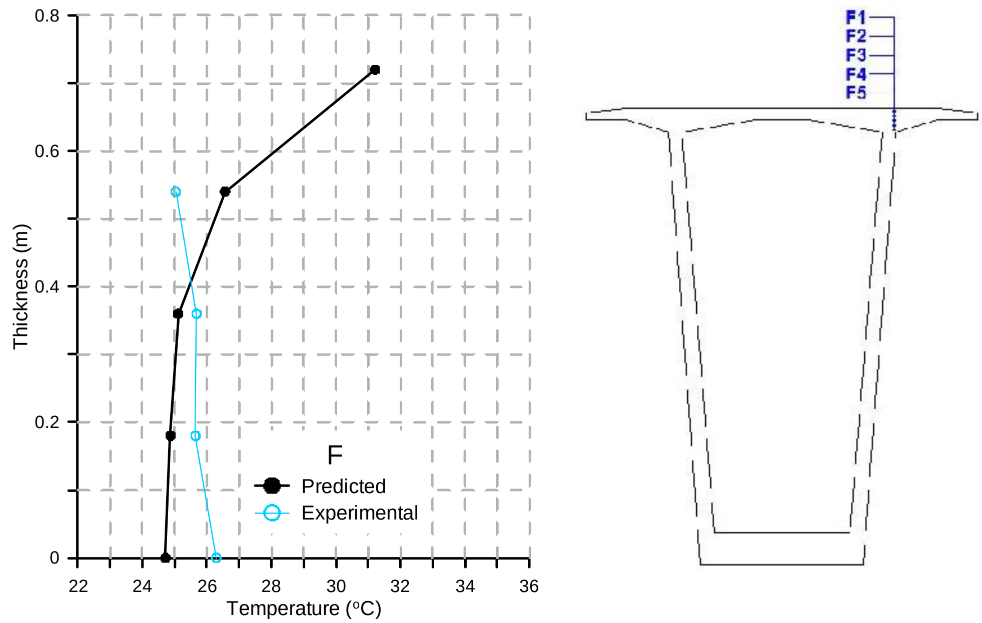

Figure 4.6 Comparison between the FE temperatures and the field temperatures, set (F)

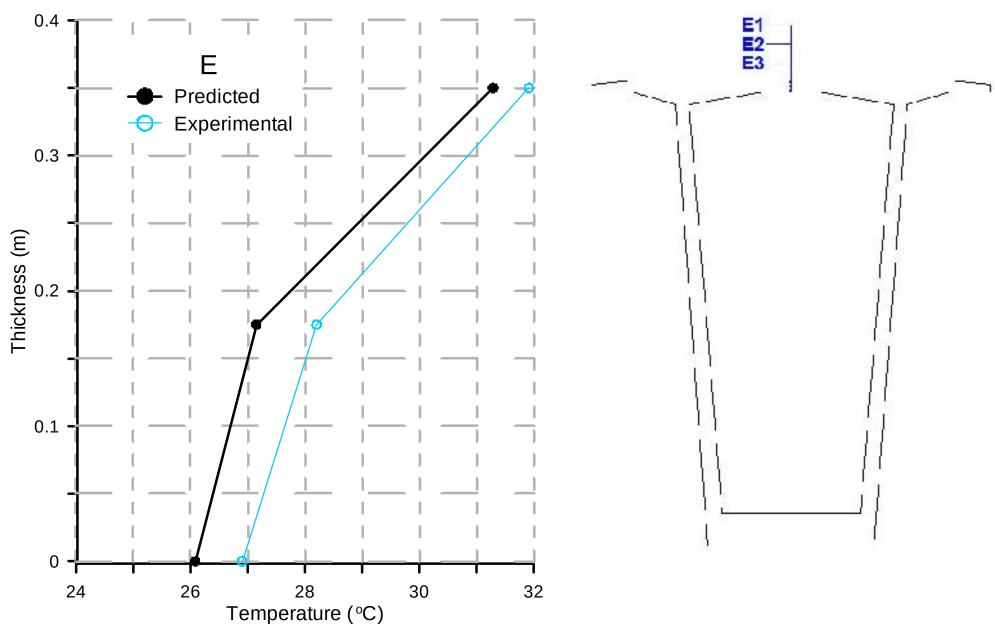

Figure 4.7 Comparison between the FE temperatures and the field temperatures, set (E)

Figure 4.7 illustrates the predicted and measured temperatures across the top flange thickness in the middle width of the top flange. The largest difference of 1.04 °C occurred at the internal surface of the top flange (thermocouple E2), while the smallest difference of 0.62°C occurred at the top surface (thermocouple E1). Therefore, the values of the vertical temperature differences predicted by the numerical study agree well with those obtained from the experimental site.

Figures 4.8 and 4.9 shows the predicted and measured transverse temperatures for the two sets of thermocouples (C and B) through the southeast wall thickness of the study section, on August 9 at 13:00. The set C located at 1.0 m below the top surface of the top flange, while the set B located at 1.5 m above the bottom surface of the bottom slab. From Figure 4.8, it can be seen that the largest difference of 0.46 °C occurred at the internal surface (thermocouple C2), while the smallest difference of 0.17°C occurred at the external surface (thermocouple C1). As shown in Figure 4.9 the largest difference in the transverse temperatures was 1.67°C and occurred at the internal surface (thermocouple B2), while the smallest difference of 0.32°C occurred at the external surface (thermocouple B1). Therefore, the transverse temperature differences at the two locations of the southeast wall predicted by the numerical study agree with those obtained from the experimental site.

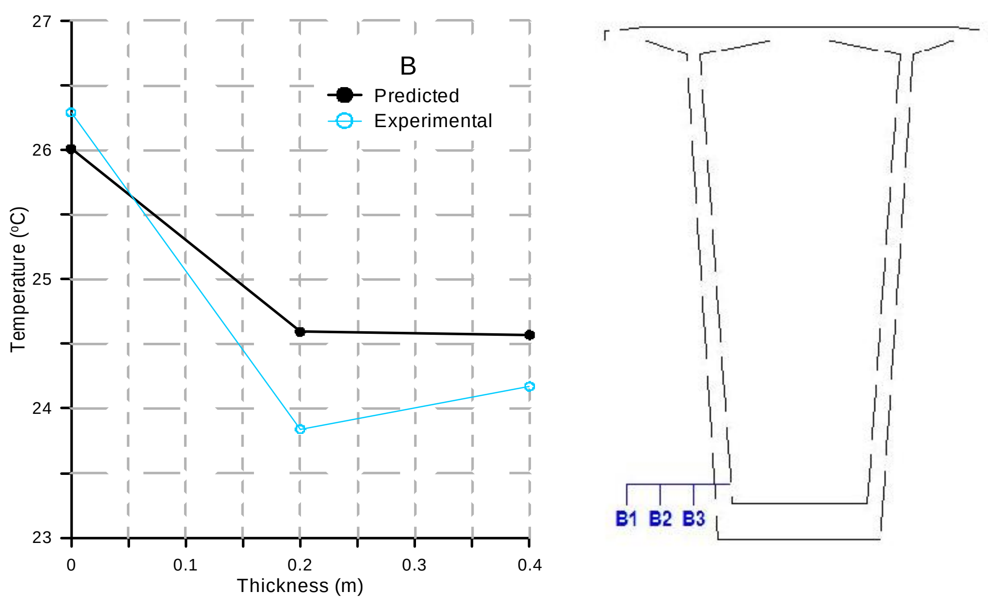

Figure 4.8 Comparison between the FE temperatures and the field temperatures, set (B)

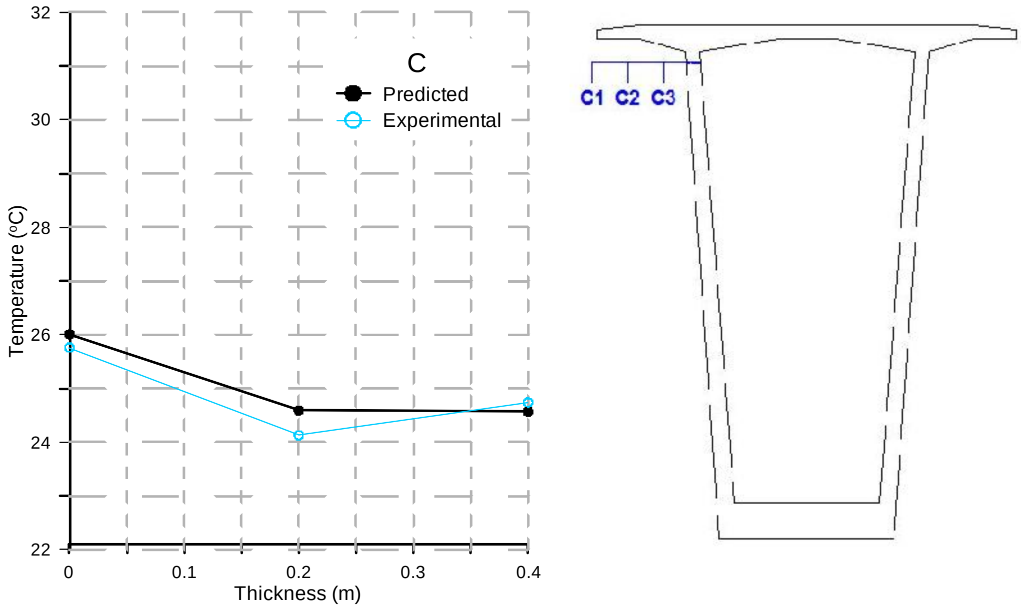

Figure 4.9 Comparison between the FE temperatures and the field temperatures, set (C)

Figures 4.10 and 4.11 compare the predicted and measured transverse temperatures for the two sets of thermocouples (G and H) through the northwest wall thickness of the study section on August 9 at 13:00. The set G located at 1.0 m below the top surface of the upper flange, while the set H located at 1.5 m above the bottom surface of the bottom slab. From Figure 4.10 it is clearly can be seen that the largest difference of 0.17°C occurred at the internal layer of the northwest wall (thermocouple G2), while the smallest difference of 0.07°C occurred at the external surface (thermocouple G1). As shown in figure 4.11, that the largest difference in the transverse temperature distribution was 1.01°C and occurred at the external surface (thermocouple H1), while the smallest difference of 0.57°C occurred at the internal surface (thermocouple H3). As a result, the shapes of the predicted and measured transverse temperature distributions for the two sets of thermocouples (G and H) of the northwest wall agree with the experimental results.

All the above comparisons show clearly match reasonably well between the predicted and experimental results and hence reflect the ability of the current FE model to study and analyze the box-girder sections under the effect of thermal loads effectively.

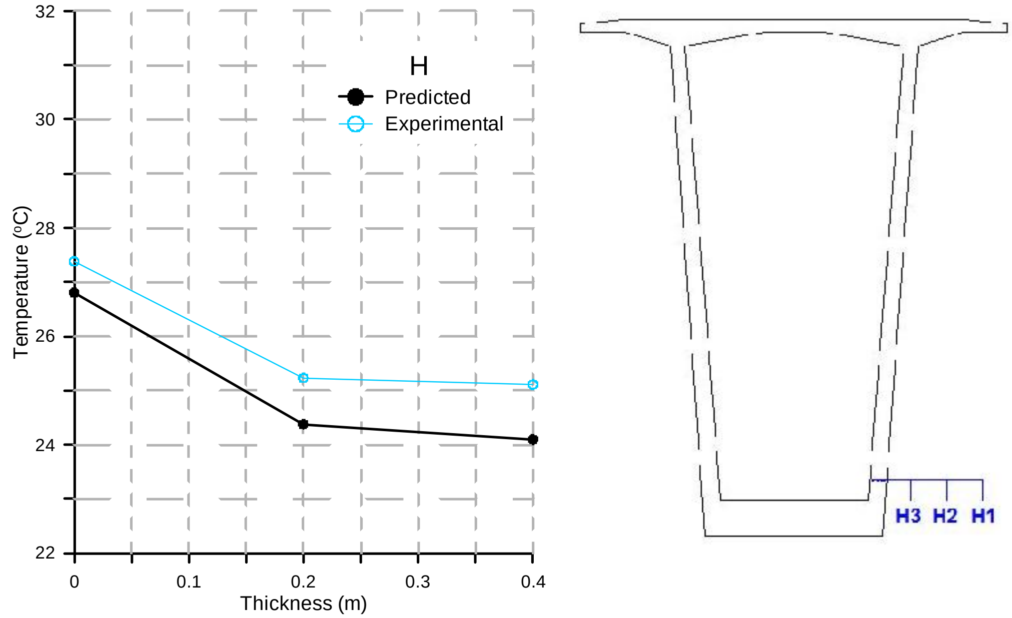

Figure 4.10 Comparison between the FE temperatures and the field temperatures, set (H)

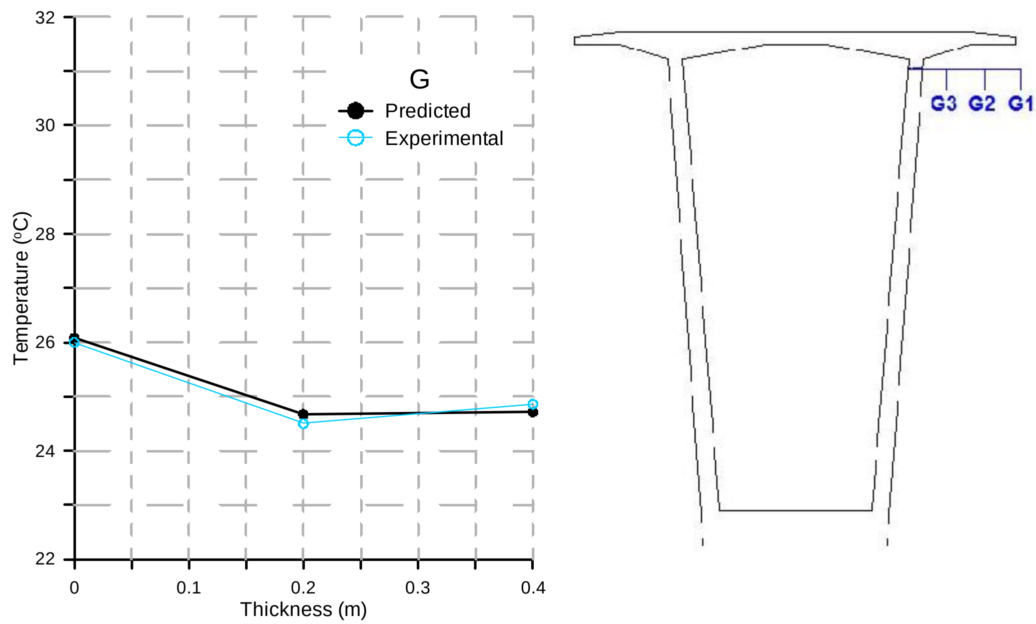

Figure 4.11 Comparison between the FE temperatures and the Field temperatures, set (G)

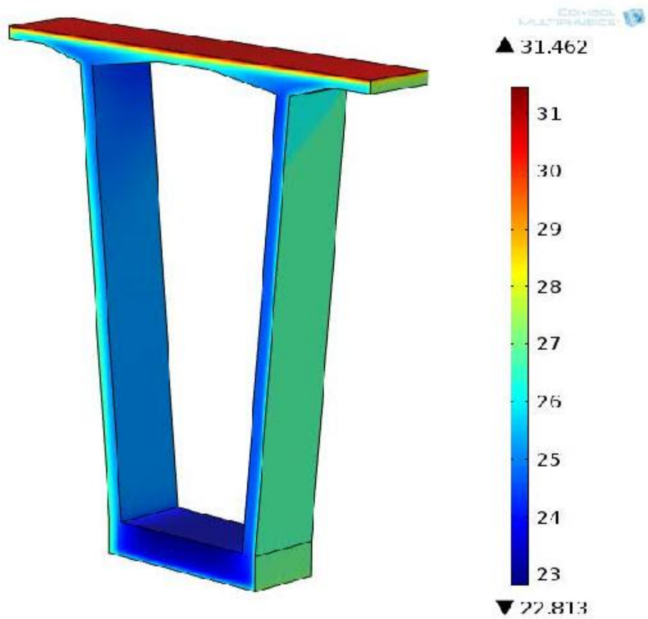

(A)

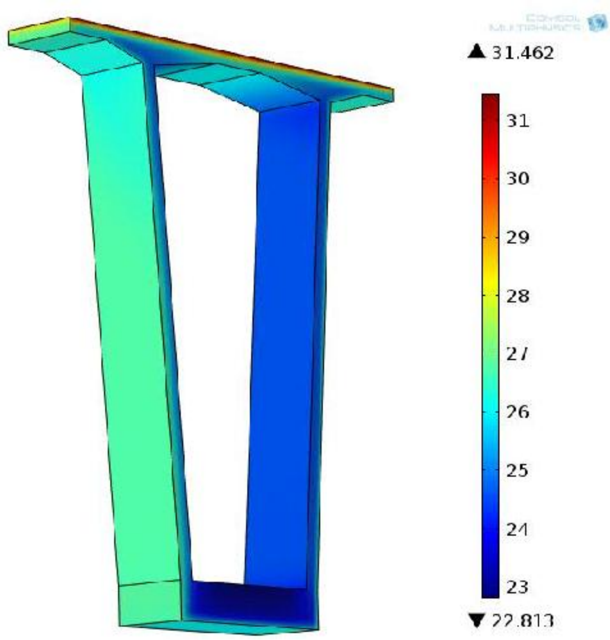

(B)

Figure 4.12 3D FE temperature distributions at 15:00, (A) the southeast face, (B) the northwest face

CHAPTER 5

TEMPERATURE DISTRIBUTIONS AND GRADIENTS IN GAZIANTEP FOR SUMMER CONDITIONS

5.1 General

June 2nd was found to have the maximum hourly total solar radiation incidence on a horizontal surface through the summer weather season, which was 1200 W/m^2. In the same day (June 2), the thermal material properties and thermal loads used in this study are listed in Table 5.1.

Table 5.1 Thermal material properties and thermal loads values

Thermal Conductivity K (w/m K)	Specific Heat C (J/kg K)	Emissivity ϵ	Absorptivity α
1.7	1000	0.85	0.5
Ambient Temperature Max T_a (^{o}C)	Ambient Temperature Min T_a (^{o}C)	Wind speed Min-Max (m/s)	Reflection factor (β)
31.5	12	0.0 - 1.9	0.2

The values of the convection heat transfer coefficient (h_c) for different surfaces of the girder section were calculated using equation 3.7. The latitude and the longitude of the assumed location (Gaziantep, Turkey) are 37° 03' 33" N and 37^o 22' 57" E. The longitudinal axis of the girder model lies on the East-West direction, thus the surfaces of the vertical walls are facing the north and south direction.

A simplification was conducted in the cross section of the top flange to become prismatic with 0.7 m thickness in order to facilitate the numerical analysis, as shown in Figure 5.1. In addition, Figure 5.1 shows the dimensions of the girder model and the locations of the fictitious thermocouples.

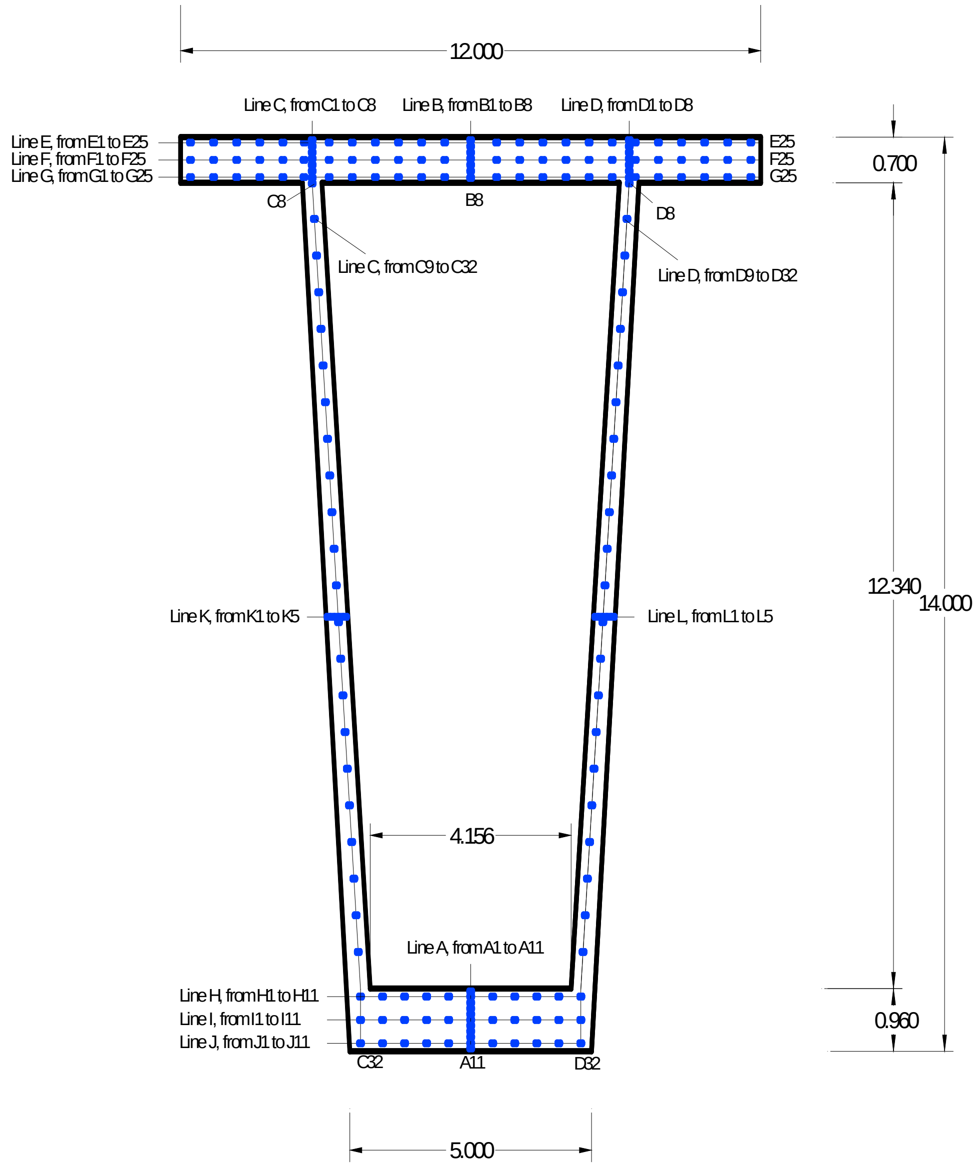

Figure 5.1 Dimension and thermocouples location of FE cross-section
(all dimensions in meter)

5.2 Temperature -Time Curves for Selected Points

The determination of the temperature differentials and the structure response to those temperature differentials was achieved by measuring the changes in temperatures at different locations over the cross-section of the box-girder. During the hot summer days, the bridges structures are exposed to the daily solar radiation, convection heat exchange and re-radiation and hence lead to the largest temperature differential. The influence of these differentials can have important effect on the thermal behavior of the structures. The girder model was almost aligned in the East-West direction, which means that, during the summer days, the sun strikes the top surface and the Southern vertical surfaces more effectively than the northern vertical surfaces. The solar radiation is usually uniform on the top horizontal surface of the top slab during the daily thermal cycle.

The position of the sun during the summer days is of particular importance to find out the received incident intensity and distribution of solar radiation, where the sun rises from the Northeast direction and sets at the Northwest direction during the summer's days.

Another fact worthy of mentioning is that the differences in heat within the cross-section of the concrete bridge are not severe just as in differences in the ambient temperature, this is because concrete is a weak conductor of heat. Thus, the inner concrete layers require more time for heating or for cooling largely.

The box space inside the box-girder is filled with enclosed air, which also is a weak conductor of heat. When the outer bridge boundaries gain heat energy from solar radiation and increase in the ambient air temperature, heat energy is slowly flowing between the inner concrete layers towards the box space.

Figure 5.2 shows the vertical temperature distribution through the thickness of the bottom slab of the box girder on June 2, 2013. The fictitious thermocouples A1, A6, and A11 are located along the depth in the middle of the bottom slab width, where thermocouple A1 located on the top surface of the bottom slab, thermocouple A6 located in the middle of the bottom slab thickness and thermocouple A11 located on the bottom surface of the bottom slab (see Figure 5.1). From Figure 5.2 it can be seen that the minimum temperature in the bottom surface was approximately 18.50 °C at about 05:40, this is because the receiving surface lost its heat to the surrounding environment by re-radiation and convection along cooling phase, followed by a constant increase in the temperature due to the sun's heating effect. The diffuse radiations from the sky and the reflected radiations from the ground and other surrounding objects reach the bottom surface of the bottom slab, which lead to increase the surface temperature continuously until reaching the peak temperature at about 15:00, with a value of approximately 25.80 °C, while the rising of temperature was constant and slight along the daily thermal cycle in the top surface and the mid-thickness of the bottom slab (thermocouples A1 and A6 respectively). Note that the maximum temperature distribution in the bottom surface was greater than those in the top surface by approximately 6.43^{o}C and greater than those in the internal layers of the bottom slab by approximately 5.7^{o}C, this is because the concrete is a weak conductor of heat within the internal layers.

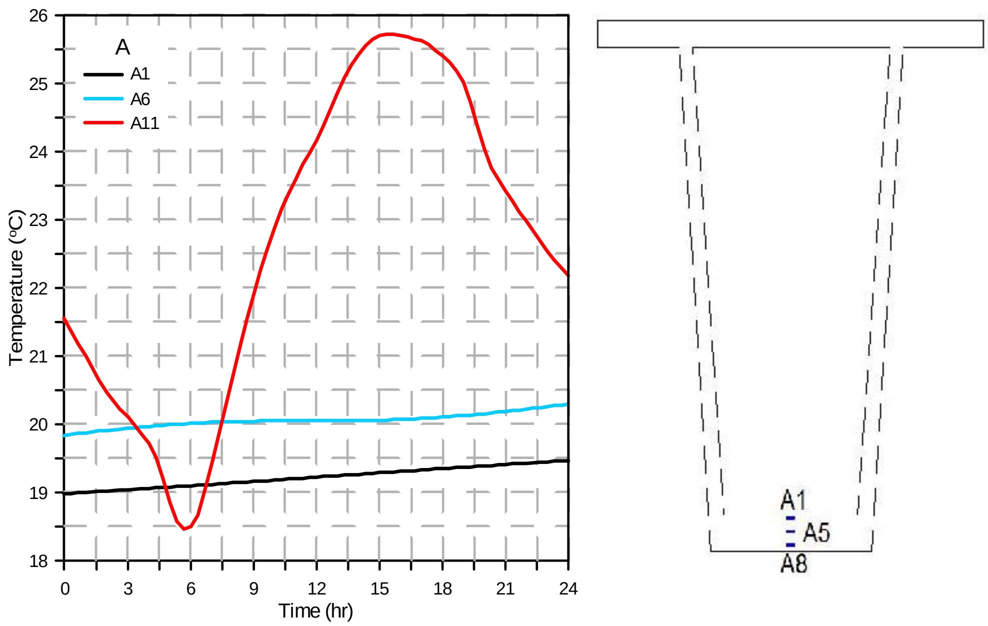

Figure 5.2 Vertical temperature distributions in the bottom slab, set-A

Figure 5.3 shows the vertical temperature distribution through the top slab thickness of the girder model during the daily thermal cycle on June 2, 2013. The fictitious thermocouples B1, B5, and B8 are located along the depth in the middle of the top slab width, where thermocouple B1 is located at the top surface of the top slab and thermocouple B5 is located in the middle of the top slab, while thermocouple B8 is located on the bottom surface of the top slab, (see Figure 5.1). The temperature distribution in the top surface of the top slab (thermocouple B1) was in the lowest level in the early morning about 04:40, which was approximately 23.8°C. After sunrise, the vertical temperature in the middle of the top surface was approximately 26.4^{o}C at 06:00, and then began to climb during the daylight hours until up to a maximum at 13:40, with a value of approximately 52.4°C, this is due to the daily sun movement during the summer days. After 13:40, the temperature began to decrease rapidly, which was 34.2^{o}C at 20:00, this is attributed to that the top surface began to lose its heat by the convection and long-wave radiation to the ambient air.

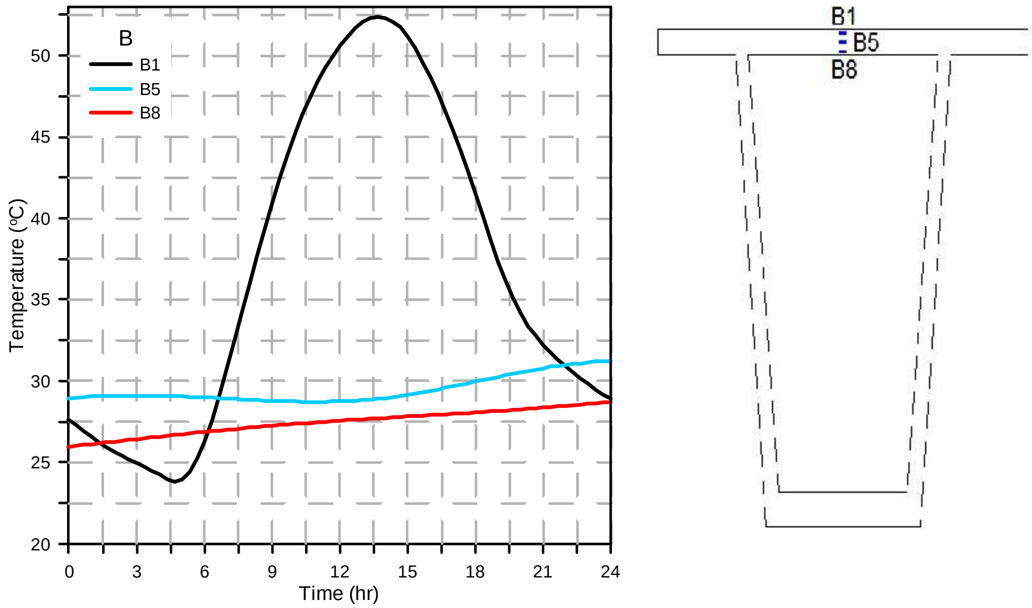

Figure 5.3 Vertical temperature distributions in the top slab, set-B

From Figure 5.3 it can be seen that the vertical temperature distributions increased continuously in the middle of the bottom surface (thermocouple B8) along the daily thermal cycle until reaching a maximum value at 24:00, which was 28.72^{o}C, while the temperature in thermocouple B5 was 29^{o}C at 00:00 and began slightly to increase until at 06:00, which was 28.98^{o}C, then started to decreasing until 11:00, after that increased until 24:00, which was 31.24^{o}C. The maximum value of temperature in thermocouple B1 at 13:40 was greater than those in thermocouples B5 and B8 by approximately 23.5^{o}C and 24.7^{o}C, respectively. This is because the external surfaces and especially the top horizontal surface of the top flange receive direct beam radiation, which raised the temperature of this surface compared with the interior layers.

Figure 5.4 shows the temperature distribution along the 14m depth of the South wall of the girder model during the daily thermal cycle on June 2, 2013. The fictitious thermocouples C1, C5, C8, C10, C22, C27 and C32 are distributed vertically along the depth of the South wall. Where C1, C5, C8 are located across the top slab, C22, C27 and C32 are located across the bottom slab and C10 is located at 2 m beneath the top surface of the top slab, as shown in Figure 5.1.

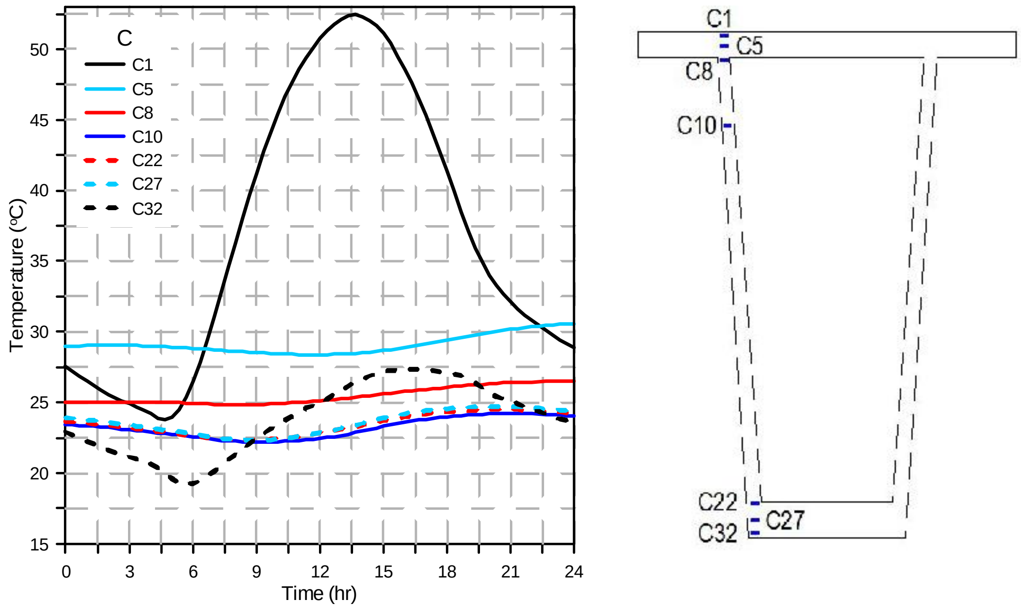

Figure 5.4 Vertical temperature distributions in the south web, set-C

From Figure 5.4 it can be seen that the temperatures of the top surface at the South side were less than those in the lower and internal surface during the night cooling hours, where the minimum temperature value in the top surface was less than 23.8°C at about 04:40, while the temperature distribution in the middle and the bottom surface of the top slab (thermocouples C5 and C8) was 28.95°C and 24.98°C, respectively. The temperature in the internal surfaces (thermocouples C5, C8, C10, C22 and C27) during the early hours morning began to slightly decreasing even to after sunrise, then started to gradually increase along the daily thermal cycle, this is because the relatively low thermal conductivity of concrete, thus the heat flow between the inner layers by conduction is very slow.

In addition, it can be seen from Figure 5.4 that the vertical temperature distribution in the top surface (thermocouple C1) was 26.6°C at 06:00. Following the onset of sunrise, the temperature in the top surface (thermocouple C1) began to increase even reached its maximum value, which was 52.4°C at about 13:40, while the maximum temperature at 2 m beneath the upper surface (thermocouple C10) was 24.23°C at 20:40. The vertical temperature distribution of the top surface begins to decrease immediately after 13:40 along the afternoon hours and during the night hours until reached about 30.83^{o}C at 22:00 and 28.86^{o}C at 24:00. This can be attributed to the amount of solar radiation intensity received by the exterior surfaces, which relies on the position and movement of the sun during the summer's days, as well as, that the top surface during the night cooling hours lost heat energy by the surface convection and long-wave radiation to the ambient air.

From Figure 5.4 it is clearly can be seen that the minimum temperature distribution during the early hours of the morning across the thickness of the bottom slab in the southern side was in the bottom surface, which was 19.25^{o}C at 06:00, while the temperature distribution in the top surface and the middle point of the bottom slab was 22.75^{o}C and 22.64^{o}C, respectively.

The outer lower surface of the bottom slab only receives the diffuse radiations from the sky and reflected radiations from the earth's surface and the other surrounding objects. The temperature distribution was less than those in any external surface in the other three walls (top slab, South wall and North wall). Hence, the outer lower surface of the bottom slab has the lowest temperatures compared with the other exterior surfaces, where the maximum temperature distribution in the lower surface of the bottom slab was less than that in the upper surface of the top slab by approximately 25.12^{o}C.

Figure 5.5 shows the vertical temperature distribution along the 14m depth of the North wall of the box-girder section during the daily thermal cycle on June 2, 2013. The fictitious thermocouples D1, D5, D8, D10, D22, D27 and D32 are located vertically along the depth of the North wall, where D1, D5, D8 are located across the top slab in the North side and D22, D27 and D32 are located across the bottom slab in North side and D10 is located at 2 m beneath the top surface of the top slab.

From Figure 5.5 it can be seen that the top surface of the top slab lost heat to the surrounding environment by the surface convection and long-wave radiation along the cooling hours, the minimum value of the temperature was 23.8^{o}C at 04:40, and its maximum value was 52.4^{o}C at 13:40. The minimum temperatures in the interior layers (thermocouples D5, D8, D10) were 28.7^{o}C at 11.40, 25.7^{o}C at 08:20 and 24.6^{o}C at 06:00, respectively. The maximum temperatures in the interior layers of the top slab (thermocouples D5 and D8) and (thermocouple D10) were 30.9°C at 24:00, 25.8°C at 11.20 and 26.9°C at 21:20, respectively.

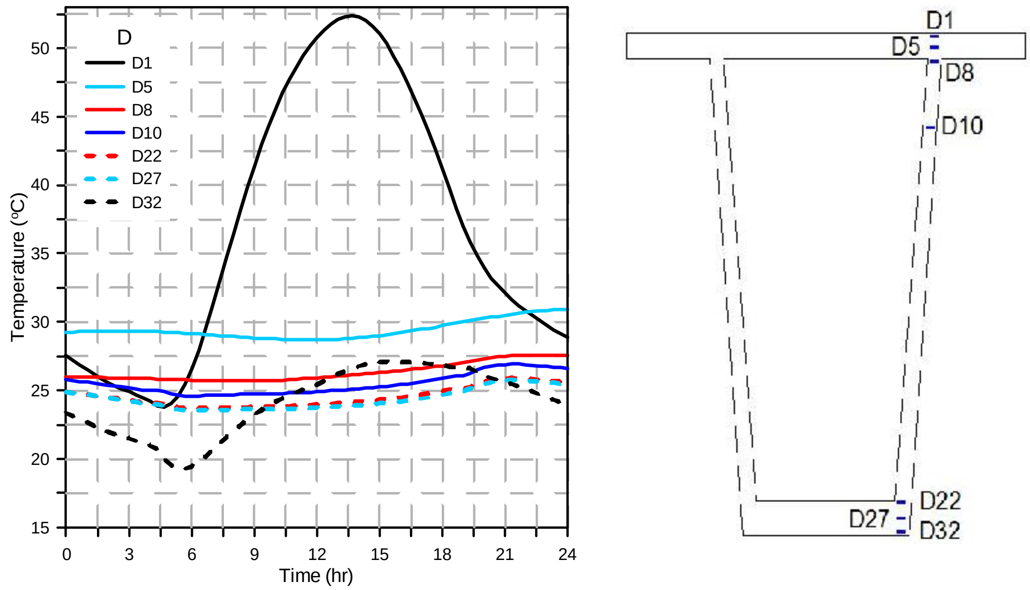

Figure 5.5 Vertical temperature distributions in the North web, set-D

In addition, it may be observed from Figure 5.5 that the temperature distribution in the bottom surface of the bottom slab suffered from the occurrence of the significant temperature variations more than those in the internal surfaces of the bottom slab, this can be attributed to the effect of the variation in ambient temperature and the reflected radiations from the earth's surface and the objects surrounding the bridge.

The maximum temperature in the bottom surface was 27°C at 15:20 PM and the minimum temperature in the bottom surface was 19.3°C at about 04:40, while the maximum temperatures in the interior layers (thermocouples D22 and D27) were 25.9°C at 19:40 and 25.7°C at 22:00, while the minimum temperatures in thermocouples D22 and D27 were 23.7°C at 06:00 and 23.5°C at 06:20.

Figure 5.6 shows the transverse temperature distribution along the width of the top slab at different locations from the top surface during the daily thermal cycle on June 2, 2013. The fictitious thermocouples E1, E13, and E25 were distributed horizontally along the line E1-E25, which is located at 0.2 m below the top surface along the width of the top slab. As shown in Figure 5.1, thermocouple E1 is located in the upper part of the vertical southern edge in the top slab, E25 is located in the upper part of the vertical northern edge in the top slab and E13 is located in the middle of line E1- E25.

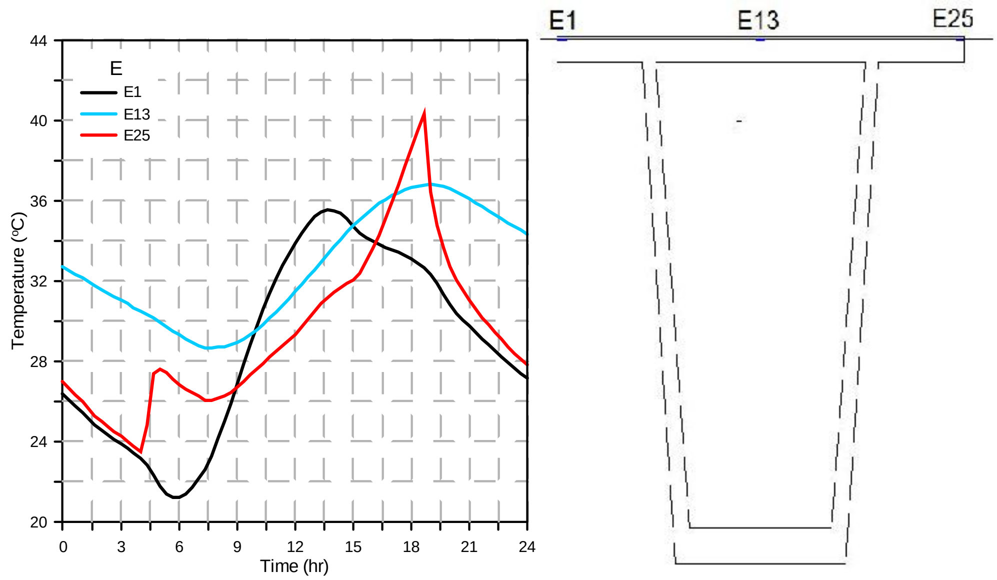

Figure 5.6 Transverse temperature distributions along line E1-E25

From Figure 5.6 it can be seen that the temperatures in thermocouples E1 and E25 started to decrease in the northern and southern edge during the cooling hours, because the exterior surfaces lost heat energy by the cooling surface convection and re-radiation.

In the onset of the sunrise, and because the sun rises from the Northeast direction, the sun radiates the vertical northern faces with lower solar radiations while the vertical southern faces are entirely shaded, hence the temperatures in thermocouple E25 were greater than those in thermocouple E1 along the early morning hours until at about 09:00. The temperature of the southern edge began to increase at around 08:40 until reached its maximum value at 13:40, with a value of approximately 35.5°C and then started to decrease along the afternoon hours and the night hours, this can be attributed to the effect of the daily movement of the sun during the summer's days, which is still even at the midday to the South direction in the E-W plane making the southern faces receive more solar radiation than the northern faces.

Figure 5.6 shows that the transverse temperatures in the middle of the top surface (thermocouple E13) along the night cooling hours and during the first daytime hours until at about 10:00 were greater than those in the southern edge (thermocouple E1), while they were greater than those in the northern edge (thermocouple E25) along the night cooling hours and during the daytime hours until about17:20. Moreover, the largest temperature in thermocouple E13 was 36.8^{o}C at 19:00, while the largest temperature in thermocouple E25 was 40.3^{o}C at 18:40. After that, the temperature decrease rapidly at the onset of the sunset at approximately 18:40.

Figure 5.7 shows the transverse temperature distributions in the middle of depth and along the top slab width during the daily heating and cooling cycle on June 2, 2013. Fictitious thermocouples F1, F13, and F25 are distributed horizontally along the line F1-F25, which is located along the centerline of the top slab width, As shown in Figure 5.1, thermocouple F1 is located in the center of the vertical southern edge of the top slab, F25 is located in the center of the vertical northern edge of the top slab and F13 is located in the center of the line F1- F25.

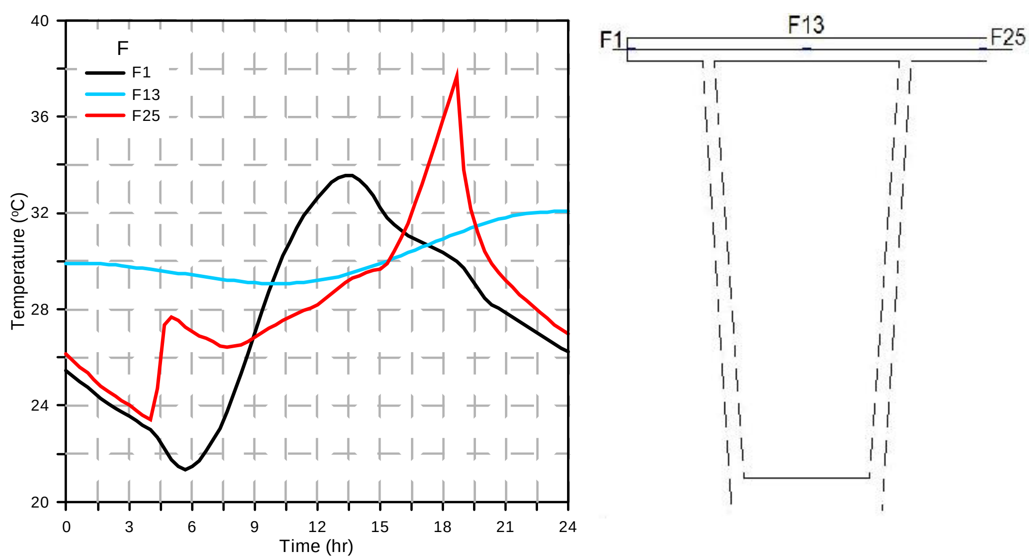

Figure 5.7 Transverse temperature distributions along line F1-F25

From Figure 5.7, it can be seen that the temperatures in the vertical southern side (thermocouple F1) were less than those in the vertical northern side (thermocouple F25) along the cooling phase and during the early morning hours until about 09:00. On the other hand, they were less than those in the central point on the line F1-F25 (thermocouple F13) until about at 10:00. The minimum value of the temperature in thermocouple F1 was 21.3^{o}C at 05:40. Afterwards, the temperature in the vertical southern face (thermocouple F1) started to increase until reaching its maximum value of 33.6°C at 13:20 and then began to decrease along the remaining time from the daily thermal cycle, where it was 29.7°C at 19:00, 27.9°C at 21:00 and 26.2°C at 24:00.

It is clear from Figure 5.7 that the temperature in the central point (thermocouple F13) was 29.9°C at 24:00 and then decreased until reached its minimum value, which was 29.°C at 22:00. At this time, the readings of thermocouple F13 started to increase until reached its maximum value, which was approximately 32°C at 24:00.

It can be seen from Figure 5.7 that the temperatures in the northern side were greater than those in the southern side during the late hours of the afternoon (which started about 16:20) and during the night cooling hours. The largest temperature distribution in thermocouple F25 was 36.7 at 18:40. After that, the temperature began to decrease rapidly at the onset of sunset approximately 18:40, while the minimum temperature in thermocouple F25 was 23.4°C at 16:00.

Figure 5.8 shows the transverse temperature distributions along the width of the top slab at different locations and during the daily heating and cooling cycle on June 2, 2013. The fictitious thermocouple G1 is installed in the lower part of the vertical southern edge of the top slab, G25 is installed in the lower part of the vertical northern edge of the top slab and G13 is located in the middle of line G1-G25, which is located at 0.2m above the bottom surface of the top slab.

As shown in Figure 5.8, the transverse temperature in the middle of bottom surface tends to be having a continuous and constant increase along the daily thermal cycle. It can be seen from Figure 5.8 that the temperature in the southern side first decreased along the cooling phase until reaching its minimum value at 05:40, which was 20.5°C, then began to increase until reached its maximum value at 13:20, which was approximately 32.9°C. After that, the temperature began to decrease until reaching low values during the afternoon hours and the night hours, these were 30.53°C at 16:00, 29.4°C at 18:00, 27.5°C at 20:00 and 25.24 at 24:00, while the temperature in the northern side has first decreased to its minimum value at 04:00, which was 22.5°C. Then began to increase until reached its maximum value at 18:40, which was 36.8°C, after that began to increase until reaching its minimum value, which was 26°C at 24:00.

From Figure 5.8, it can be seen that the temperatures in the vertical northern side were greater than that in the southern side along cooling phase to about 09:00 in addition to the last hours before the sunset at about 16:20 and during the night hours, while the temperatures in the southern side were greater than those in the northern side from about 09:00 to approximately 16:20. This is due to the effect of the complicated movement of the sun on the received intensity of solar radiation by the outer surfaces of the girder section.

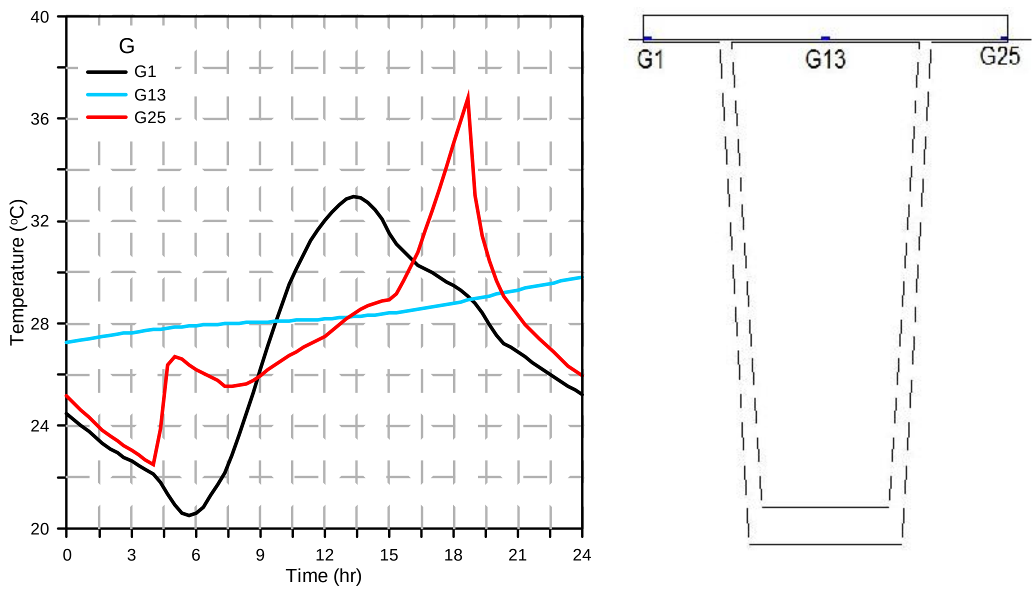

Figure 5.8 Transverse temperature distributions along line G1-G25

Figure 5.9 shows the transverse temperature distributions along the width of the top part of the bottom slab in different locations during the daily thermal cycle on June 2, 2013. The fictitious thermocouple H1 is located in the upper part of the vertical southern edge in the bottom slab, H11 is located in the upper part of the vertical northern edge in the bottom slab and H6 is located in the middle of line H1- H11, which is located at 0.16 m below the top surface of the bottom slab.

From Figure 5.9 it can be seen that the transverse temperature distribution in the inner surfaces (thermocouple H6) of the bottom slab was almost uniform during the daily thermal cycle, while the temperature distribution in the northern and southern faces (thermocouples H1 and H11) were unsteady along the daily thermal cycle. The minimum and the maximum temperatures in the central point (thermocouple H6) were 19^{o}C at 00:00 and 19.6^{o}C at 24:00, respectively.

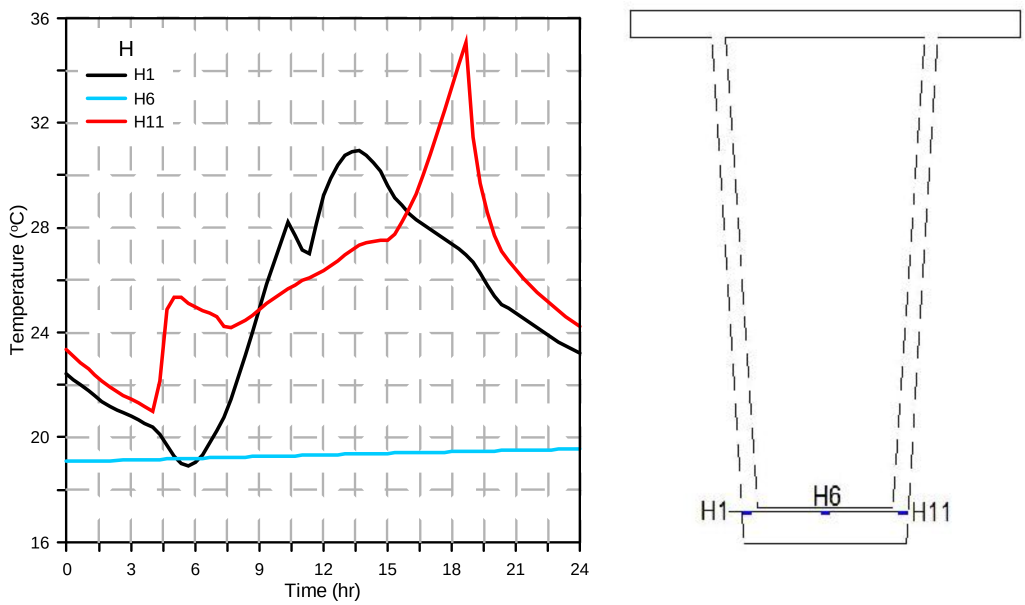

Figure 5.9 Transverse temperature distributions along line H1-H11

As shown in Figure 5.9, the temperature in the northern face increased at 04:20 and then began to decrease at 04:40 until about 07:30. This is because the sun rises from the Northeast direction and moves from North to South direction towards zenith-EW plane, where the path of the sun crosses this plane twice every day. The first at about 09:00 and the second at about 15:00. Therefore, the sun radiates the southern faces more than the northern faces from about 09:00 to about 15:00. The maximum and the minimum temperature in the southern edge was 31^{o}C at 13.40 and 19^{o}C at 05:40, while the maximum and minimum temperatures in the northern edge were 35^{o}C about 16:40 and approximately 21^{o}C at 04:00.

Figure 5.10 shows the transverse temperature distributions in the middle of depth and along the bottom slab width during the daily heating and cooling cycle of June 2, 2013. Thermocouple I1 is located in the center of the vertical southern face, I11 is located in the center of the vertical northern face and I6 is located in the center of the line I1- I11, which is located in the middle of the depth along the bottom slab width.

As shown in Figure 5.10, the transverse temperature distributions in the central point (thermocouple I6) were increased continuously and slightly along the daily thermal cycle, while the temperatures in the vertical external faces of the bottom slab were unsteady during the daily thermal cycle. The maximum and the minimum temperatures in the northern edge were 34.7°C at 18:40 and 21.06°C at 04:00 and they were 31°C at 13:40 and 19°C at 05:40 in the southern edge, while the maximum and the minimum temperatures in the central point (thermocouple I6) were 20.3°C at 24:00 and 19.8°C at 00:00, respectively.

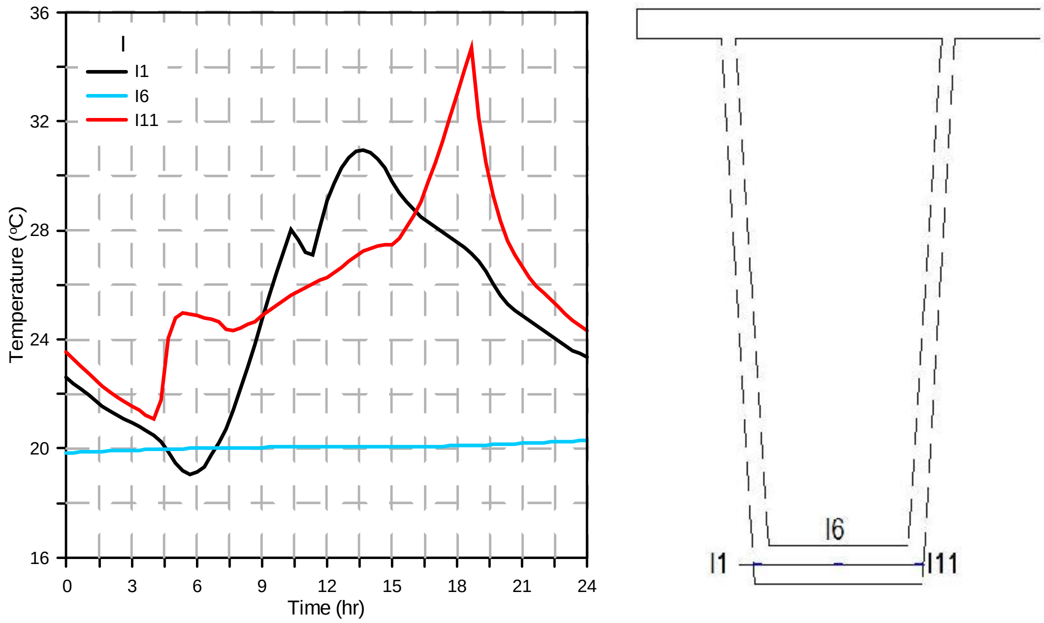

Figure 5.10 Transverse temperature distributions along line I1-I11

Figure 5.11 shows the transverse temperature distribution along the width of the bottom slab at different locations of the bottom surface during the daily thermal cycle on June 2, 2013. Thermocouple J1 is installed in the lower vertical southern edge, J11 is installed in the lower vertical northern edge and J6 is located in the middle of line J1- J11, which is located at 0.2 m above the bottom surface of the bottom slab. It can be seen From Figure 5.11 that the minimum temperature during the cooling hours in the exterior surfaces of the bottom slab was recorded in the lower southern edge (thermocouple J1), with a value of approximately 18.9°C at 05:40, while the minimum temperatures were 20.9°C at 04:00 in the lower northern edge (J11), and 20.6°C at 09:20 in the middle of the bottom surface (J6). Figure 5.11 illustrates that the transverse temperature distribution in the middle of the bottom surface climbed from about 20°C at 09:40 during the heating cycle to a peak of 22.3°C in the late night (22:20). The maximum temperatures in the lower northern edge and lower southern edge were 35.3°C at 18:40 and 31°C at 13:40, respectively.

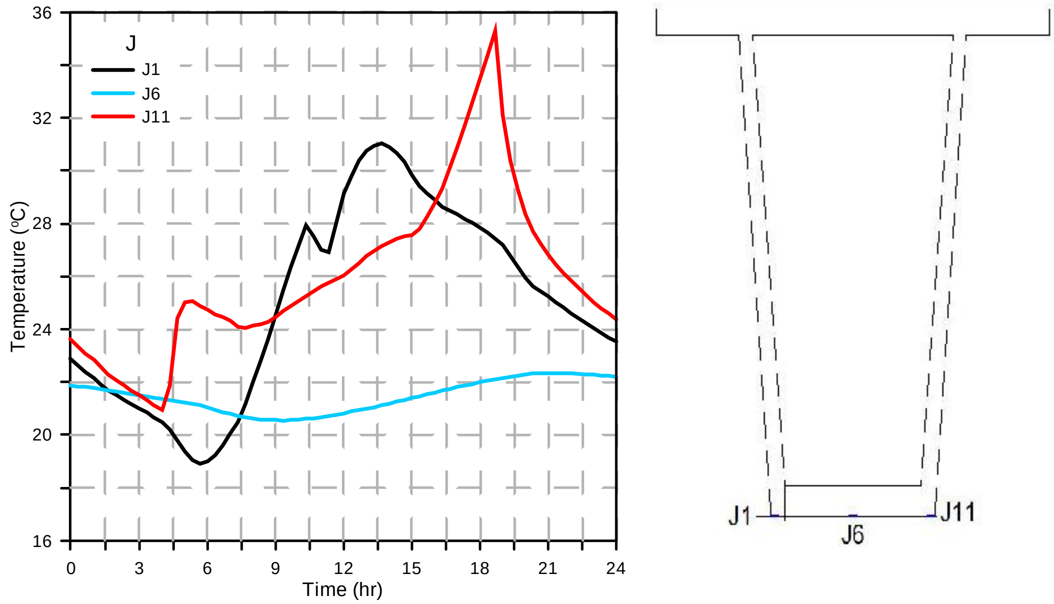

Figure 5.11 Transverse temperature distributions along line J1-J11

Figure 5.12 shows the transverse temperature distributions across the South wall thickness at different locations during the daily thermal cycle on June 2, 2013, where the thermocouple K1 is located on the exterior surface of the South wall, thermo-couple K3 is located in the middle of the wall thickness and K5 is located on the interior surface of the South wall.

From Figure 5.12 it can be seen that from the start of the daily thermal cycle, the exterior surface lost heat to the surrounding environment by convection heat exchange and re-radiation. As well as, the central area lost heat to the interior layers by conduction heat transfer, while the interior surface gained heat energy by conduction. This is because the heat energy is transferred from a high-temperature region to a low-temperature region. Figure 5.12 shows that the temperature in the internal surface (thermocouple K5) started to increase during the cooling phase until about 04:40 and then it decreased to the lowest value of approximately 23°C at 13:40. After that, it climbed to the maximum value, which was approximately 24°C about 24:00. On the other hand, the temperature of the exterior surface was the lowest in the early morning (about 5:40), with a value of approximately 18.6°C. The temperature was then climbed during the daytime to a peak of approximately 29.8°C at about 13:40. The maximum and the minimum temperatures in the central area were 25^{o}C at about 20:20 and 22.3^{o}C at about 08:40, respectively.

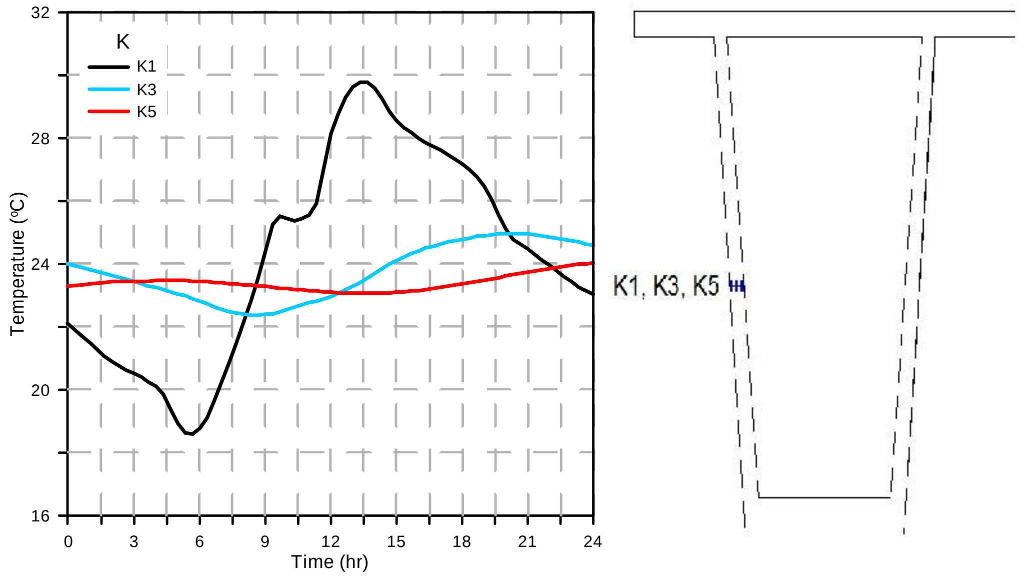

Figure 5.12 Transverse temperature distributions in the south web, set K

Figure 5.13 shows the transverse temperature distributions through the North wall thickness at different locations during the daily thermal cycle on June 2, 2013, where the fictitious thermocouple L1 is located on the exterior surface of the North wall, thermocouple L3 is located in the middle of the wall thickness and thermocouple L5 is located on the interior surface of the North wall.

It can be seen from Figure 5.13 that the transverse temperature distribution in the exterior surface tended to decrease during the cooling hours of the night until amounted the minimum value of about 20.5^{o}C at 04:20, and then the temperature of the exterior surface rose from the onset of the sunrise to about 05:20, with a value of about 25.9^{o}C. Thereafter began to decline until amounted its value of about 24.2^{o}C at 07:40 and then climbed to its greatest value at the sunset about 18:40, which was approximately 36.4^{o}C. The temperature in the central area decreased during the cooling phase to the lowest value of approximately 24.4^{o}C at about 05:20, then rose to the largest value of approximately 27.2^{o}C at 21:00 and then began to decrease during the late hours of the night. The transverse temperature distribution in the inner surface (thermocouple L5) was almost steady along the daily thermal cycle, it can be seen from Figure 5.13 that it started to decrease until about 06:00 with a value of approximately 25^{o}C then tended to increase to a value of approximately 24.8^{o}C at 13:00 and then increased to maximum value, which was 25.7^{o}C at 24:00.

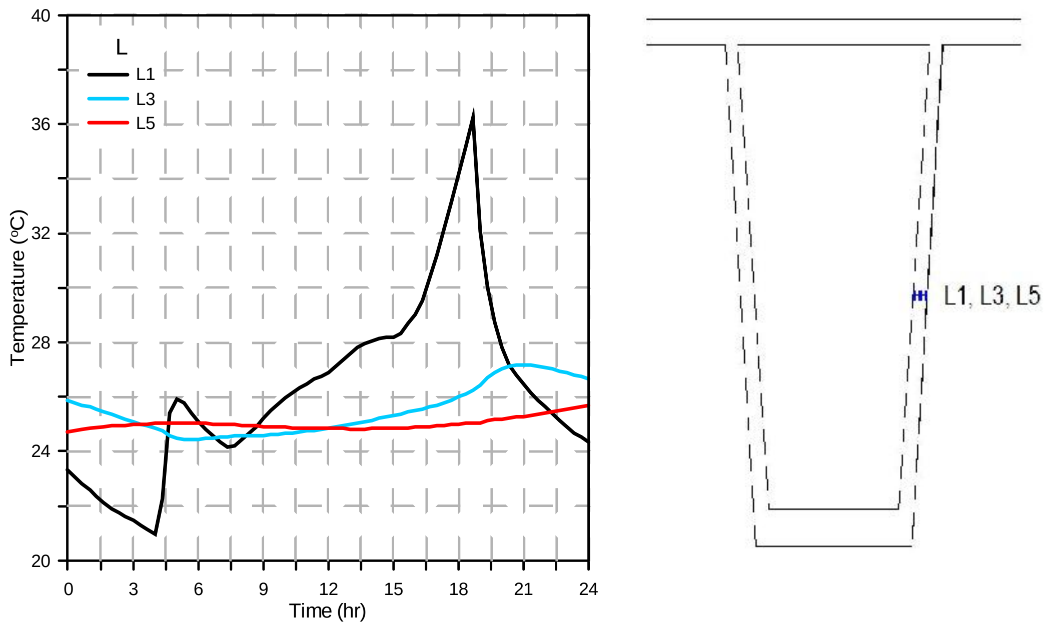

Figure 5.13 Transverse temperature distributions in the north web, set-L

5.3 Temperature Distributions at Different Time Steps

Figure 5.14 illustrates the vertical temperature distribution across the bottom slab at the three time steps 06:00, 14:00 and 20:00. Originally, temperature on the bottom surface was lower than those in the inner layers at 06:00, which was 18.5^{o}C. At the same time, the largest temperature was approximately 21.03^{o}C, which is located 0.2 m above the bottom surface, while the maximum surface temperature was 25.42^{o}C at 14:00 and occurred at the bottom surface of the slab. As shown in Figure 5.14, the largest difference of temperature between the exterior surface and the interior surface of the bottom slab was 6.2^{o}C, which occurred at 14:00. It can be seen from Figure 5.14 that the largest temperature in the top surface was 19.4^{o}C and occurred at 20:00, while it was approximately 19.3^{o}C at 14:00 and about 19^{o}C at 06:00.

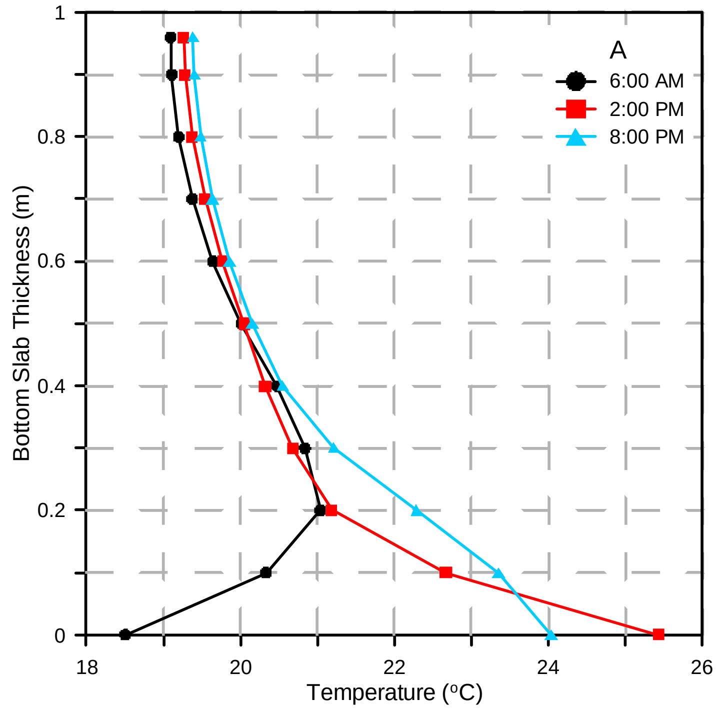

Figure 5.14 Vertical temperature distributions in the bottom slab at different time steps

Figure 5.15 shows the vertical temperature distribution across the top slab at three time steps 06:00, 14:00 and 20:00. As shown in the Figure, the largest surface temperature occurred at the top surface of the top slab at about 14:00, which was about 52.3°C, while the temperature of the top surface was 34.2°C at 20:00 and 26.4°C at 06:00. After sunset, the top surface began to lose heat by cooling surface convection and re-radiation to the surrounding environment along the cooling phase. Thus, it is clearly shown in the Figure that the largest temperature at 20:00 at 0.1 m beneath the top surface was approximately 37.7°C.

In addition, Figure 5.15 illustrates that the largest difference in the temperature between the top surface and the bottom surface of the top slab was 24.6°C and occurred at 14:00. This is because the outer surfaces of the bridge and especially the top horizontal surfaces are exposed to the direct solar radiation, which makes these surfaces warmer than the interior layers and the bottom surface. It can be seen from the Figure that the temperature of the bottom surface at the three time steps were close to each other's with minor differences where the temperatures were 26.8°C, 27.8°C and 28.3°C at approximately 06:00, 14:00 and 20:00, respectively.

This can be attributed to the effect of the top slab thickness, which is 0.7 m and the thermal conductivity coefficient of concrete, which is only 1.7 W/m K. therefore it is not enough to transfer the temperatures from the outer surfaces to the inner surfaces. In addition to the effect of the enclosed air in the box space inside the box-girder, where the enclosed air is considered as a weak conductor of heat and hence it makes the temperature variations in the interior surfaces of the box-girder more moderate during the daily thermal cycle.

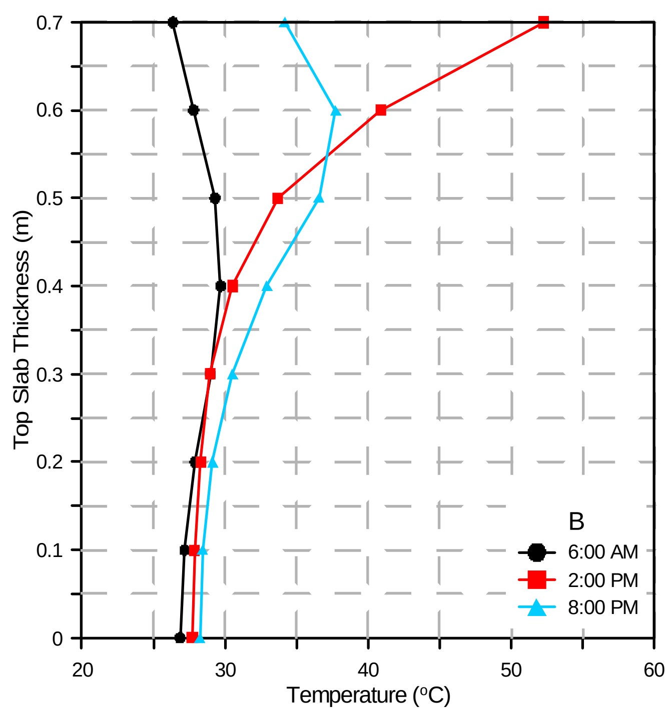

Figure 5.15 Vertical temperature distributions in the top slab at different time steps

Figure 5.16 illustrates the vertical temperature distributions along the 14m depth of the South wall of the 3D FE model at different time steps 06:00, 14:00 and 20:00. The minimum temperature of the top surface was 26.5℃ and took place at 6:00, while the temperature in an interior layer at 0.3 m beneath the top surface was about 29.8℃ as shown in Figure 5.16. The largest temperature in the top surface was 52.3^{o}C at 14:00, while the temperature at 0.2 m beneath the top surface was 33.6^{o}C. This high difference in temperature is due to the high intensity of solar radiation, which strikes the top horizontal surface during the midday hours, thus the largest differences of the temperature occurred between the top surface and the interior layers of the slab and the wall. After sunset, the top horizontal surface began to lose its heat by the convection and the re-radiation to the surrounding environment and this continued during the night cooling hours, as described in the vertical temperature distribution at 8:00 shown in Figure 5.16.

It can be seen from Figure 5.16 that the vertical temperature distribution was almost constant along the depth of the wall, which is extended from the bottom surface of the top slab to the upper surface of the bottom slab, where the temperature at 1.0 m beneath the top surface of the top slab was 23°C, 23.6°C and 24.2°C at 06:00, 14:00 and 20:00 respectively.

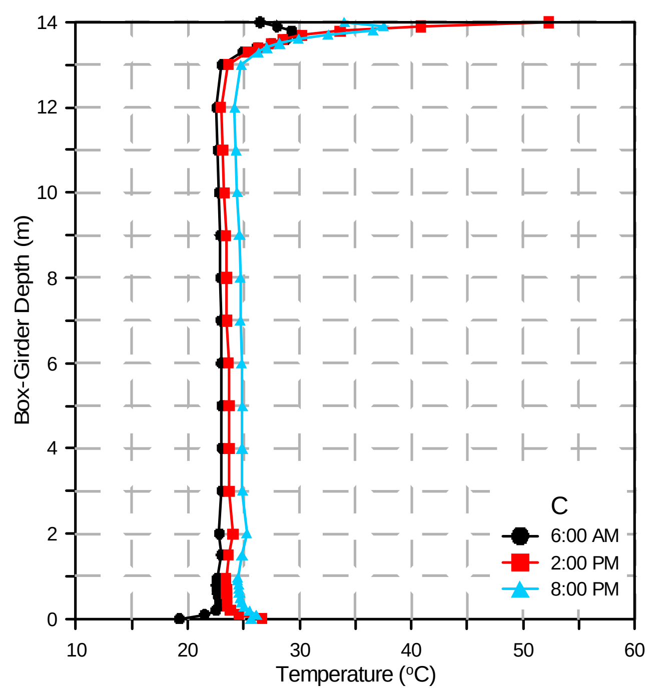

Figure 5.16 Vertical temperature distributions along the south web at different time steps

As described in Figure 5.16 it can be seen that the vertical temperature distribution across the bottom slab varies from a time step to another, the temperature in the bottom surface was lower than those in the inner layers at 06:00, which was 19.2°C, the temperature was approximately 22.9°C at 0.3 m above the bottom surface.

The largest temperature in the bottom surface at 14:00 was 26.65°C, while at the same time, the temperature at 0.3 m above the bottom surface was about 23.8°C. This is because of the effect of the diffuse solar radiation, the hot ambient temperature and the reflected radiation from the earth's surface and other objects surrounding the bridge structure.

Figure 5.17 shows the vertical temperature distribution along the 14m depth of the North wall of 3D FE model at different time steps 06:00, 14:00 and 20:00. It is shown in the Figure that the largest temperature of the top horizontal surface of the top slab at the northern side occurred at 14:00, with a value of 52.2^{o}C, whereas the lowest temperature occurred at 06:00 with a value of approximately 26.6^{o}C.

Due to the fact that concrete is a weak conductor of heat, therefor the inner concrete layers retain with heat energy for a long time. As shown in the vertical temperature distribution at different time steps shown in Figure 5.17, the vertical temperature distributions were almost constant along the depth of the North wall. It should be noted that the temperatures at 1.0 m beneath the top surface of the top slab were 24.6^{o}C, 24.9^{o}C and 26.8^{o}C at 06:00, 14:00 and 20:00, respectively.

As shown in Figure 5.17, the lowest temperature in the bottom surface of the bottom slab at the North side was 19.4^{o}C, occurred at 06:00, while the largest temperature was 26.8^{o}C and occurred at 14:00. At the same time, the temperature at 0.3m above the bottom surface was 23.8^{o}C.

As shown in Figure 5.17, the largest difference in temperature between the top surface of the top slab and bottom surface of the bottom slab was 28.4^{o}C and occurred at 14:00.

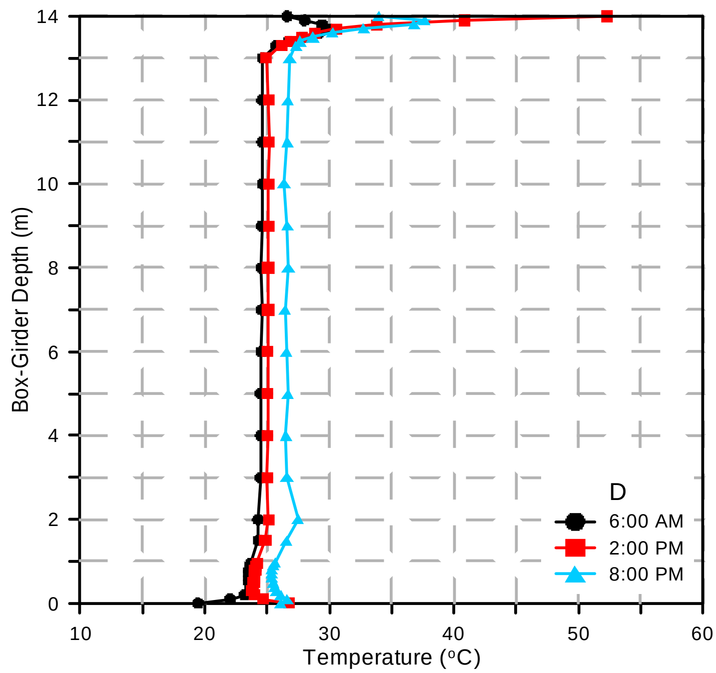

Figure 5.17 Vertical temperature distributions along the north web at different time steps

Figure 5.18 shows the transverse temperature distributions along the centerline of the 12 m width of the top slab at different time steps 06:00, 14:00 and 20:00. At 06:00, from the Figure it can be seen that for each of the three time steps, the temperature distributions were almost the same along the central width of the top slab, while sharp variations in the surface temperature occurred along the edge of the South wing of the top slab and little variations in the surface temperature occurred along the North wing of the top slab.

At 06:00, the surface temperature at the southern edge increased from the minimum value of 21^{o}C to 29^{o}C at 0.5 m away from the southern edge, while the temperature difference was only about 3^{o}C along the northern edge. Furthermore, the surface temperature at the northern side was greater than those in the southern side by approximately 5.6^{o}C. This is because the sun rises from Northeast direction during the summer days.

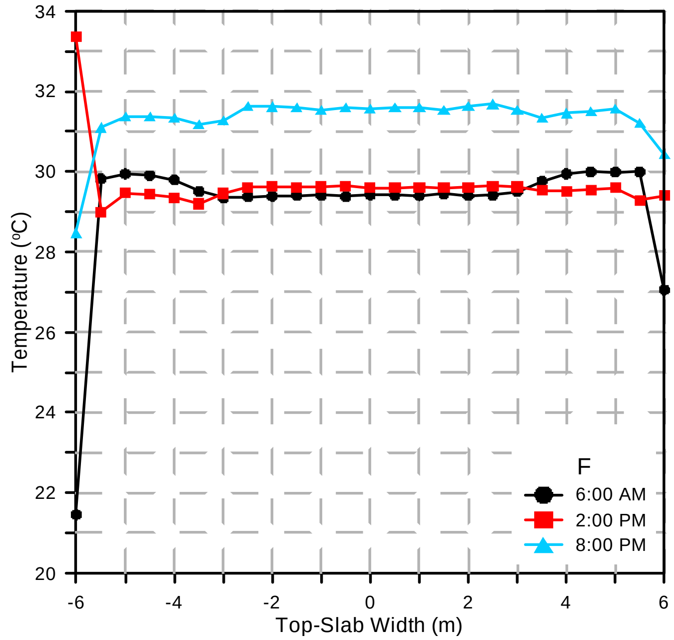

Figure 5.18 Transverse temperature distributions along the centerline of the 12 m width of the top slab width at different time steps

As shown in Figure 5.18, the surface temperature decreased from the maximum value of approximately 33.4℃ at southern edge at 14:00 to about 19.00 at 0.5 m away from the southern edge, while the temperature difference was only 0.2℃ along the northern edge.

At 20:00, the temperature increased from approximately 28.5^{o}C at the southern edge to about 31^{o}C at 0.5 m away from the southern edge, while the temperature difference was only 0.8^{o}C along the northern edge.

Figure 5.19 shows the transverse temperature distributions along the centerline of the 5 m width of the bottom slab at different time steps 06:00, 14:00 and 20:00. As shown in the Figure, the temperature distributions during the three time steps were almost identical and steady along the central width of the bottom slab, while sharp variations in the surface temperature occurred along the vertical southern edge and minor variations in the surface temperature occurred along the northern edge. The maximum surface temperature at the southern edge was approximately 30.8^{o}C and occurred at 14:00, which decreased to approximately 21.9^{o}C at 0.5 m away from the southern edge. The maximum surface temperature at the northern edge was 28.34^{o}C and occurred at 20:00.

At 06:00, Figure 5.19 shows that the temperature increased from about 19.1^{o}C at the southern edge to about 21.9^{o}C at 0.5 m from the southern edge, while the surface temperature decreased from about 24.9^{o}C to about 22.3^{o}C at 0.5 m from the northern edge.

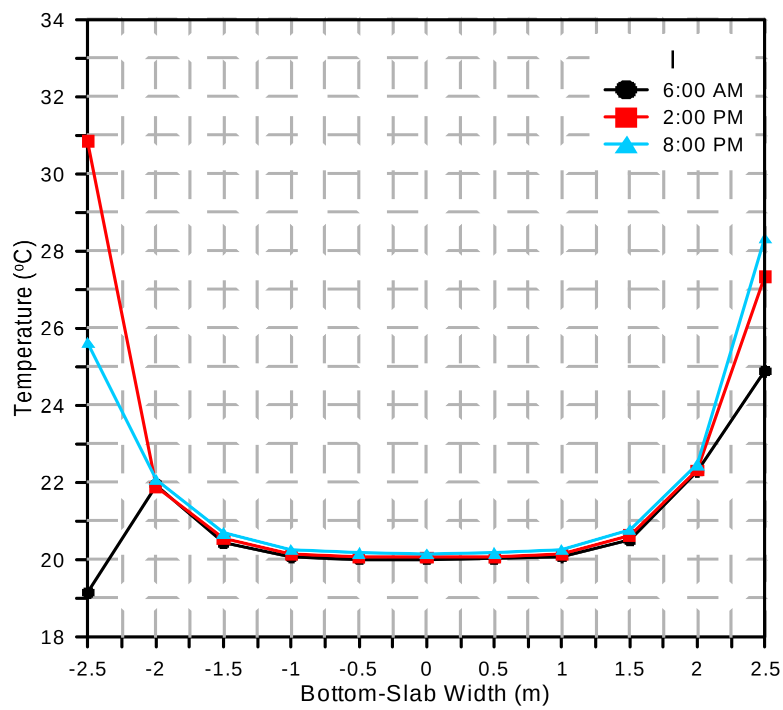

Figure 5.19 Transverse temperature distributions along the centerline of the 5 m width of the bottom slab at three time steps

Figure 5.20 demonstrates the transverse temperature distributions across the South wall thickness at the three time steps 06:00, 14:00 and 20:00. As shown in the Figure, the external surface temperature was lower than those in the interior surfaces at 06:00 by approximately 5^{o}C, while it was greater than those in the internal surface at 14:00 by approximately 6^{o}C.

At 08:00, Figure 5.20 shows that the maximum temperature was 25.65^{o}C and occurred at 0.1 m away from the external surface, which decreased to approximately 23.6^{o}C in the internal surface.

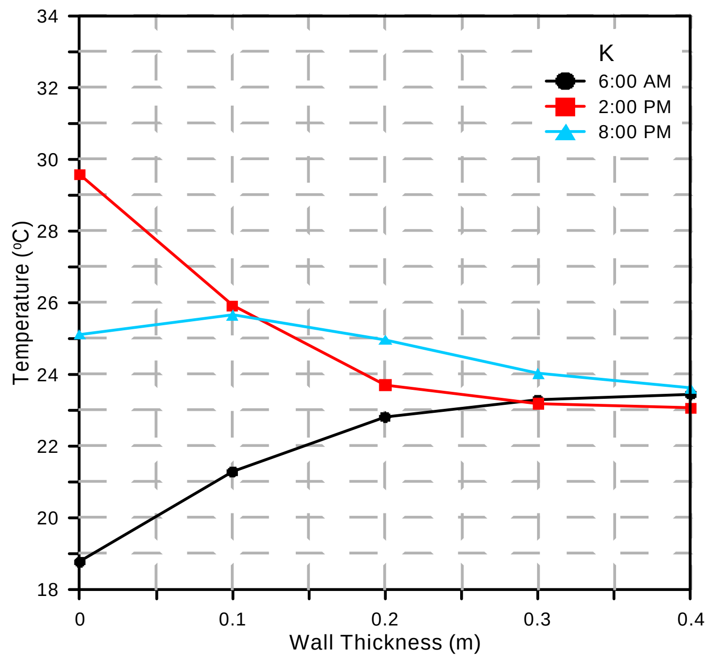

Figure 5.20 Transverse temperature distributions across the south web thickness at three time steps

Figure 5.21 shows the transverse temperature distributions across the north wall thickness at different time steps 06:00, 14:00 and 20:00. The Figure shows that the exterior surface temperature was larger than those in the interior surface at 14:00 by approximately 3^{o}C, while the maximum difference between the exterior surface temperature and interior surface temperature at 20:00 was 2.6^{o}C. As shown in Figure that the maximum temperature was approximately 28.74^{o}C, which occurred at 0.2 m away from exterior surface at 20:00.

At 06:00, Figure 5.21 shows that the minimum temperature was 24.3^{o}C and occurred at 0.1 m away from the external surface, which increased to approximately 25^{o}C in the internal surface, while the exterior surface temperature was approximately 25^{o}C at 06:00.

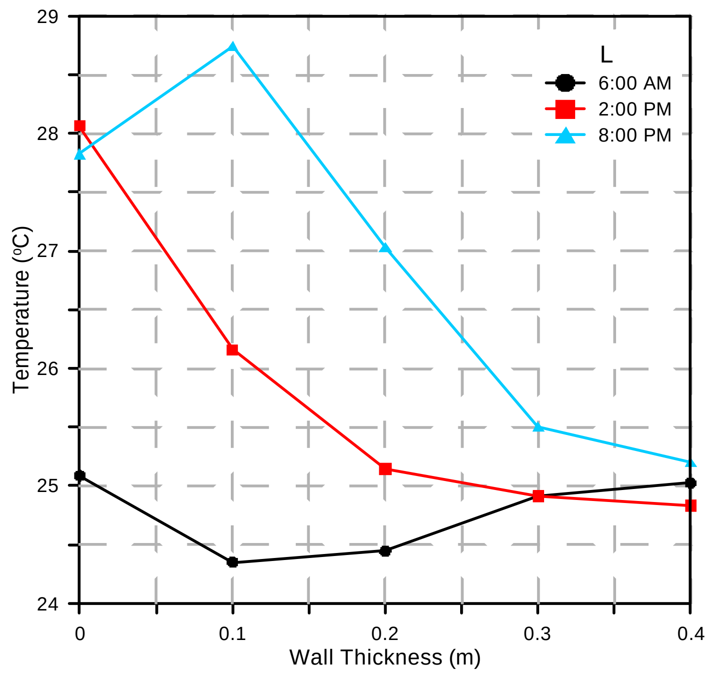

Figure 5.21 Transverse temperature distributions across the north web thickness at different time steps

Figures 5.22 to 5.24 show the 3D temperature distributions in the 3D FE box-girder model at the time steps 06:00, 14:00 and 20:00.

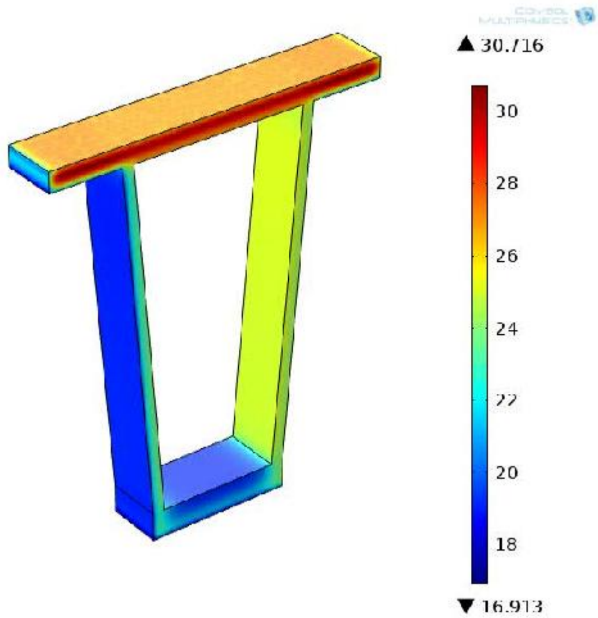

(A)

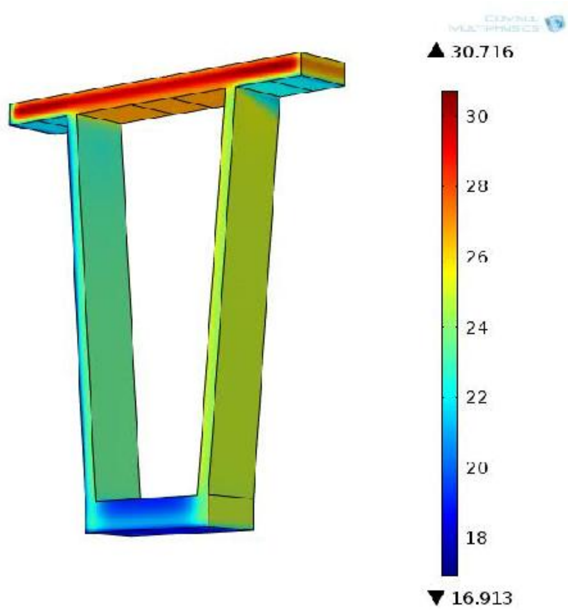

(B)

Figure 5.22 3D temperature distributions at 06:00: (A) northern face and (B) southern face

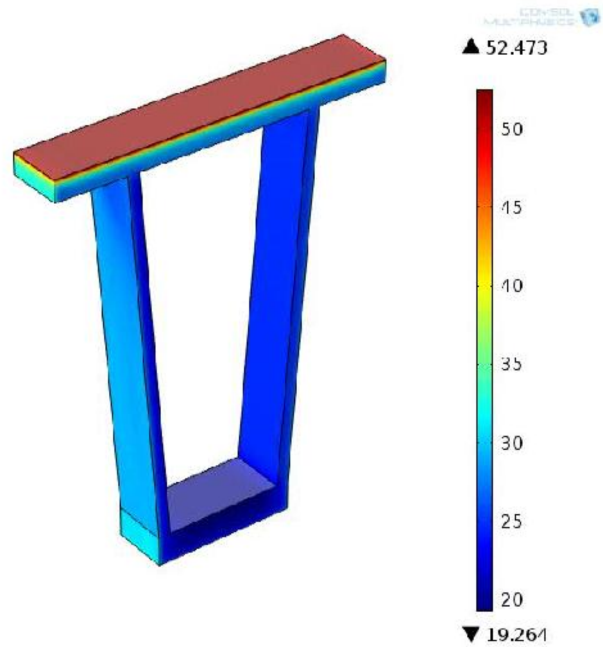

(A)

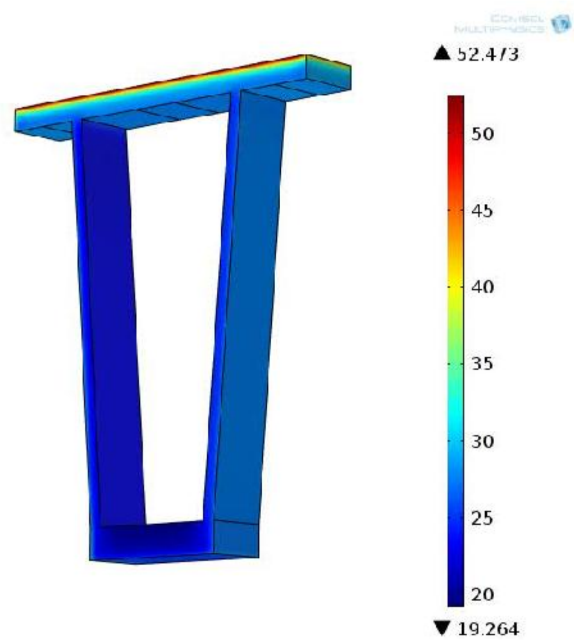

(B)

Figure 5.23 3D temperature distributions at 14:00: (A) northern face and (B) southern face

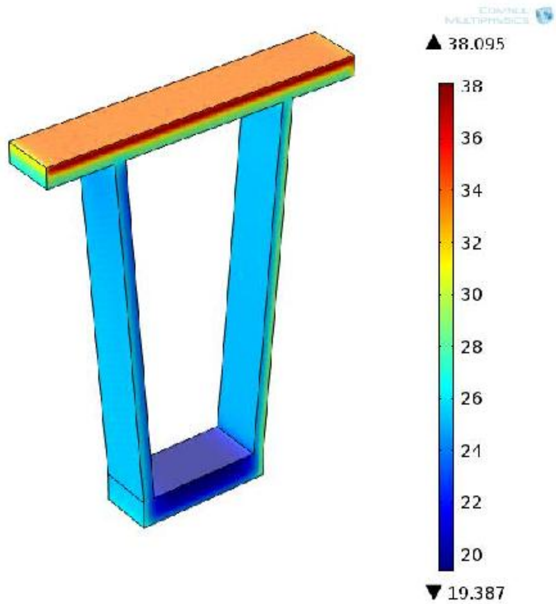

(A)

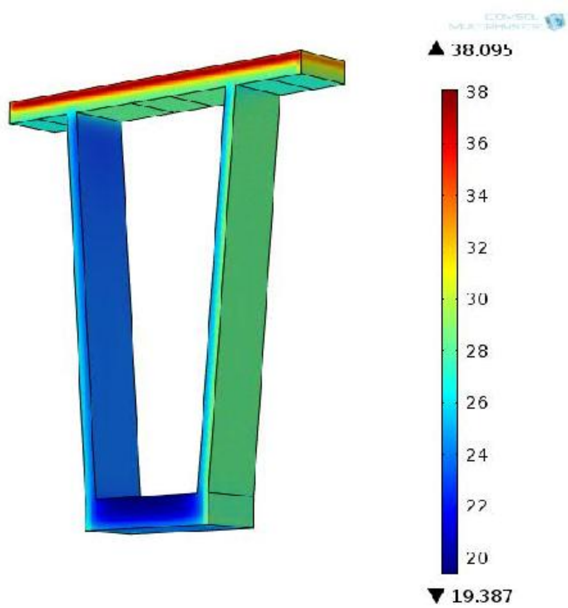

(B)

Figure 5.24 3D temperature distributions at 20:00: (A) northern face and (B) southern face

5.4 Maximum Positive and Negative Temperature Gradients

Figure 5.25 includes the distribution of positive vertical temperature gradients that were calculated by subtracting the lowest temperature from all other temperatures across the bottom slab. The Figure shows that the vertical temperature gradient was at the maximum value in the bottom surface of the bottom slab, which amounted to about 6.4°C at 15:00. The vertical temperature gradient decreased from the maximum value at the bottom surface to the zero point of the gradient at the top surface at around 15.00 as shown in Figure 5.25. This is because of the weak thermal conductivity of concrete, where the incoming heat energy input cannot be moved quickly within the inner concrete layers of the girder cross-section.

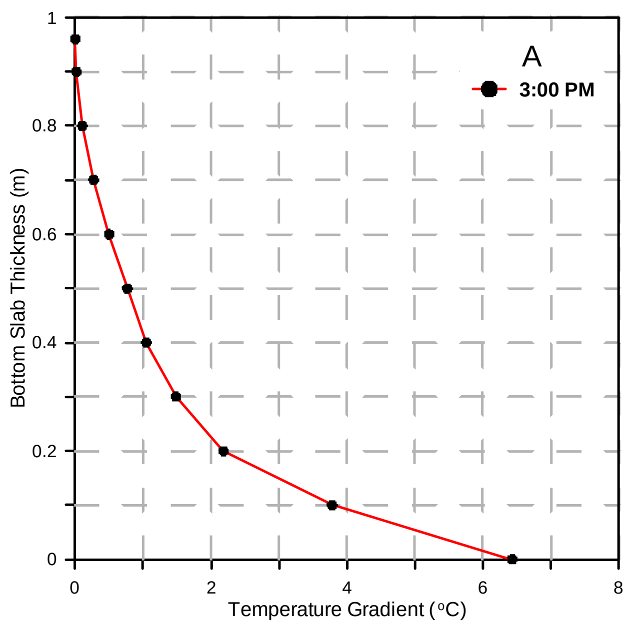

Figure 5.25 Vertical temperature gradients across the bottom slab of the FE model

Figure 5.26 shows the positive vertical temperature gradients across the top slab. As noted previously, the positive vertical temperature gradient mainly relies on the solar radiation intensity on the top horizontal surfaces of the bridge girders. The largest vertical temperature gradients occurred at the top surface, with a value of about 24.7°C at 13.40. The vertical temperature gradient decreased from the top surface to the zero point of the gradient at the bottom surface at about 13.40. as shown in Figure 5.26.

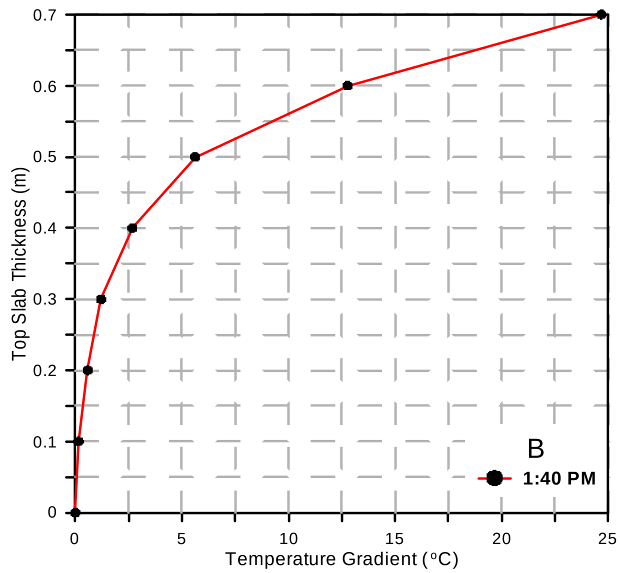

Figure 5.26 Vertical temperature gradients across the top slab of the FE model

Figures 5.27 to 5.28 show the positive and negative vertical temperature gradients along the 14 m depth of the South and North webs of the model section at different time steps. The largest negative gradients in the South web occurred at 0.3 m below the top surface of the top slab at 05:40, with a value of approximately 10.6°C, while the largest negative gradients in the North web occurred at 0.3 m below the top surface of the top slab at 05:20, with a value of approximately 10.8°C. The effect of the top slab thickness is clear in Figures 5.27 and 5.28, where the temperature gradients occurred across the top slab, while the temperature gradients were almost constant along the height of the webs. The top slab thickness is 0.7 m and the thermal conductivity coefficient of concrete is only 1.7 W/m K, therefore it is not enough to transfer the temperatures from the external surfaces to the internal surfaces during the daily thermal cycle.

It can be observed from Figures 5.27 to 5.28 that the largest negative gradients along the thickness of the bottom slab were approximately 3.7℃ at 05.40 in the South web and approximately 4.3℃ at 05:20 in the North web. The largest positive gradients along the South and North webs were about 29.56℃ at 13:20 and about 28.64℃ at 13:40, respectively, and occurred at the top surface of the top slab, whereas the positive temperature gradient at the bottom surface of the bottom slab in the South and North webs were approximately 3.4°C at 13.20 and approximately 2.9°C at 13:40, respectively.

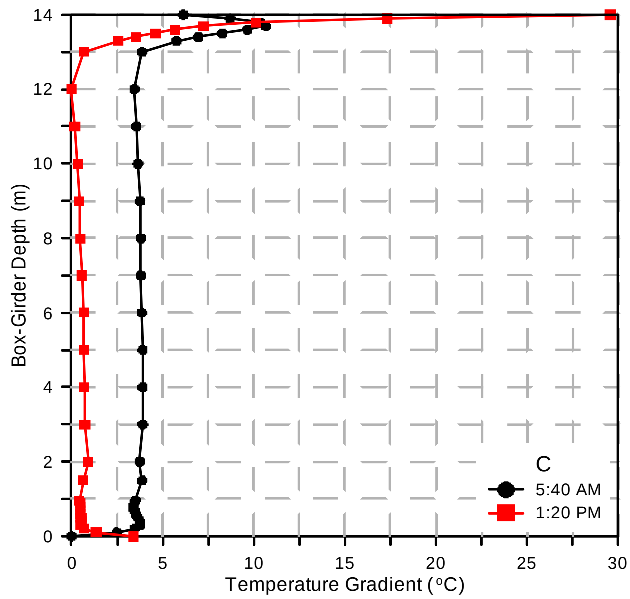

Figure 5.27 Vertical temperature gradients along the depth of the South web of the FE model

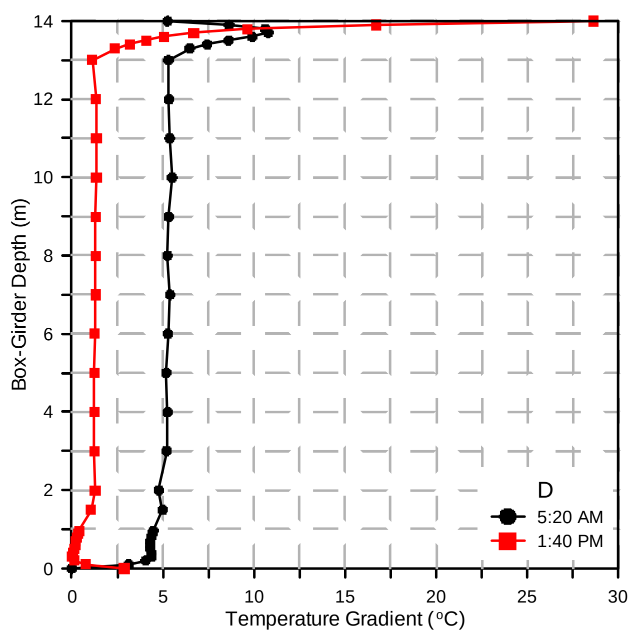

Figure 5.28 Vertical temperature gradients along the depth of the North web of the FE model

Figure 5.29 shows the positive and the negative transverse temperature gradients along the centerline of the 12 m width of the top slab at different time steps (05:40 and 13:20). From the Figure it can be seen that the positive and the negative surface temperature gradients at the northern and the southern faces were more varied compared with those along the central width of the top slab, where the positive and the negative temperature gradients were almost constant along the central width of the top flange. As stated earlier, the northern faces expose to the direct solar radiation for a few hours during the early morning and the last hours before the sunset, while the southern faces expose to the direct solar radiation from 09:00 to 15:00. Therefore, the positive and the negative surface temperature gradients at the southern edge were more than those in the northern edge. The largest positive and negative surface gradients at the southern edge were 4.7°C at 13:20 and 8.7°C at 05:40 respectively, while they were 0.23°C at 13:20 and 2.8°C at 05:40, respectively, at the northern edge.

As shown in Figure 5.29, the largest difference in the negative temperature gradient between the interior point at 0.5 m away from the southern edge and the southern edge was 8.55°C, while the largest difference in the negative temperature gradient between the interior point at 0.5 m away from the northern edge and the surface of the northern edge was 2.8°C. The positive temperature gradient decreased from the maximum value at the surface southern edge to a zero point of gradient at the interior point at 0.5 m away from the southern edge at around 13.20 as shown in Figure 5.29.

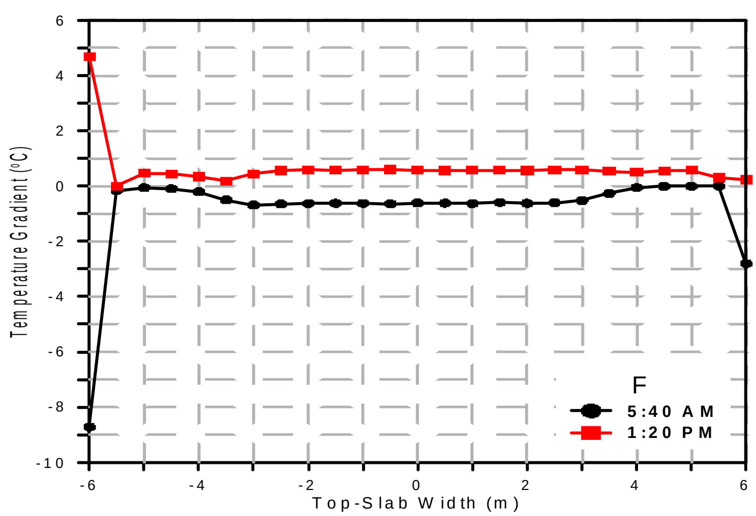

Figure 5.29 Transverse temperature gradients along the centerline of the width of the top slab of the FE model at different time steps

Figure 5.30 shows the positive and the negative transverse temperature gradients along the centerline of the 5 m width of the bottom slab at different time steps 05.40

and 13.40. It can be seen from the Figure that the positive and the negative surface temperature gradients at the northern and the southern edges were more varied compared with those along the central width, where the positive and the negative thermal gradients were almost constant along the central width of the bottom slab. The positive and the negative surface temperature gradients at the southern edge were more than those in the northern edge, where the largest positive and the negative surface gradients at the southern edge were 10.9^{o}C at 13.40 and 5.89^{o}C at 05.40 respectively, while they were 7.2^{o}C at 13.40 and zero at 05.40, respectively, at the northern edge.

As shown in the Figure, the largest difference in the positive temperature gradient between the interior point at 0.5 m away from the southern edge and the surface of the southern edge was 9^{o}C. The largest difference in the positive temperature gradient between the interior point at 0.5 m away from the northern edge and the surface of the northern edge was approximately 4.9^{o}C. From Figure 5.30 it can be seen that the largest difference in the negative temperature gradient between the interior point at 1.5 m away from the northern edge and the surface of the northern edge was approximately 4.9^{o}C.

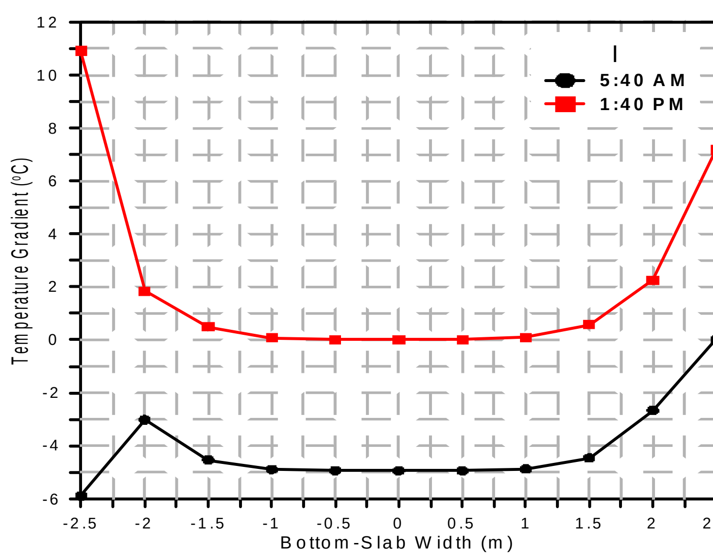

Figure 5.30 Transverse temperature gradients along the centerline of the width of the bottom slab of the FE model at different time steps

Figure 5.31 shows the positive and the negative transverse temperature gradients across the South wall thickness at different time steps (05.40 and 13.40). It can be seen, from the Figure that the maximum positive temperature gradient occurred at the exterior surface, which was approximately 6.7°C at 13:40 and the maximum negative temperature gradient occurred at the exterior surface, with a value of approximately 4.9°C at 05:40. The maximum positive and negative temperature gradients decreased to the zero value at the interior surface, as shown in Figure 5.31.

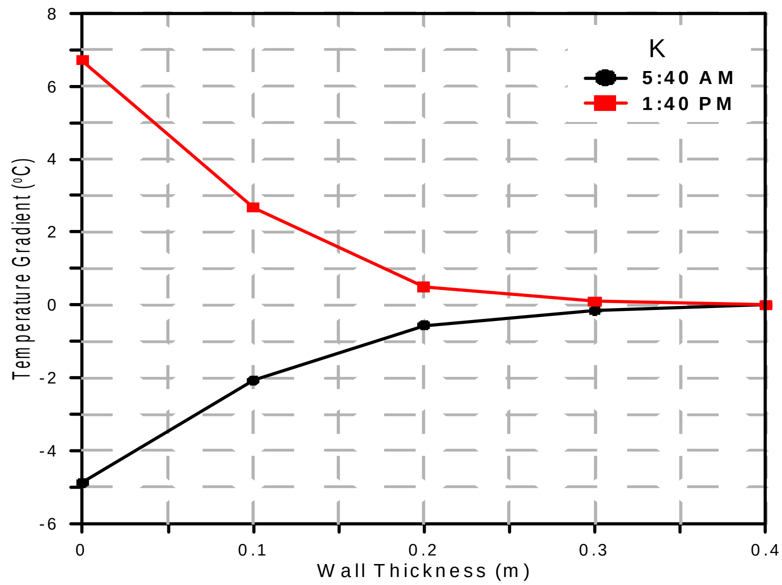

Figure 5.31 Transverse temperature gradients across the South wall thickness at different time steps

Figure 5.32 shows the positive and the negative transverse temperature gradients across the North wall thickness at different time steps (04.00 and 18.40). It is clear from the Figure that the maximum positive temperature gradient occurred at the exterior surface, which was approximately 11.2°C at 18:40 and the maximum negative temperature gradient occurred at the exterior surface, with a value of approximately 4°C at 04:00. The positive and the negative gradients at the interior surface were close to zero, as shown in Figure 5.32.

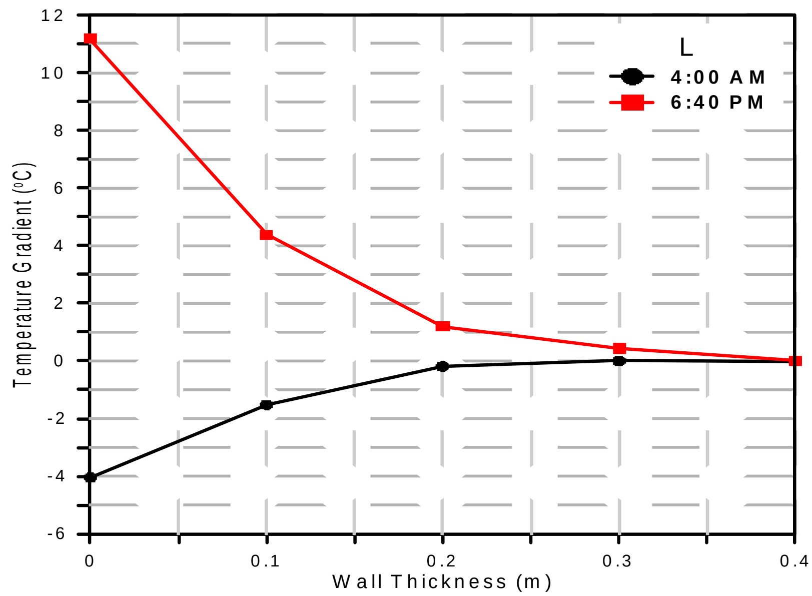

Figure 5.32 Transverse temperature gradients across the northern wall thickness at different time steps

.

CHAPTER 6

GEOMETRICAL PARAMETRIC STUDIES

6.1 General

The main objective of this chapter is study the effect of the cross-section geometry on the temperature distributions and the temperature gradients in deep concrete box girder bridges. The effect of other parameters such as the daily and seasonal range of the ambient air temperature, the location and orientation of the bridges, the incident solar radiation or the speed of the wind were studied by many scholars among them are Priestly and Buckle [58], Emerson [59], Elbadry and Gali [22, 23] and other. Therefore, the set of geometrical parameters were implemented, which concentrated on the impact of the variations of the geometrical properties on the thermal response. The analyzed geometrical parametric are the thickness of the top slab, the thickness of the bottom slab, the width of the cantilever wing and the depth of the girder. The summer climatic conditions on June 2nd have been utilized as the input weather data for the models, the detailed data of these climatic conditions are listed in chapter 5.

6.2 Thickness of the Top Slab

To study the effect of the top slab thickness on the thermal response of the box girder bridge, three cross sections of the FE model with three different thicknesses (Ts = 0.7m, Ts = 0.5m and Ts = 0.3m) were used. Aside from the top slab thickness, all dimensions remained the same as those in the original model, as shown in Figure 6.1.

Figure 6.1 shows the analyzed three cross sections of the model, where A is the model section with the top slab thickness of Ts = 0.7m, B is the model section with the top slab thickness of TS = 0.5m and C is the model section with the top slab thickness of Ts = 0.3m.

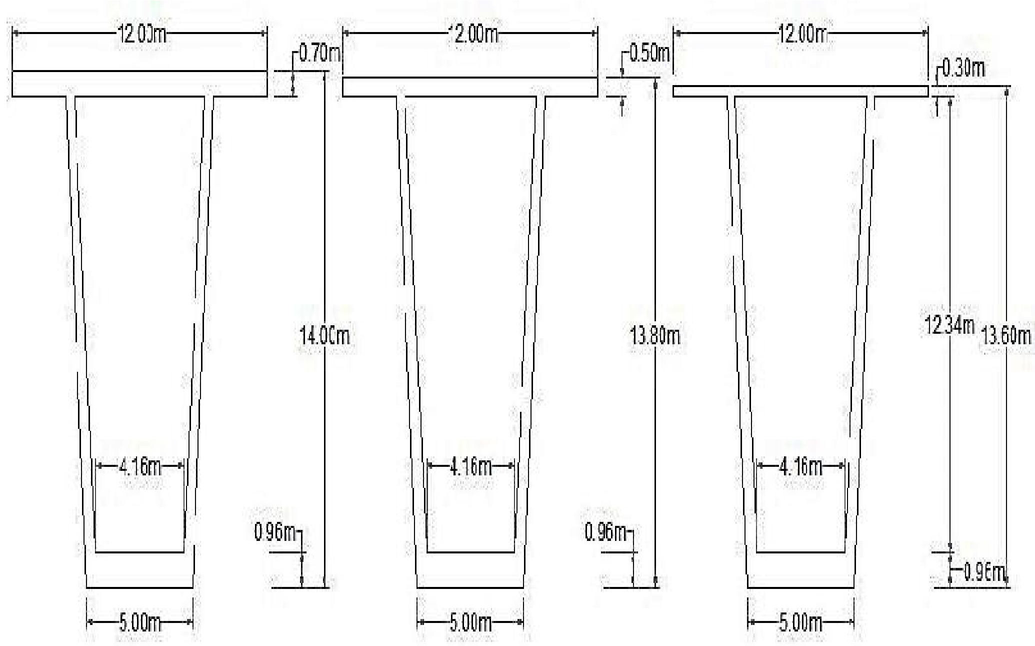

Figure 6.1 The analyzed cross sections in the parametric study of the upper slab thickness: (A) upper slab thickness = 0.7m (reference section), (B) upper slab thickness = 0.5m and (C) upper slab thickness = 0.3m.

Figure 6.2 shows the vertical temperature distribution across the top slab for the three cross sections of the model at 13:40. From the Figure, it is clear that the upper slab thickness has a significant effect on the vertical temperature distribution across the top slab. Actually, the top slab receives direct solar radiation especially through the top horizontal surface. When the top slab thickness is decreased, the ratio of the top surface area to the concrete volume of top slab becomes larger. Thus, the effective temperatures rise in the heating phase and drop in the cooling phase, this is due to the thermal properties of concrete.

From Figure 6.2, it can be observed that the maximum and the minimum temperature were 54.2^{o}C and 36.5^{o}C, respectively, which occurred at the top and the bottom surfaces of the thinner slab (Ts = 0.3m), while the maximum and minimum temperature that occurred at the top and the bottom surfaces of the thicker top slab (Ts = 0.7m) were approximately 52.4^{o}C and 27.7^{o}C, respectively.

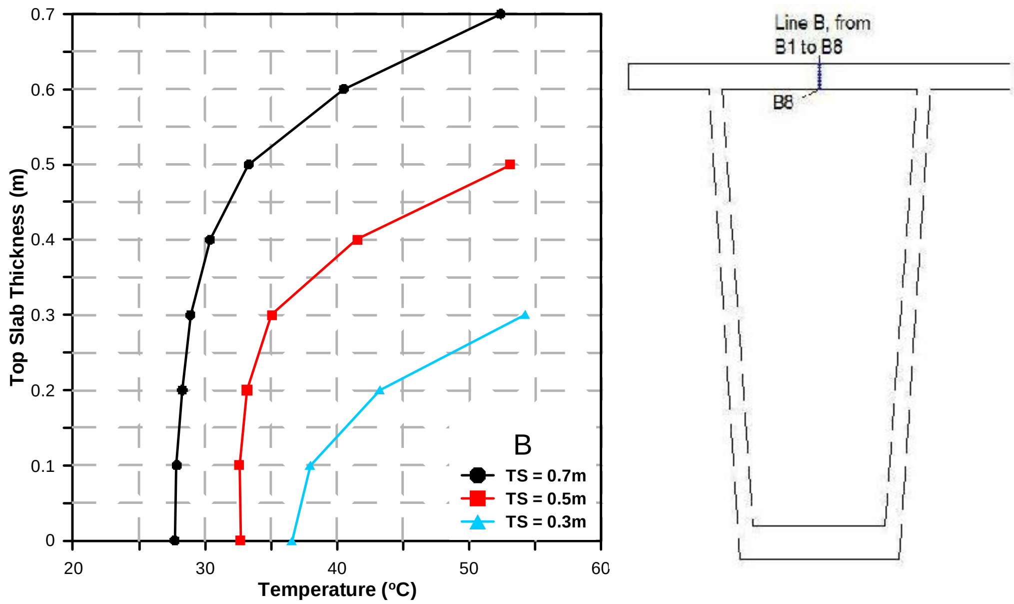

Figure 6.2 Vertical temperature distributions across the top slab for the three cross sections of the FE model at 13:40

Figure 6.3 shows the maximum values of the vertical temperature gradient across the top slab for the three cross-sections of the model at the specific time (at 13:40). From the Figure, it is clear that the top slab thickness has an important effect on the vertical temperature gradient across the top slab. Where a decrease in the top slab thickness from 0.7 m to 0.5 m led to a decrease in the vertical temperature gradient from 24.68°C to 20.52°C. As a result, the average gradient of temperature drop was about 0.2°C/1cm thickness (0.84%°C/1cm thickness) and then changed to approximately 0.14°C/1cm thickness (0.71%°C/1cm the thickness) when the top slab thickness reduced from 0.5 m to 0.3 m. As a result, the average gradient of temperature drop was approximately 0.17°C/ 1cm thickness (0.77%°C / 1cm thickness) for the top slab.

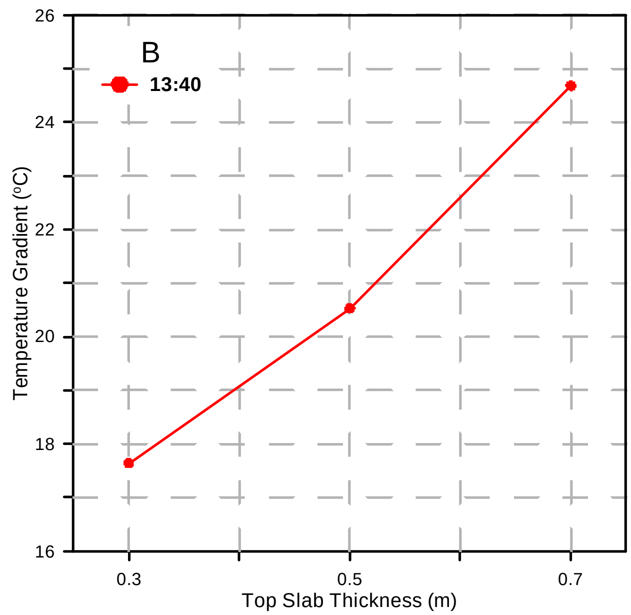

Figure 6.3 Temperature gradients across the top slab for the three cross section of the 3D FE model at 13:40

Figures 6.4 to 6.5 show the vertical temperature distributions along the depth of the south and the north webs at 13:20 for the three sections of the model. From these Figures, it can be observed that the effect of the top slab thickness on the vertical temperature distributions along the south and the north webs was negligible, where the vertical temperature distribution across the four walls of the three cross- sections of the model did not change significantly as a function of the thickness of the top slab.

The largest differences between the temperature distributions in the south and the north webs of the three cross sections occurred at the intersecting points of the girder webs and the top slab where the temperature of the thinner slab (Ts = 0.3 m) was greater than those of the thicker slab (Ts =0.7 m) by approximately 4.2^{o}C for each web.

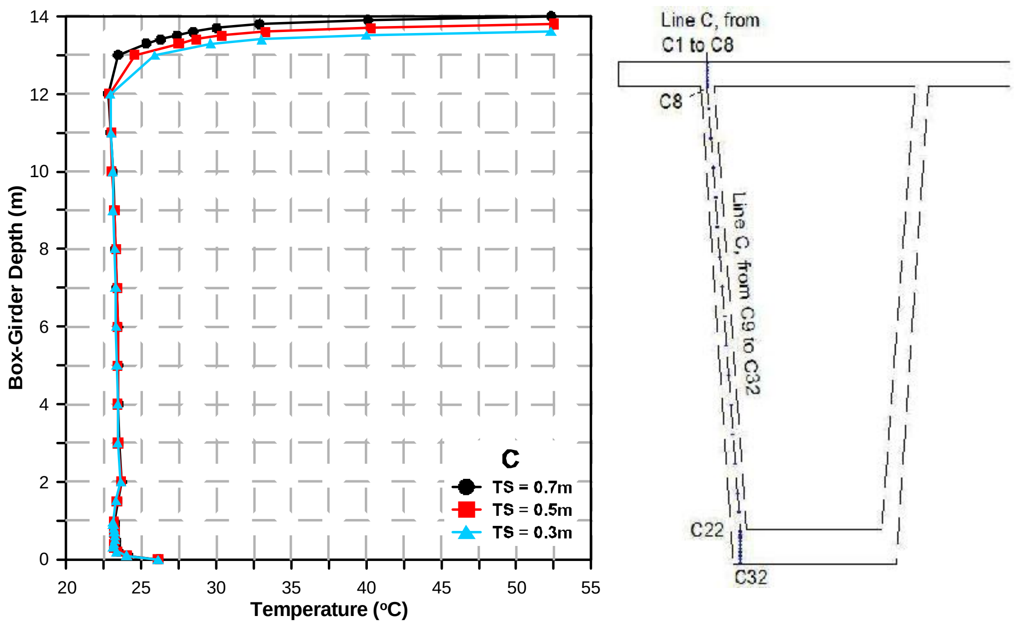

Figure 6.4 Vertical temperature distributions along the south web for the three cross sections of model at 13:20

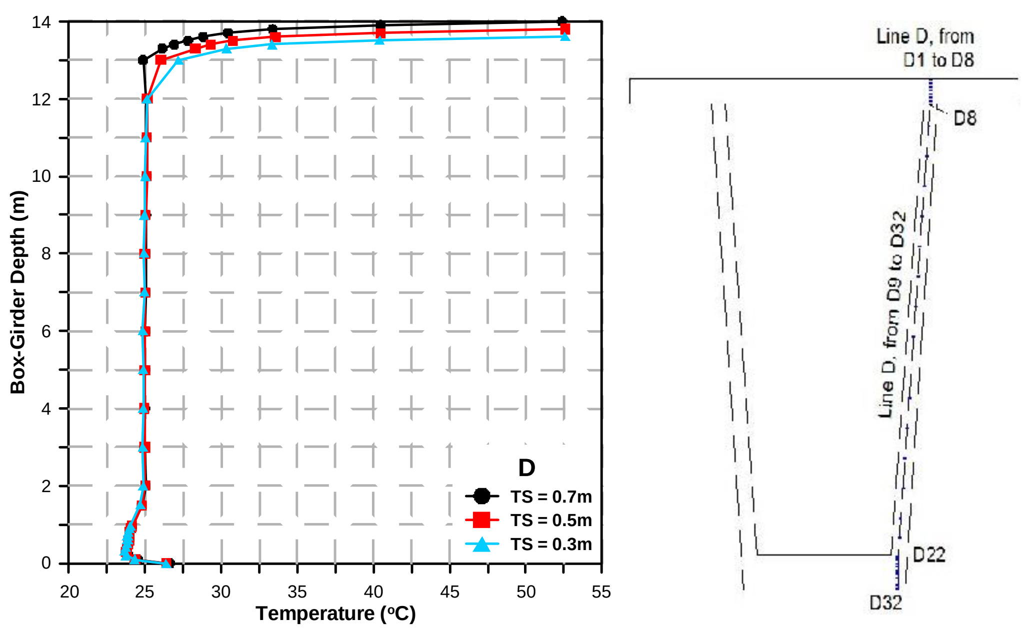

Figure 6.5 Vertical temperature distributions along the north web for the three cross sections of model at 13:20

Figures 6.6 to 6.7 show the maximum values of the vertical temperature gradient along the depth of the south and the north webs at about 13:20 for the three cross sections of the model. The effect of the top slab thickness on the vertical temperature gradients of the model sections was too small, where the maximum difference between the largest thermal gradients in the south and the north webs of the three cross-sections was found to be 0.3°C (0.05%°C/1cm thickness) for each web, as shown in Figures 6.6 and 6.7.

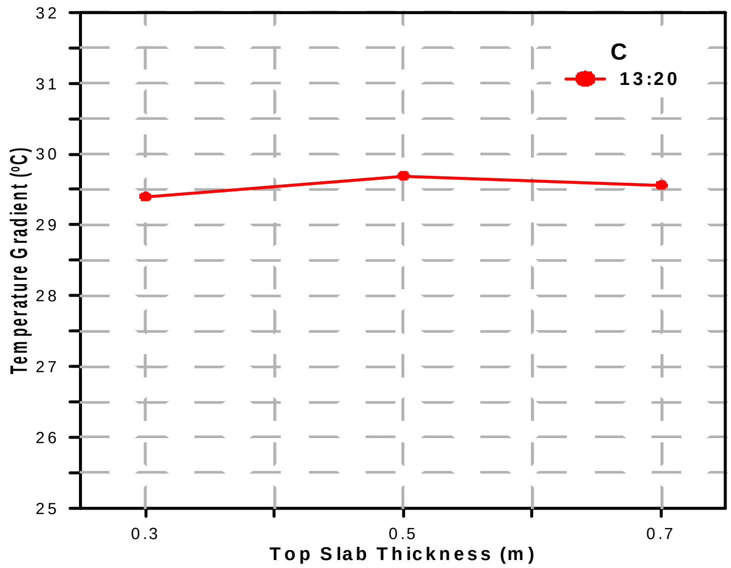

Figure 6.6 Maximum values of the vertical temperature gradient along the south web for the three cross sections of the model at 13:20

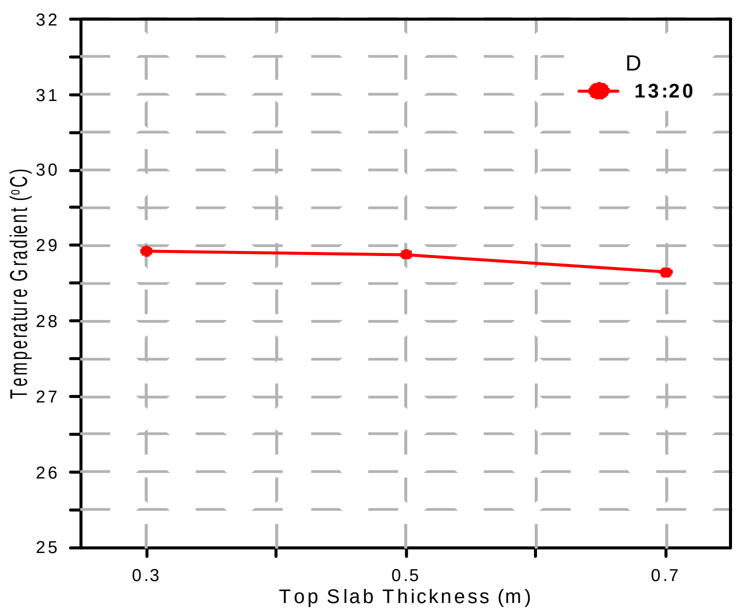

Figure 6.7 Maximum values of the vertical temperature gradient along the north web for the three cross sections of the model at 13:20

Figures 6.8 to 6.10 show the 3D temperature distributions for the three cross sections of the model at 13:40.

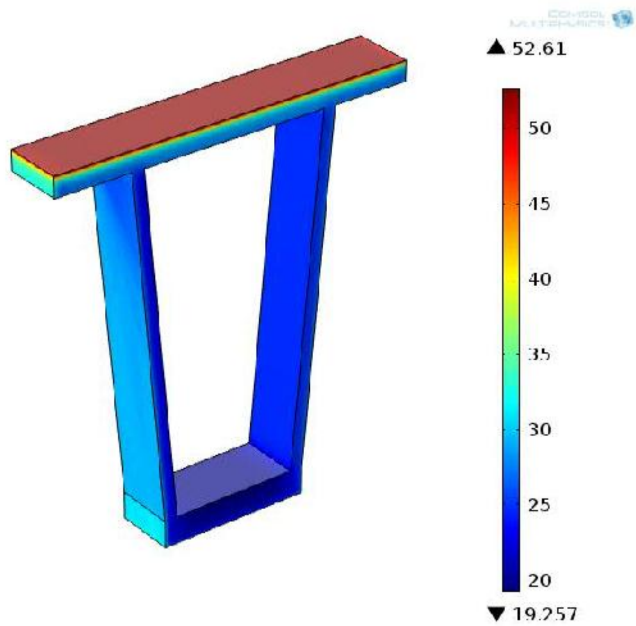

Figure 6.8 The 3D temperature distribution of the model section with top slab thickness of TS = 0.7 m at 13:40 (time of maximum gradient)

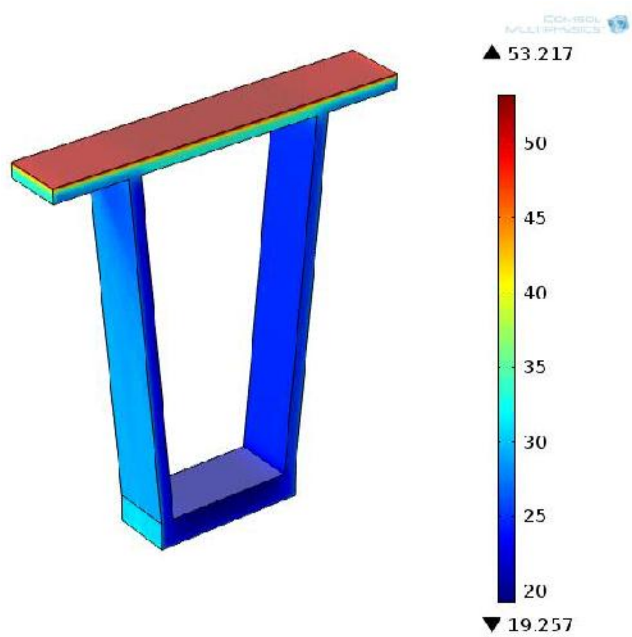

Figure 6.9 The 3D temperature distribution of the model section with top slab thickness of TS = 0.5 m at 13:40 (time of maximum gradient)

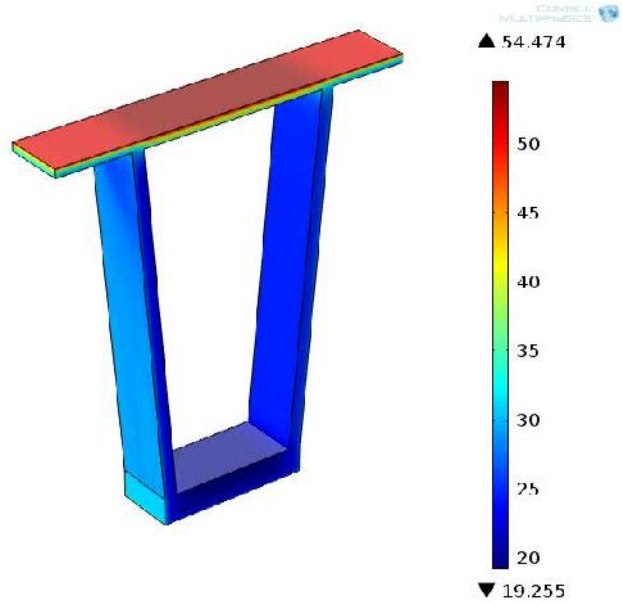

Figure 6.10 The 3D temperature distribution of the model section with top slab thickness of TS = 0.3 m at 13:40 (time of maximum gradient)

6.3 Thickness of the Bottom Slab

To study the effect of the bottom slab thickness on the thermal response of the box girder bridge, three cross sections of the FE model with variable thicknesses (Bs = 0.96 m, Bs = 0.7 m and Bs = 0.5 m) were used. Aside from the bottom slab thickness, all dimensions remained the same as those in the original model as shown in Figures 6.11.

Figure 6.11 shows the analyzed three cross sections of the FE model, where section (A) is the model section with the bottom slab thickness of Bs = 0.96 m, section (B) is the model section with the bottom slab thickness of Bs = 0.7 m and section (C) is the model section with the bottom slab thickness of Bs = 0.5 m.

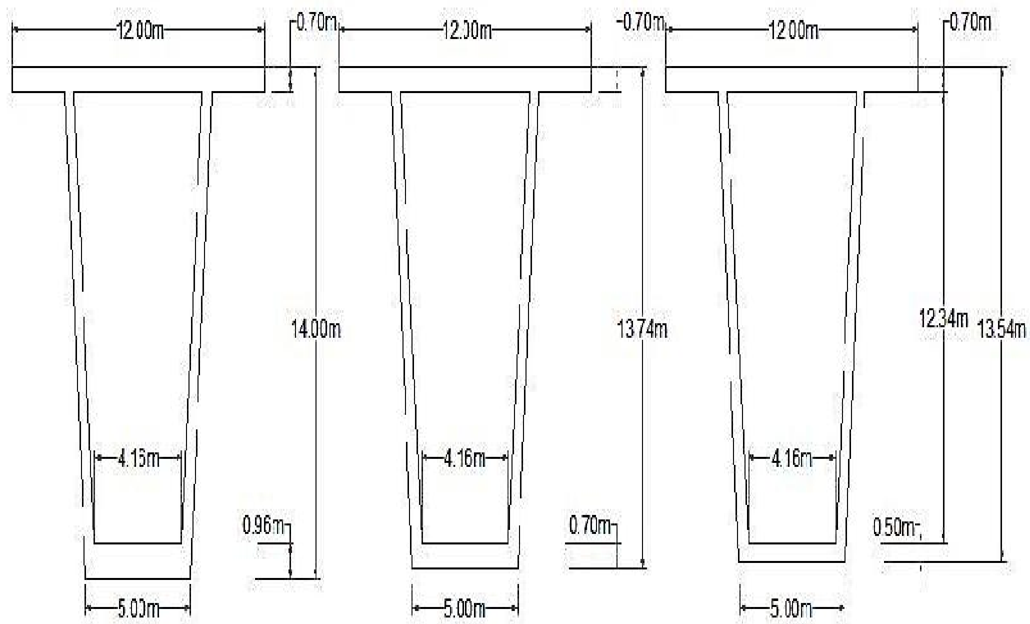

(A) (B) (C)

Figure 6.11 Analyzed cross sections in the parametric study of the bottom slab thickness: (A) bottom slab thickness = 0.96 m (reference section), (B) bottom slab thickness = 0.7 m and (C) bottom slab thickness = 0.5 m.

Figure 6.12 show the vertical temperature distributions across the bottom slab for the three cross-sections of the model at 15:00. From the Figure, it can be seen that the thickness of the bottom slab has a slight impact on the temperature distribution across the bottom slab at about 15.00. Where a decrease in the thickness of the bottom slab led to an increase in the temperature at the top surface and the internal layers of the bottom slab, while the increase in the temperature at the bottom surface was too small as shown in Figure 6.12. From the Figure the maximum temperature in the thinner slab of the model section (Bs = 0.5 m) was found to be 21.6^{o}C, while it was 19.3^{o}C in the thicker slab (Bs = 0.96 m).

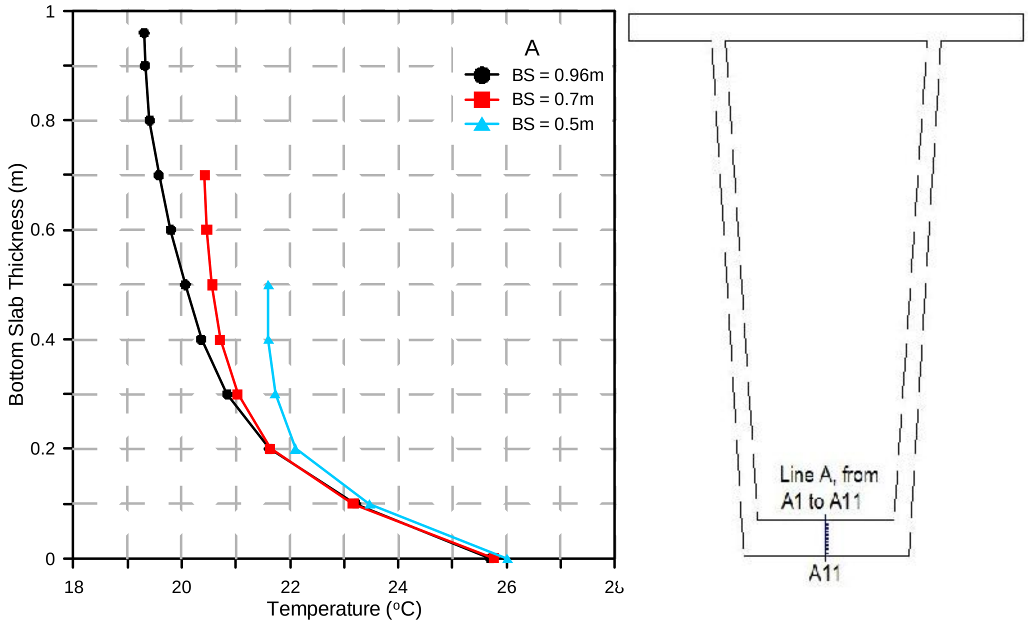

Figure 6.12 Vertical temperature distribution across the bottom slab for the three sections of the 3D FE model (Bs = 0.96 m, 0.7 m and 0.5 m)

Figure 6.13 show the maximum values of the vertical temperature gradient across the bottom slab for the three cross-sections of the model at 15:00. From the Figure, it is clear that the bottom slab thickness has a little effect on the vertical temperature gradient across the bottom slab. Where a decrease in the bottom slab thickness from 0.96 m to 0.7 m resulted in a decrease in the vertical thermal gradient from 6.39°C to 5.34°C, as a result, the average thermal gradient of temperature drop was about 0.05°C/1 cm thickness (0.82%°C/1cm thickness) and then changed to about 0.046°C/1cm thickness (0.86%°C/1cm thickness) when the bottom slab thickness reduced from 0.7 m to 0.5m. As a result, the average thermal gradient of temperature drop was about 0.048°C/1cm thickness (0.8%°C/1cm thickness) for the bottom slab. Thus, the effect of the bottom slab thickness on the thermal gradient is still within the negligible range.

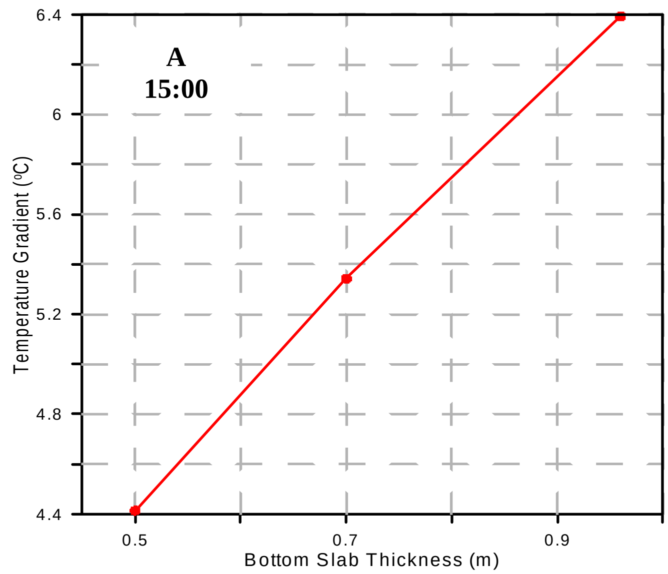

Figure 6.13 Maximum values of the vertical temperature gradient across the bottom slab for the three sections of the model at 14:30

Figures 6.14 to 6.16 show the 3D temperature distributions of the FE model with different thicknesses of the bottom slab at the time of maximum gradient (at 15:00).

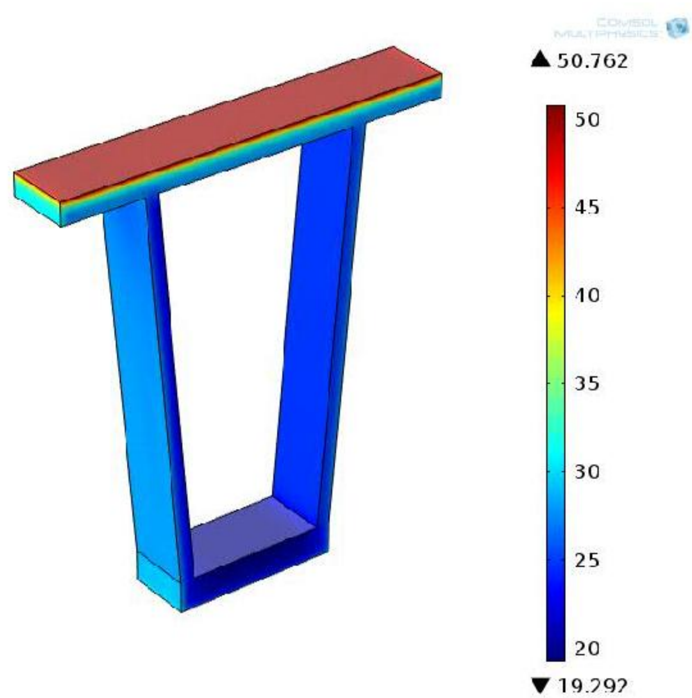

Figure 6.14 The 3D temperature distribution of the section with the bottom slab thickness BS = 0.96 m at 14:30 (time of maximum gradient)

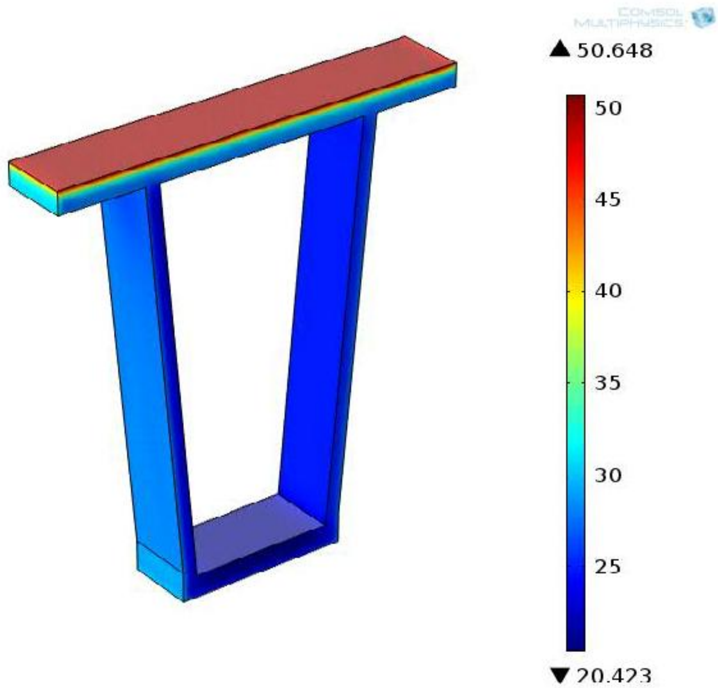

Figure 6.15 3D temperature distribution of the section with the bottom slab thickness BS = 0.7 m at 14:30 (Time of maximum gradient)

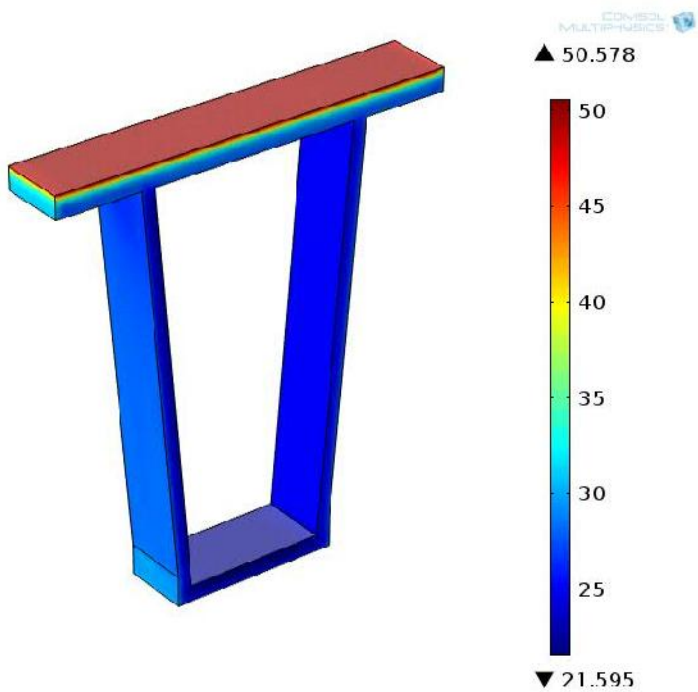

Figure 6.16 The 3D temperature distributions of the section with the bottom slab thickness BS = 0.7 m at 14:30 (Time of maximum gradient)

6.4 Width of the Cantilever Wing

The main purpose of this parametric study is to assess the impact of the overhanging width on the vertical and transverse temperature distribution and gradients in the concrete box-girder. To study the effect of the overhanging width on the variations in temperature over the cross section, three cross sections with the variable overhanging widths (W =4.5 m, W =2.5 m and W =0.5 m) were modeled. Apart from the overhanging width, all dimensions remained the same as those in the original model as shown in Figure 6.17.

Figure 6.17 shows the analyzed three cross sections of the FE model, where section (A) is the model section with the cantilever width (W = 4.5 m), section (B) is the model section with the cantilever width (W =2.5 m) and section(C) is the model section with the cantilever width (W = 0.5 m).

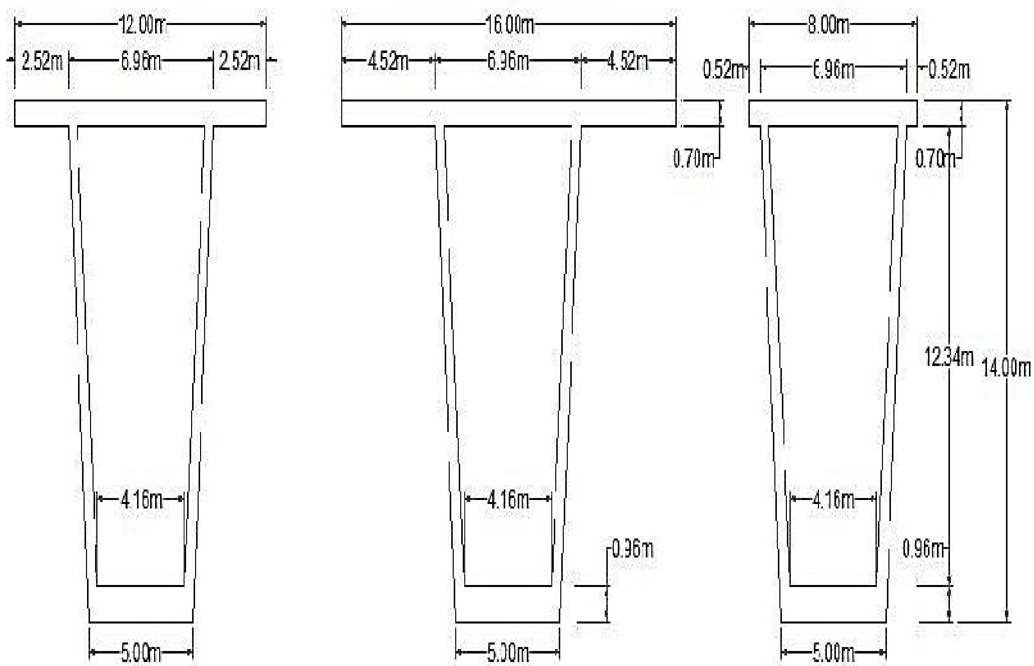

(A) (B) (C)

Figure 6.17 Analyzed cross sections in parametric study of the overhanging width: (A) overhanging width = 2.5 m (reference section), (B) overhanging width = 4.5 m and (C) overhanging width = 0.5 m.

Figures 6.18 to 6.19 show the vertical temperature distributions along the depth of the south and the north webs at13:20 for the three sections of the model. From the Figures, it is clear that the effect of the overhanging width on the vertical temperature distributions along the two webs is negligible, where the temperature was almost the same for the three overhanging widths. Although, the increase of the overhanging width of the top flange causes an increase in the shade length on the upper part of the surface area of the girder webs, but the effect on the temperature distribution is negligible. This is because the sun during the hot midday hours reaches high altitudes in the sky. Consequently, all the temperatures of the three cross sections were identical with each other's.

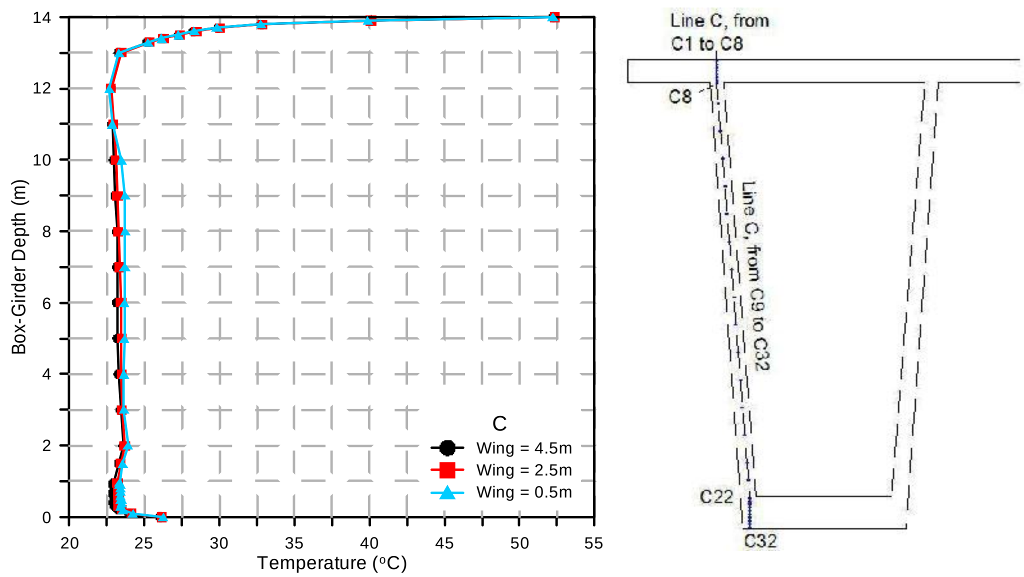

Figure 6.18 Vertical temperature distributions along the south web of the three sections of the FE model at 13:20

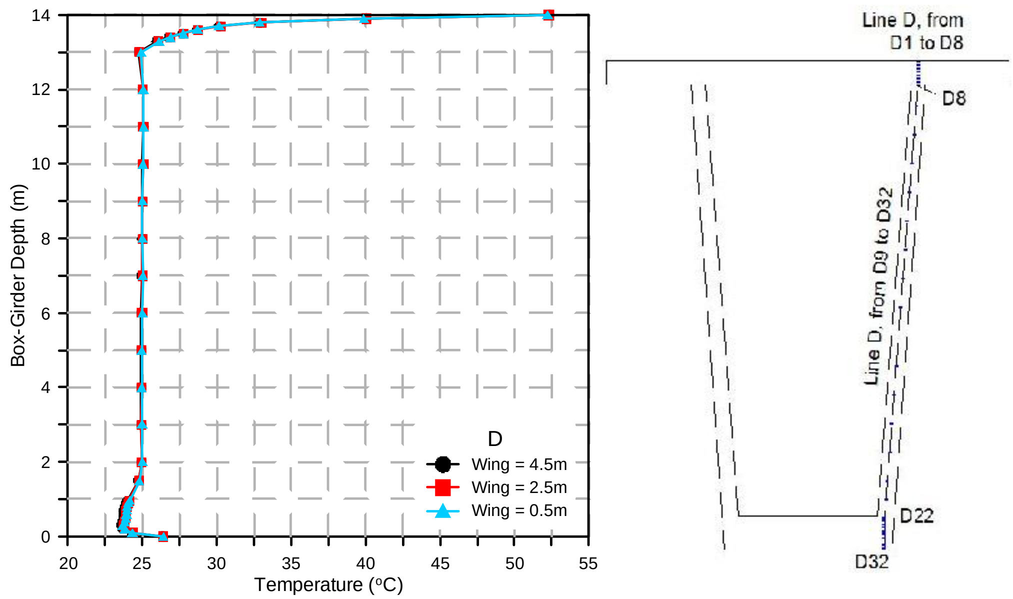

Figure 6.19 Vertical temperature distributions along the north web of the three sections of the FE model at 13:20

Figures 6.20 to 6.21 show the maximum values of the vertical temperature gradients along the depth for the three cross sections of the model at 13:20. From the Figures, it can be seen that the effect of the overhanging width of the top flange on the vertical temperature gradient is negligible. As shown in Figures 6.20 and 6.21 the largest thermal gradients in the south web of the three cross sections were 29.55°C for the section with the overhanging width of 4.5 m, 29.56°C for the overhanging width of 2.5 m and 29.57°C for the overhanging width of 0.5 m, while the largest thermal gradients in the north web of the three sections were 28.74°C for the overhanging width of 4.5 m, 28.61°C for the overhanging width of 2.5 m and 28.54°C for the overhanging width of 0.5.

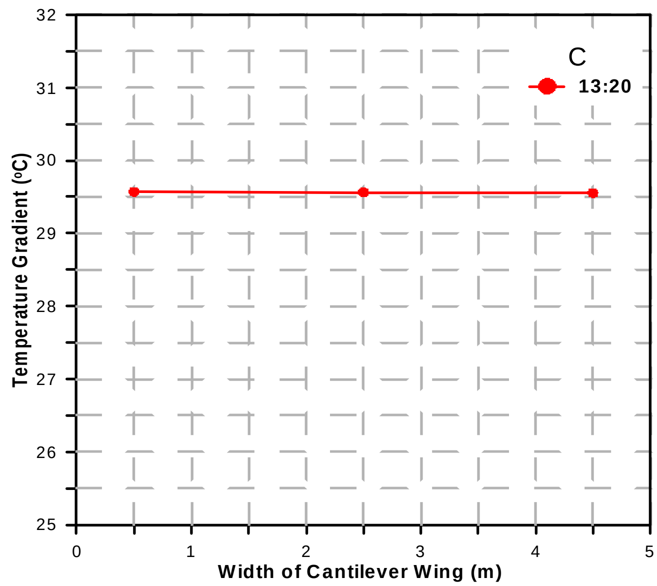

Figure 6.20 Maximum values of the vertical temperature gradient along the south web for the three sections of the model at 13:40

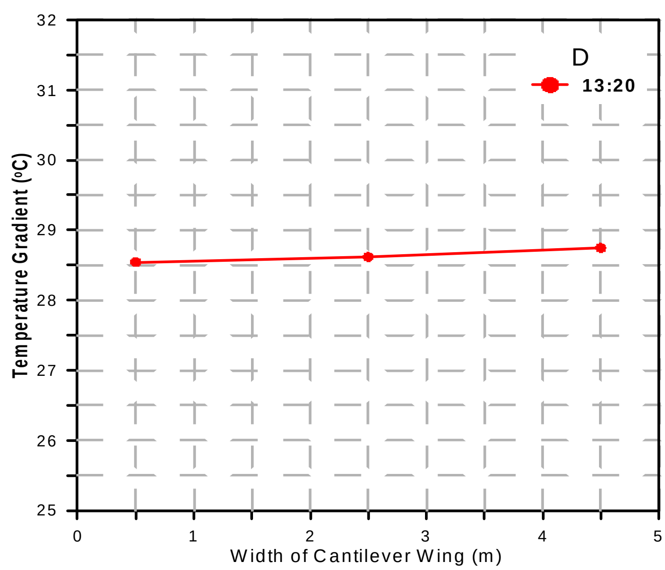

Figure 6.21 Maximum values of the vertical temperature gradient along the north web for the three sections of the model at 13:20

Figure 6.22 shows the transverse temperature distribution along the centerline of the upper slab thickness for the three cross sections of the model at 05:40. As shown in the Figure the effect of the overhanging width of the top flange on the transverse temperature distribution is negligible. This is because of the sun inclination angle in the early morning hours during the summer days. The northern faces are exposed to direct incident solar radiation with low altitude while the southern faces are almost entirely shaded.

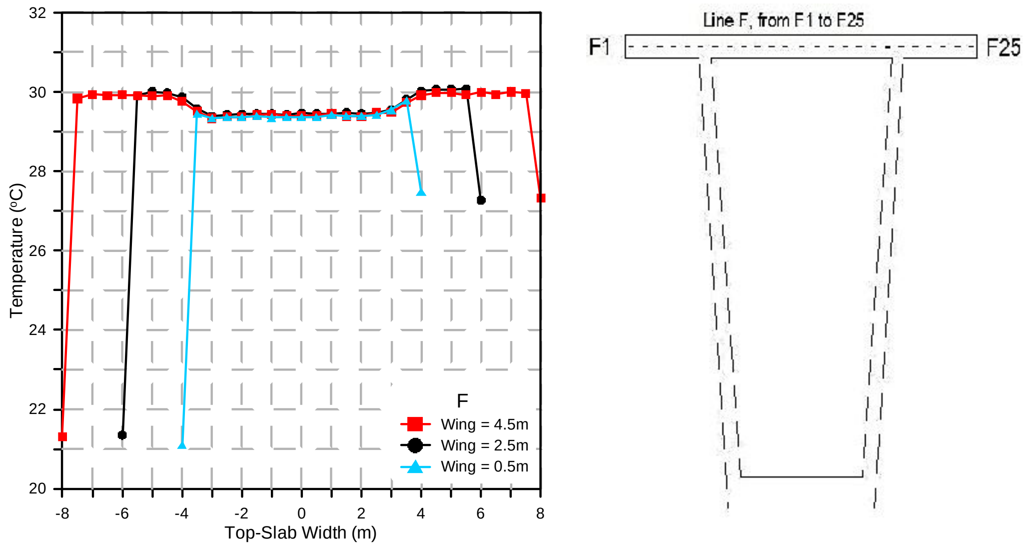

Figure 6.22 Transverse temperature distributions along the centerline of the top slab width of the three sections at 05:40

Figure 6.23 shows the maximum values of the transverse negative gradients along the centerline of the top slab thickness for the three cross sections of the model at 05:40. From the Figure, it is observed that the negative transverse thermal gradient was not affected by the changes made to the overhanging width of the top flange. As shown the in Figure, the largest negative gradients along the axis of the top slab thickness of the three cross sections of the model were 8.70^{o}C for the overhanging width 4.5 m, 8.72^{o}C for the overhanging width of 2.5 m and 8.66^{o}C for the overhanging width of 0.5 m.

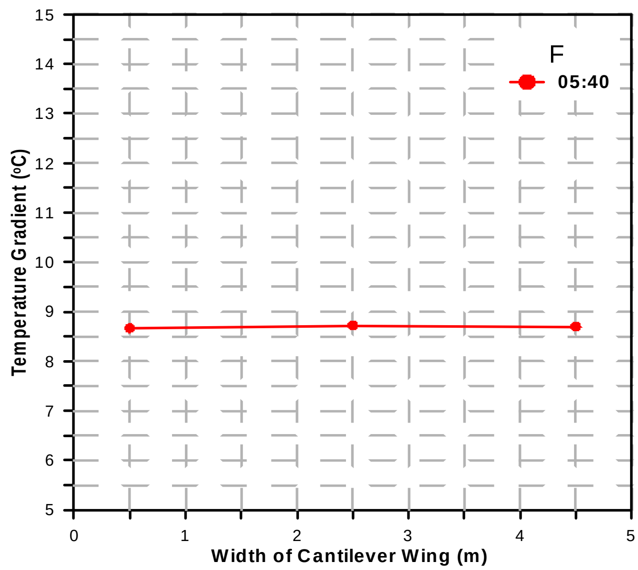

Figure 6.23 Maximum value of the transverse negative gradient along the centerline of the top slab thickness for the three cross sections of the FE model at 05:40

Figure 6.24 shows the transverse temperature distribution across the south web thickness of the three cross section of the model at 13:40. From the Figure it is clear that the overhanging width of the top flange has a slight effect on the transverse temperature distribution across the south web, where the decreasing the overhanging width resulted in a little increase in the transverse temperature distribution. As shown in Figure 6.24, the maximum temperatures occurred at the exterior surfaces for the three sections of the model were 30.38^{o}C for the overhanging width of 0.5 m, 29.77^{o}C for the overhanging width of 2.5 m and 29.57^{o}C for the overhanging width of 4.5 m, while the minimum temperatures occurred at the interior surfaces for the three sections of the model were 23.30^{o}C for the overhanging width of 0.5 m, 23.06^{o}C for the overhanging width of 2.5 m and 22.94^{o}C for the overhanging width of 4.5 m.

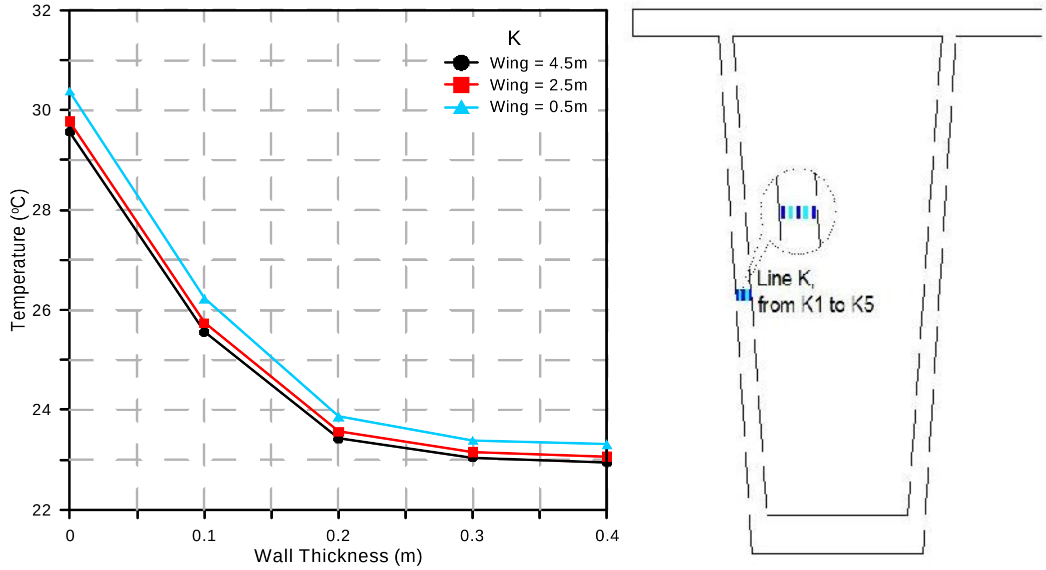

Figure 6.24 Transverse temperature distributions across the south web thickness of the three sections of the FE model at 13:40

Figure 6.25 shows the maximum values of the transverse temperature gradient across the south web thickness of the three cross sections of the model at 13:40. From the Figure, it can be observed that the cantilever wing width has a slight effect on the lateral temperature gradient across the south web. The decreasing the overhanging width from 2.5 m to 0.5 m resulted in an increase in the transverse thermal gradient from 6.7^{o}C to 7.07^{o}C, therefore, the average thermal gradient of temperature drop was about 0.18^{o}C/ 1m width (2.58%^{o}C/ 1m width), then changed to about 0.043^{o}C/1m width (0.63%^{o}C/1m width) when the cantilever width increased from 2.5 m to 4.5 m. As a result, the average thermal gradient of temperature drop was approximately 0.11^{o}C/ 1m width (1.60%^{o}C/1m width) for the overhanging width of the top flange. Hence, the effect of the overhanging width on the thermal gradient was within a minor range.

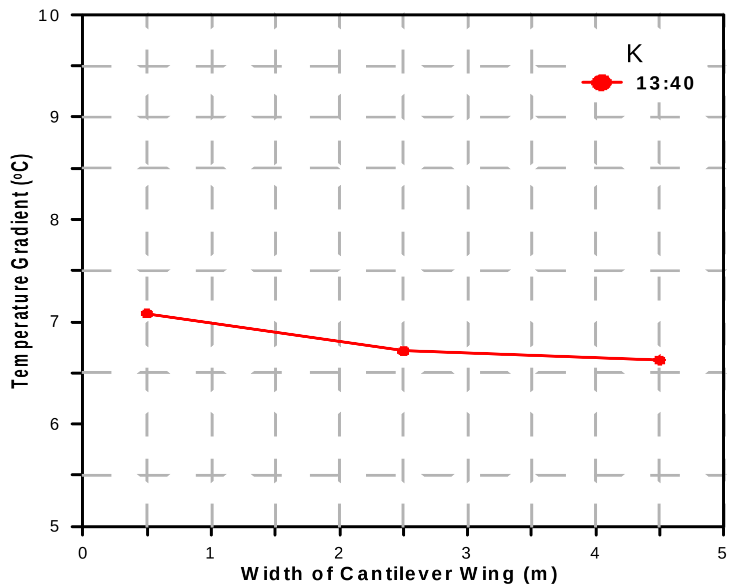

Figure 6.25 Maximum value of the transverse temperature gradient across the south web thickness for the three cross sections of the FE model at 13:40

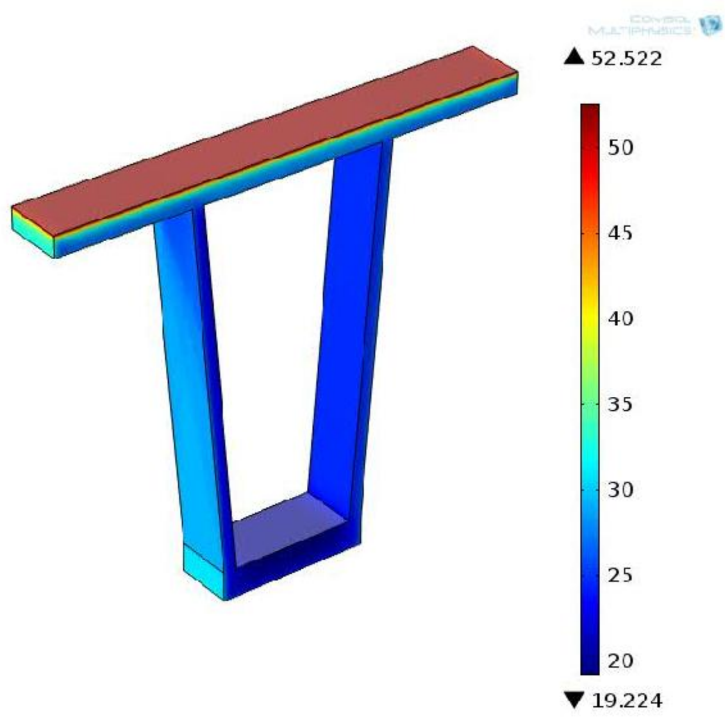

Figure 6.26 3D temperature distribution along the 14 m of depth of the model section with cantilever wings width = 4.5 m at 13:20 (time of maximum vertical gradient)

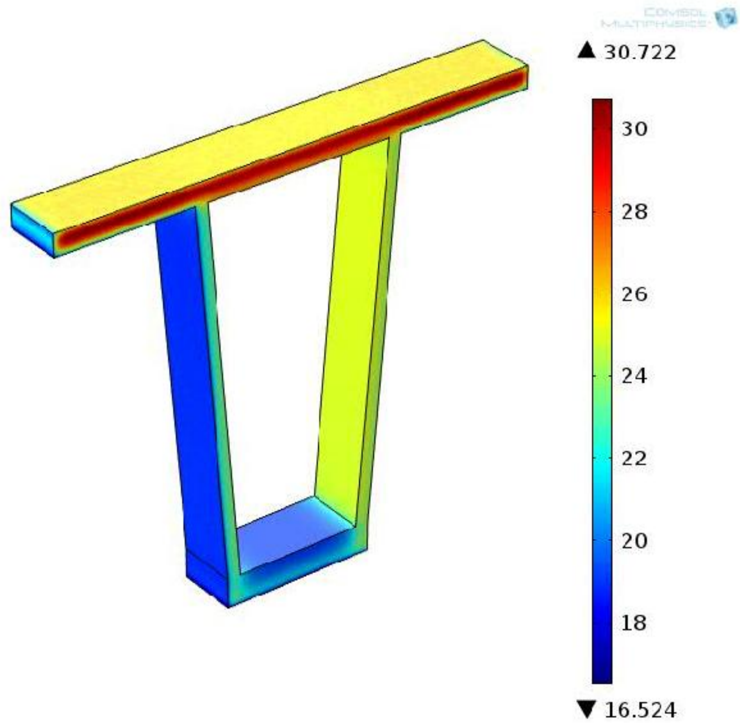

Figure 6.27 3D temperature distribution along the 14 m of depth of the model section with cantilever wings width = 4.5 m at 05:40 (time of maximum lateral negative gradient)

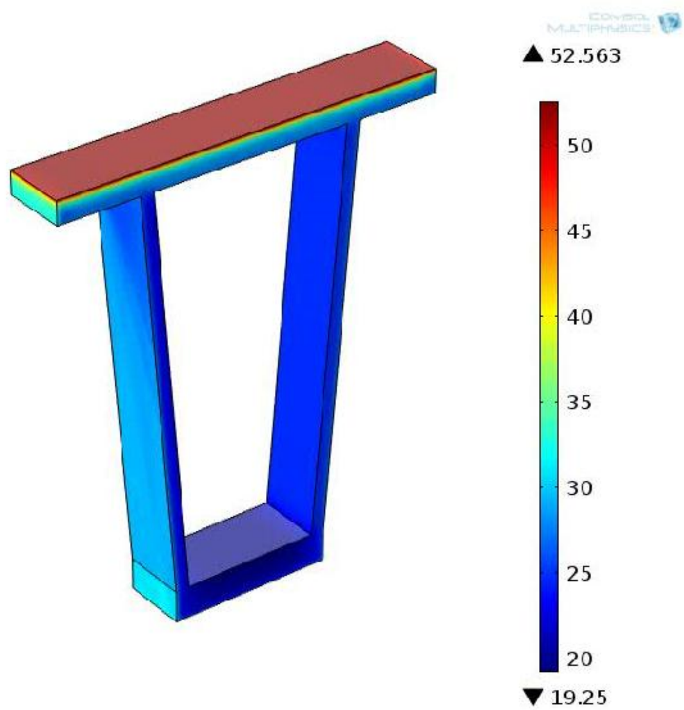

Figure 6.28 3D temperature distribution along the 14 m of depth of the model section with cantilever wings width = 2.5 m at 13:20 (time of maximum vertical gradient)

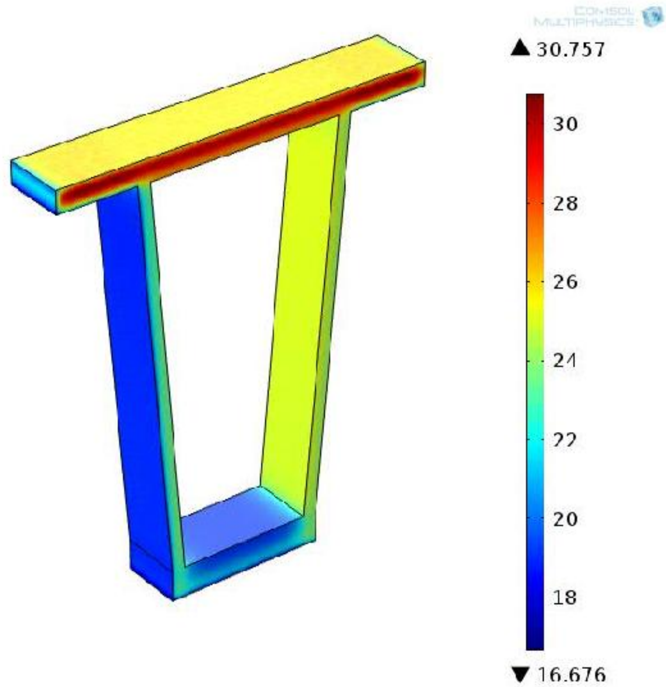

Figure 6.29 The 3D temperature distribution along the 14 m of depth of the FE model section with cantilever wings width = 2.5 m at 05:40 (time of maximum lateral negative gradient)

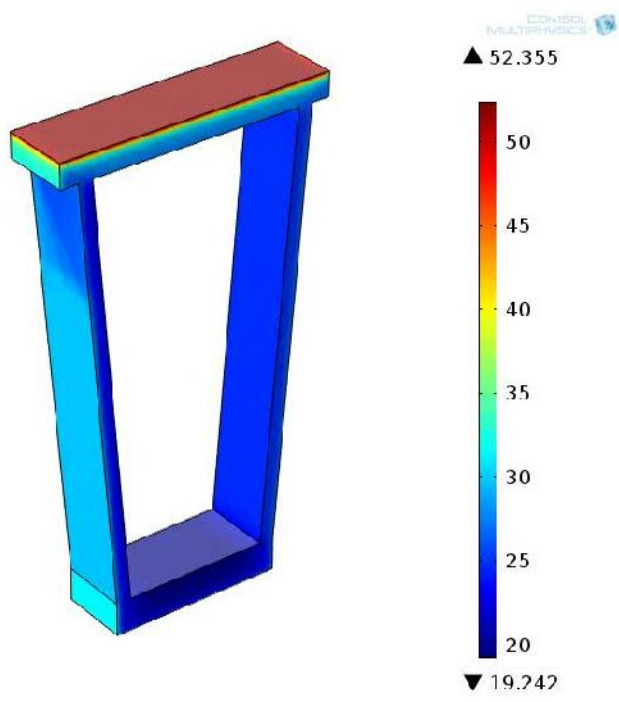

Figure 6.30 3D temperature distributions along the 14 m of depth of the FE model section with cantilever wings width = 0.5 m at 13:20 (time of maximum vertical gradient)

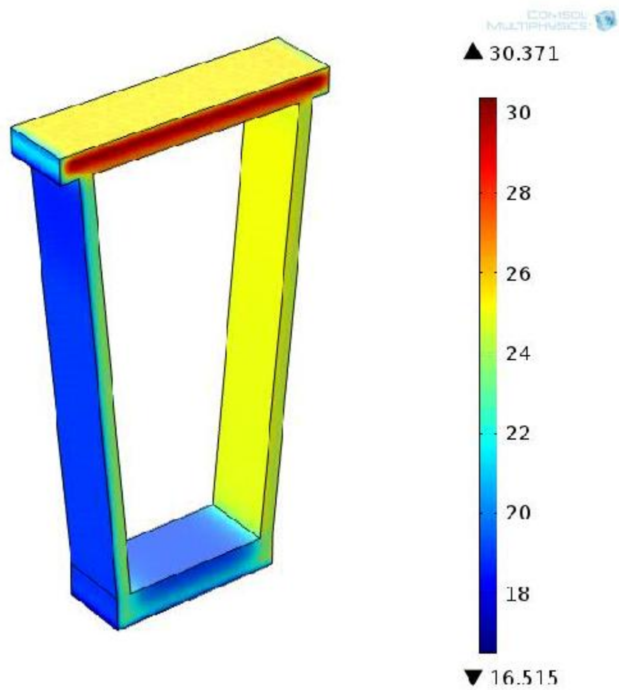

Figure 6.31 3D temperature distributions along the 14 m of depth of the model section with cantilever wings width = 0.5 m at 05:40 (time of maximum lateral negative gradient)

6.5 Depth of the Box-Girder

The height of the superstructure affects the surface area of the webs of the box girder. To study the effect of the girder depth on the variations in temperature over the cross section, three cross sections of the FE model with variable superstructure depths (D =14m, D =9m and D =4 m) were used. Apart from the girder depth, all dimensions remained the same as those of the original model, as shown in Figure 6.32.

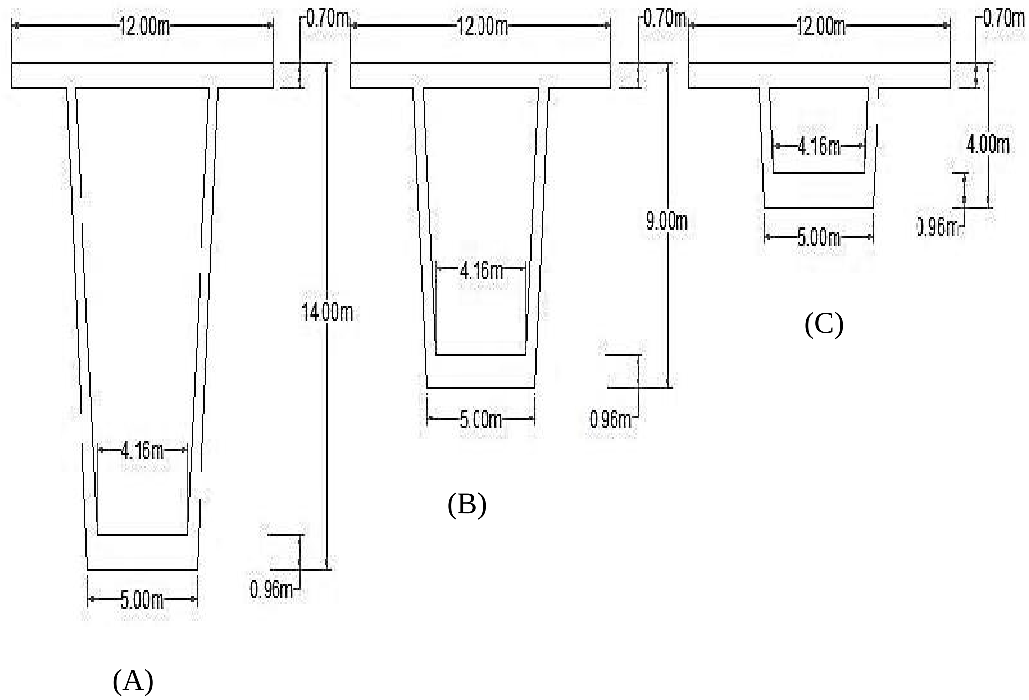

Figure 6.32 the analyzed cross sections in the parametric study of the girder depth: (A) girder depth = 14 m (reference section), (B) girder depth = 9m and (C) girder depth = 4 m

Figures 6.33 and 6.34 illustrate the vertical temperature distribution along the depth of the south and north web for the three cross sections of the model at 13:20. From Figure 6.33, it is clear that the influence of changing of the girder depth on the vertical temperature distribution in the south web was slight. As shown in Figure 6.34, the curves of the temperature distribution along the north web at 13:20 were very similar for the three different depths. Decreasing the girder depth resulted in an increase in the shadow length on the girder webs. However the variation in the temperature distribution was slight, this is because the girder webs are usually exposed to sunrays at sunrise or sunset, which are not quite intense, while during the noon hours, the girder webs are entirely shaded. As a result, the difference in the vertical temperature distributions was very little, as shown in Figures 6.33 and 6.34.

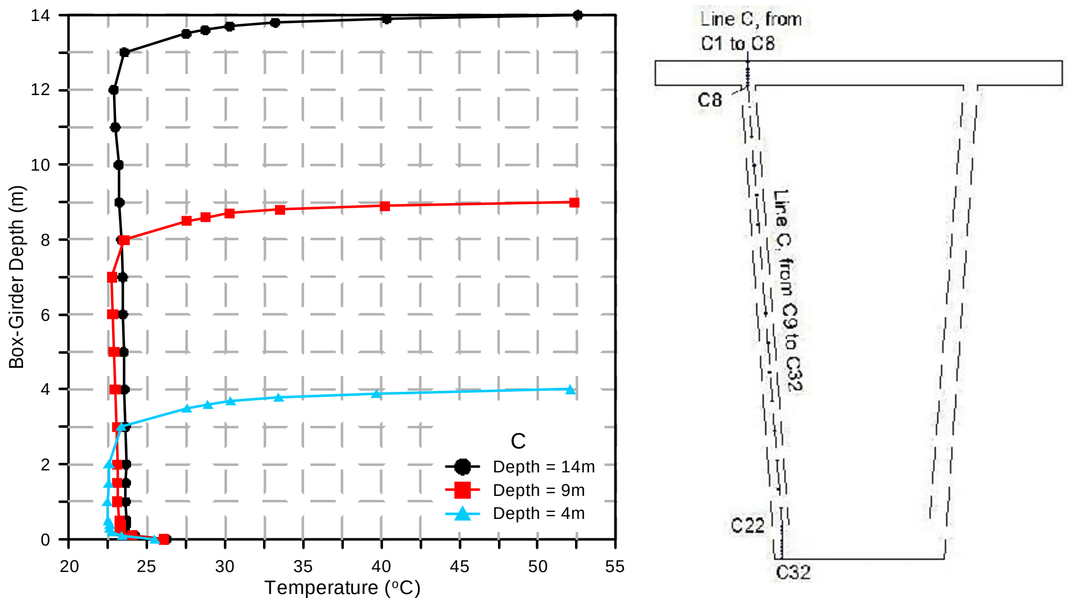

Figure 6.33 Vertical temperature distributions along the south web of the three girder depths at 13:20

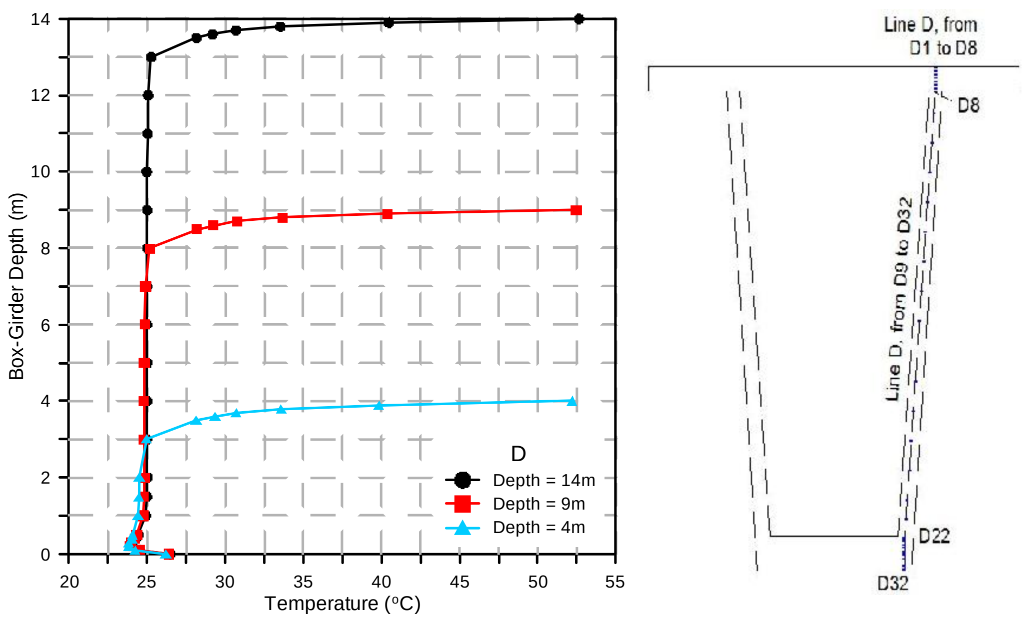

Figure 6.34 Vertical temperature distributions along the north web of the three girder depths at 13:20

Figures 6.35 to 6.36 show the maximum values of the vertical thermal gradient along the depth of the south and the north webs for the three cross sections of the model at 13:20. The representation of the vertical thermal gradient values explained the effect of the girder depth on the vertical thermal gradient of the model sections. As shown in the Figures, the maximum thermal gradients were not affected by the changes made to the girder depth.

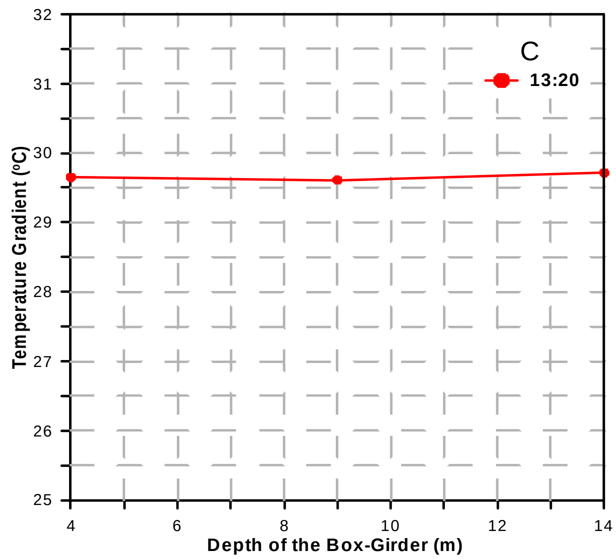

Figure 6.35 Maximum values of the vertical temperature gradient along the south web for the three girder depths at 13:20

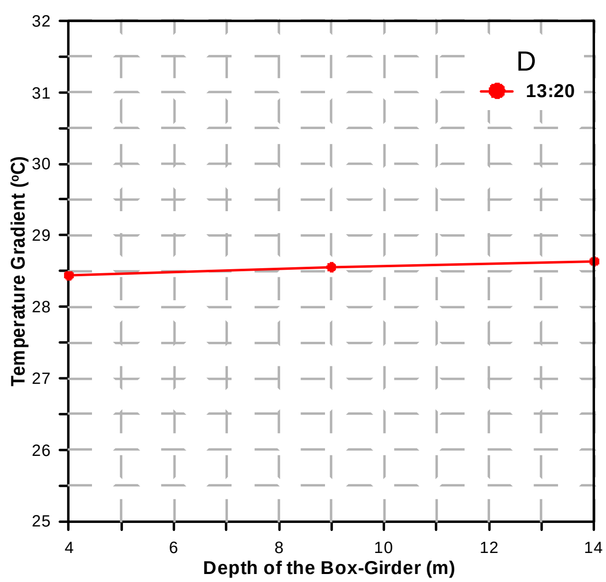

Figure 6.36 Maximum values of the vertical temperature gradient along the north web for the three girder depths at 13:20

Figure 6.37 illustrates the transverse temperature distributions along the centerline of the upper flange width for the three cross sections of the model at 05:40. As shown in the Figure, the effect of the girder depth on the transverse temperature distribution is negligible at 05:40. This is because of the sun inclination angle in the early morning hours during the summer days, where the sunrays strike the northern faces with low angles while the southern faces are entirely shaded at that time

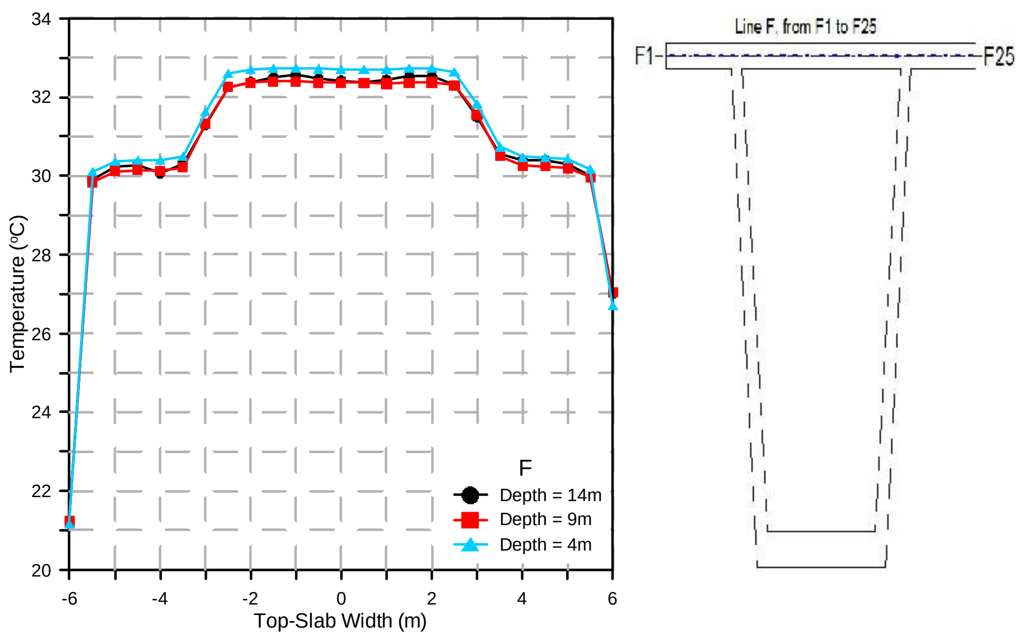

Figure 6.37 Transverse temperature distributions along the centerline of the top slab width for the three girder depths at 05:40

Figure 6.38 illustrates the maximum values of the negative transverse thermal gradient along the centerline of the top slab width for the three cross sections at 05:40. From the Figure it can be seen that the maximum thermal gradient of the shallow section was greater than those in the deep section by approximately 0.35^{o}C, while it was greater than those in the section of girder depth of 9 m by about 0.46^{o}C, as a result, the influence of the girder depth on the transverse thermal gradient was very little.

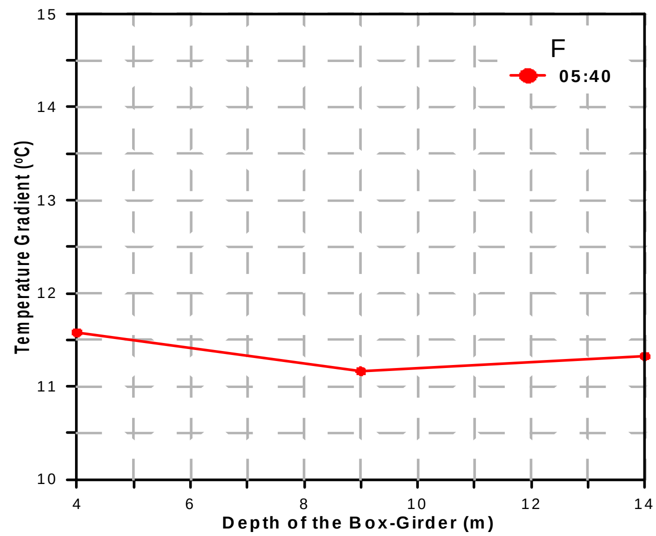

Figure 6.38 Maximum values of the transverse temperature gradient along the centerline of the top slab width of the three girder depths at 05:40

Figure 6.39 demonstrates the transverse temperature distribution across the south web thickness for the three cross sections of the model at 13:20. From the Figure, it is clear that the superstructure depth has a significant effect on the transverse temperature distribution across the thickness of the web. Increasing the girder depth resulted in lower shading length on the surface area of the girder webs, which led to the receiving of more from direct solar radiation and indirect solar radiation such as reflected radiation and increase in ambient air temperature. Therefore, the transverse temperature distribution was affected by changing the girder depth. The maximum surface temperature that occurred on the external surface of the deeper section was 29.3^{o}C, while the minimum surface temperature that occurred on the internal surface of the shallow section was 22.48^{o}C.

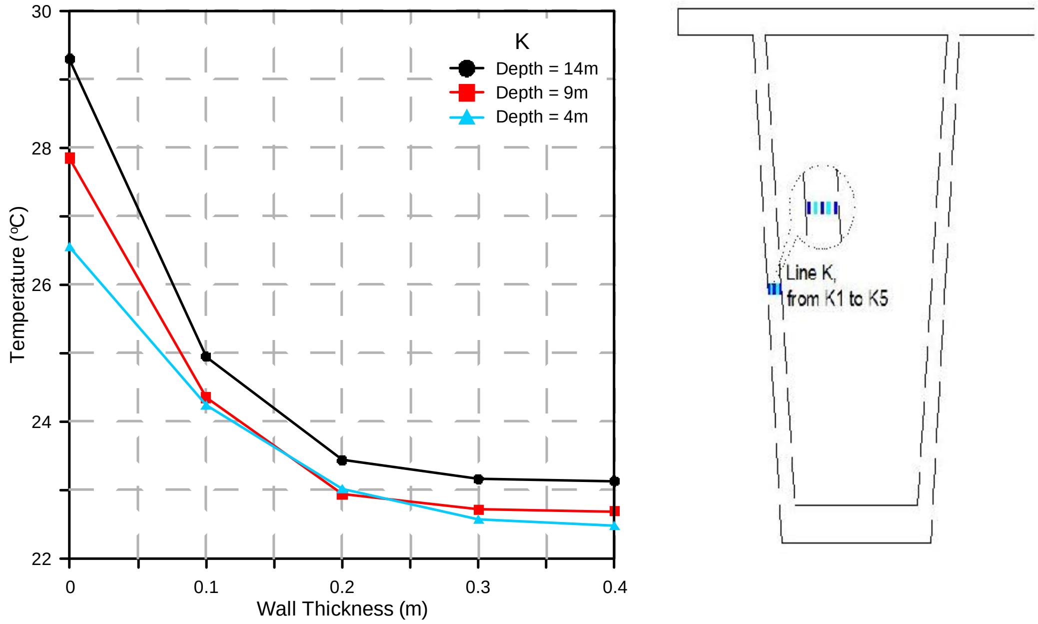

Figure 6.39 Transverse temperature distributions across the south web thickness for the three girder depths at 13.20

Figure 6.40 illustrates the maximum values of the transverse temperature gradient in the south wall for the three cross sections at 13:20. From the Figure it can be seen that the transverse temperature gradient was affected by changes made to the girder depth, where the decreasing the superstructure depth from 14 m to 9 m resulted in a reduction in the transverse temperature gradient from 6.17^{o}C to 5.16^{o}C. Therefore, the average gradient of temperature drop was about 0.19^{o}C /1m depth (3.3%^{o}C/1m depth) and then changed to about 0.22^{o}C/1m depth (4.3%^{o}C /1m depth), when the girder depth reduced from 9 m to4m. As a result, the average gradient of temperature drop was 0.21^{o}C/1m depth (3.8%^{o}C /1m depth) for the south web.

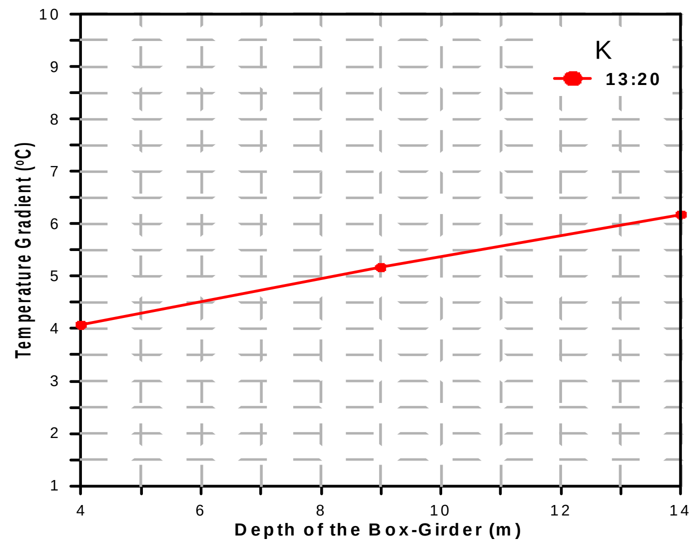

Figure 6.40 Maximum values of the transverse temperature gradient across the south web thickness for the three girder depths at 13.20

Figure 6.41 shows the transverse temperature distributions along the centerline of the bottom slab thickness for the three cross sections of the model at 06:40. From the Figure, it is clear that the effect of changing of the girder depth was slight on the surface temperature in the northern and the southern faces, while the effect of the web depth variations was negligible on the transverse temperature distributions along the axis of the bottom slab thickness.

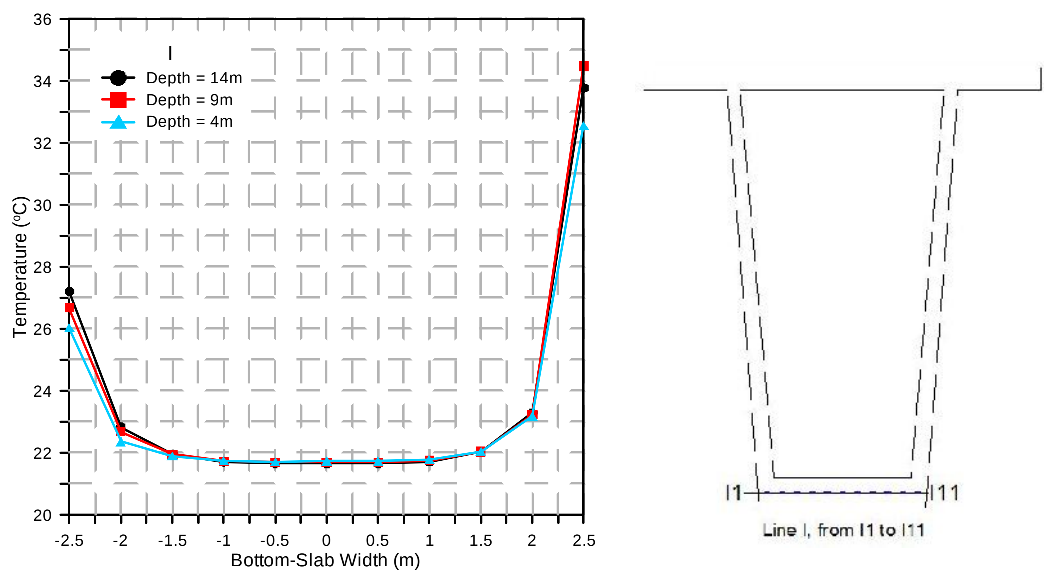

Figure 6.41 Transverse temperature distributions along the centerline of the bottom slab thickness for the three girder depths at 06:40

Figure 6.42 shows the maximum values of the transverse temperature gradient along the centerline of the bottom slab width for the three cross sections of the model at 06:40. As shown in the Figure the maximum transverse temperature gradient occurred at the cross section with web depth of 9 m with a value of approximately 12.8°C, while the maximum transverse thermal gradient for the deeper section was 12.13°C. Decreasing the girder depth from 9 m to 4 m resulted in a decrease in the thermal gradient until its value reached to approximately 10.8°C.

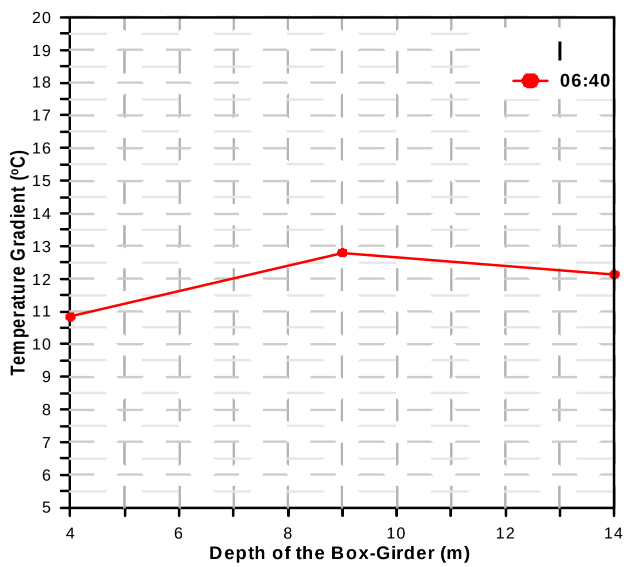

Figure 6.42 Maximum values of the transverse negative gradient along the centerline of the bottom slab thickness for the three cross sections of the FE model at 06:40

Figures 6.43 to 6.48 show the 3D temperature distribution along the depth for the three model sections at the time of maximum gradient.

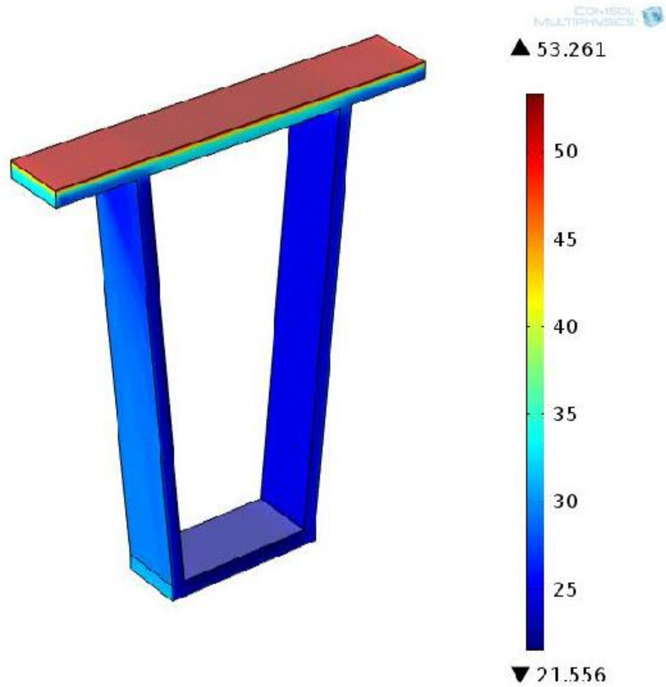

Figure 6.43 3D temperature distribution along the 14 m depth of the FE model section (time of maximum vertical gradient) at 13:20

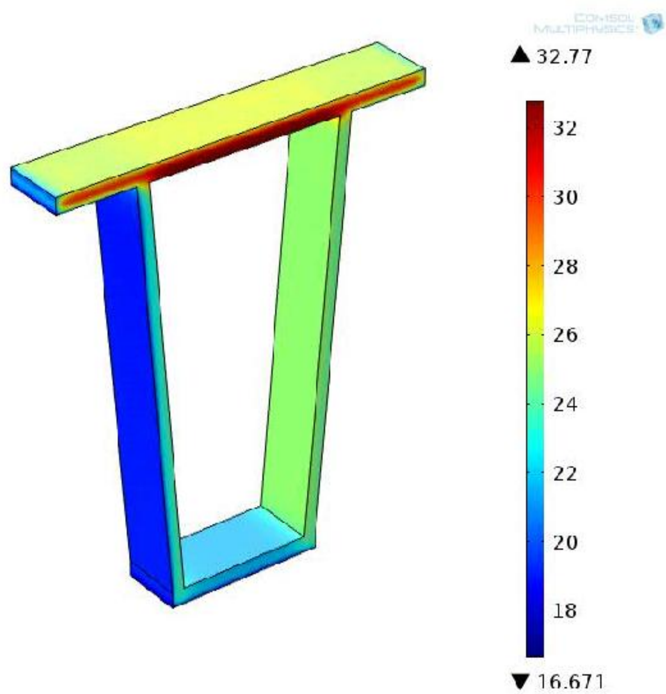

Figure 6.44 3D temperature distribution along the 14 m depth of the FE model section (time of maximum lateral negative gradient) at 05:40

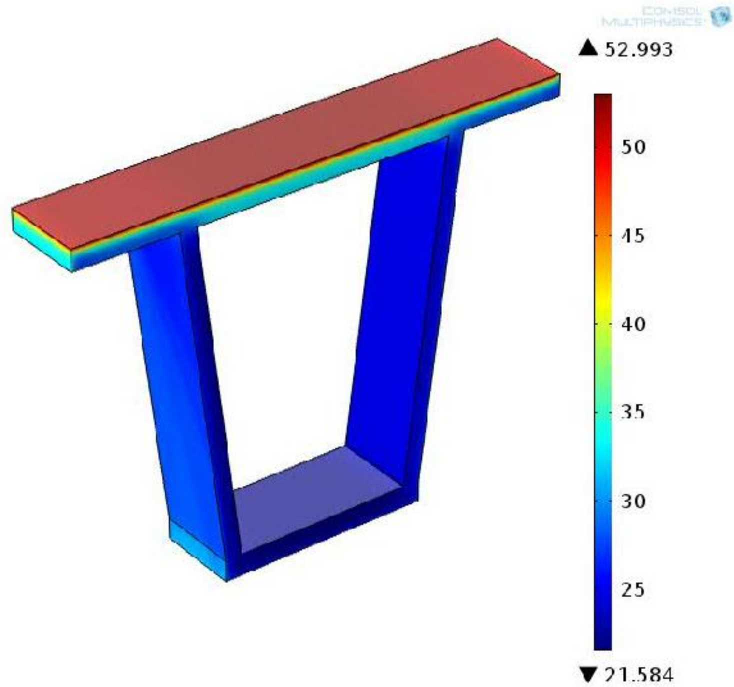

Figure 6.45 3D temperature distribution along the 9 m depth of the FE model section (time of maximum vertical gradient) at 13:20

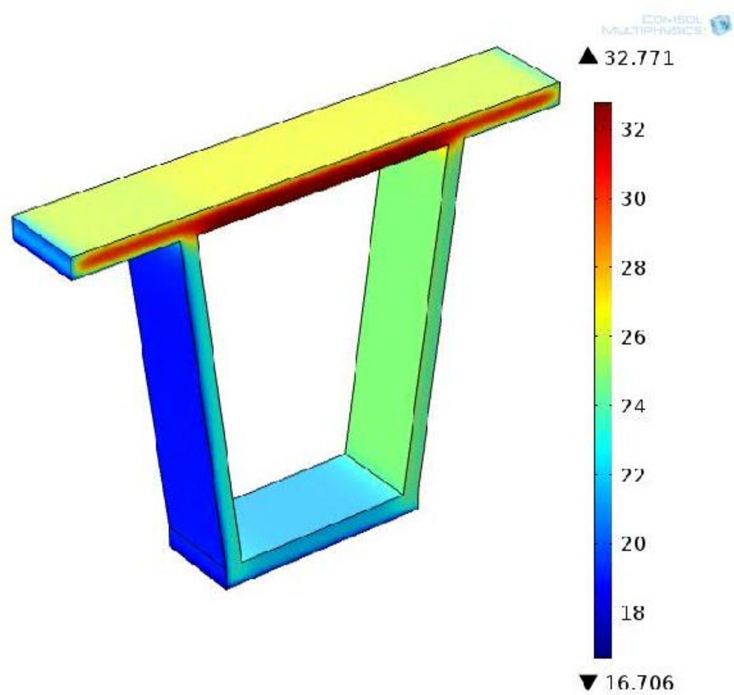

Figure 6.46 3D temperature distribution along the 9 m depth of the FE model section (time of maximum lateral negative gradient) at 05:40

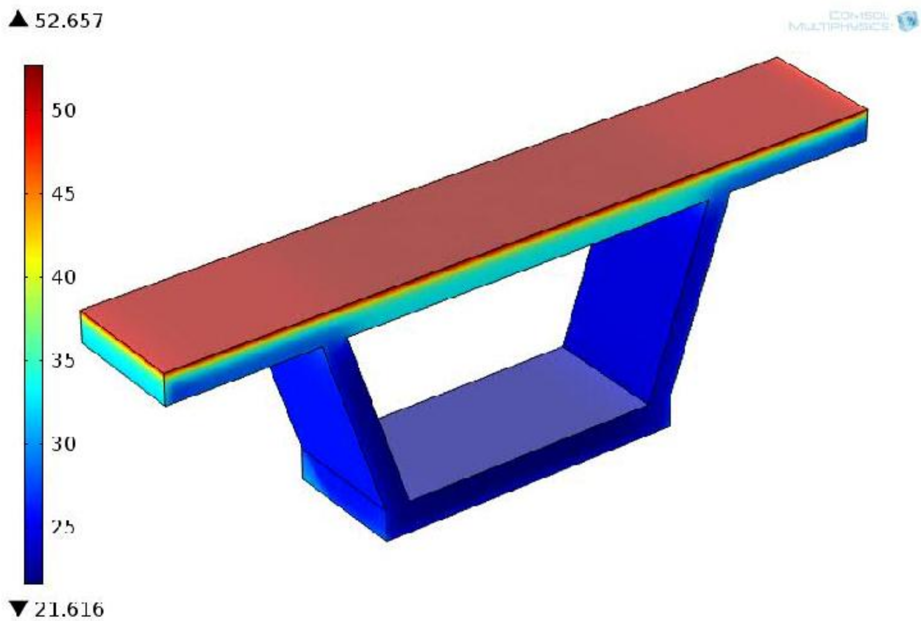

Figure 6.47 3D temperature distribution along the 4 m depth of the FE model section (time of maximum vertical gradient) at 13:20

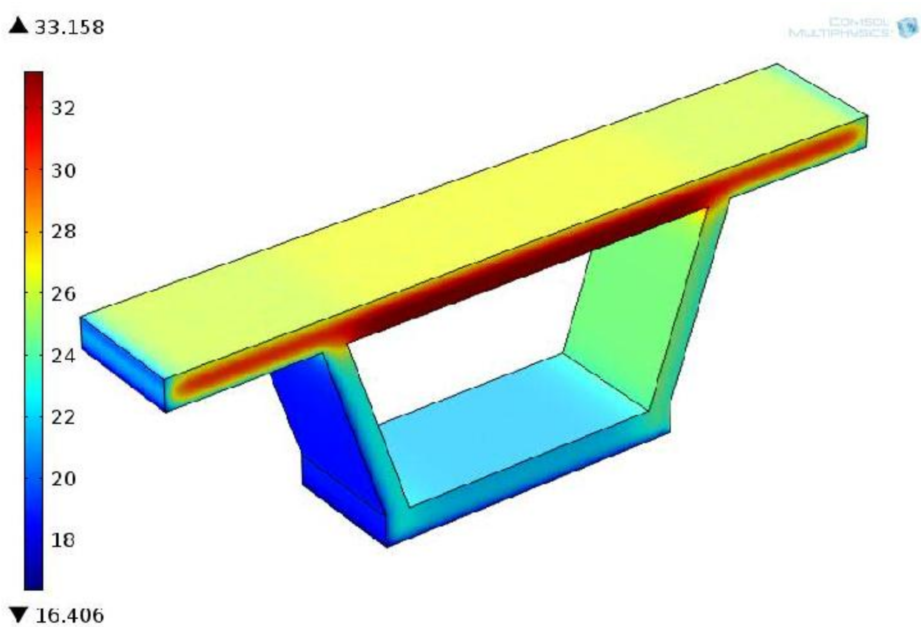

Figure 6.48 3D temperature distribution along the 4 m depth of the FE model section (time of maximum lateral negative gradient) at 05:40

CHAPTER 7

SUMMARY AND CONCLUSİONS

7.1 Summary

The heat conduction and the temperature distributions in deep concrete box-girder bridges were studied in this research using the FE method. External thermal loads including solar radiation and reflected radiation fluxes, surface convection cooling and surface re-radiation were considered in the thermal analysis. The FE model was verified with climate data and temperature measurements from an existing bridge and was used to study the temperature and the temperature gradient distributions in deep box-girder sections for the summer weather conditions of Gaziantep in Turkey.

7.2 Conclusions

The main conclusions of the current study are:

1- The proposed FE thermal analysis could simulate the heat budget of the real box-girder and predict concrete temperatures with high accuracy. The AAE between the predicted and the measured concrete temperatures along eight different groups across the top slab, the bottom slab and the webs were in the range of 0.12℃ to 1.1℃, while the MAE was less than 1.7℃ for all groups.

2- During the day, the temperature of the exterior surfaces increase due to the high solar radiation and the hot air temperature, while because of the weak thermal conductivity of concrete, the concrete interiors still cold which results in a positive temperature gradient with a maximum at the exterior surface. On the other hand, due to the convection cooling and the surface re-radiation, a negative temperature gradient occurs at the early morning hours with a minimum temperature at the exterior surface. The predicted maximum positive temperature gradients across the thickness of the centerlines of the top slab, the bottom slab, the south web and the north web for the case of the summer of Gaziantep were approximately 25℃, 6℃, 7℃ and 11℃, respectively.

3- Due to the daily movement of sun during the summer's days, the maximum lateral temperature gradients occur at the southern surfaces, while lower thermal gradients occur at the northern surfaces of both the top and the bottom slabs. Along the centerline of the top slab, the predicted maximum positive temperature gradients at the southern and northern edges were approximately 9℃ and 3℃, while the maximum negative gradients at the same points were approximately 5℃ and zero. On the other hand, the maximum positive gradients at the southern and northern edges for the centerline of the bottom slab were approximately 11℃ and 7℃.

4- For summer conditions of Gaziantep, the distribution of the maximum temperature gradient along the 14 m depth of the deep box-girder can be categorized into three different regions. The first region is a sharp nonlinear temperature decrease within the top 1 m. Followed by a region of a semi-constant temperature along the clear depth of web in addition to the top depth of the bottom slab, ending with the third region which extends along the lower 0.2 m of the bottom slab, within which the temperature shows a limited semi-linear increase.

5- The 3D FE thermal model was used to investigate the impact of bridge geometry on the temperature distributions and temperature gradients of concrete box-girders at time of maximum negative and positive gradient. The first geometrical parametric studies was the upper slab thickness, which has an important effect on the vertical temperature gradient across the top slab, where the average gradient of temperature drop was approximately 0.2^{o}C/1cm, while the effect of this parametric study on the vertical thermal gradient along the webs was negligible. The second parametric study shows that effect of the bottom slab thickness on the vertical thermal gradient across the bottom slab is still within the negligible range. The third parametric shows that the transverse negative gradient along the centerline of the top slab thickness was not affected by the changes made to the overhanging width of the top flange. In addition, the effect of the overhanging width on the thermal gradient across the North and the South webs was within a minor range at 13:40. While the effect of the fourth parametric study shows that the maximum thermal gradients along the South and the North webs were not affected by changes made to the girder depth. Moverover, the influence of this parametric on the transverse thermal gradient along the centerline of the top slab was very little. In addition, the effect of the girder depth on the the transverse thermal gradient along the centerline of the bottom slab width is still within the slight range at 06:40.

LIST OF REFERENCES

[1] Leonhardt, F. Kolbe, G. and Peter, J. (1965). Temperaturunterschiede gefahrden spannbetonbrucke (Temperature differences endanger prestressed concrete ridge, translated into English). *Beton-undStahlbetonbau*, *German*, **60**, pp. 157-163.

[2] Leonhardt, F. (1979). Risschaden an Betonbrucken-Ursachen und Abhilef (Crack damage to concrete bridge causes and remedies, translated into English), *Beton-und Stahlbetonbau, German*, **74** (2), pp. 36-44.

[3] Ghali, A., Favre, R. and Elbadry, M. (2002). Concrete structures: stresses and deformations (3rd ed.). London: Spon Press.

[4] Priestley, M. J. N. (1972). Temperature Gradients in Bridges-Some Design Consideration, New Zealand Engineering, 27, Part 7, pp. 228-233.

[5] Priestley, M. J. N. (1978). Design of Concrete Bridges for Temperature radients, American Concrete Institute Journal, 75, (23), pp. 209-217.

[6] Priestley, M. J. N. (1976). Design Thermal Gradients for Concrete Bridges, New Zealand Engineering, **31**, Part 9, pp. 213-219.

[7] Imbsen, R. A., Vandershaf, D. E., Schamber, R. A. and Nutt, R. V. (1985). Thermal Effects in Concrete Bridge Superstructures, National Cooperative Highway Research Program, Report 276, National Research Council, Washington.

[8] El-Alam, P. and Massicotte, B. (1994). Gradients Thermiques de Conception Pour le Pont de Grand-Mere, Rapport No. EPM/GCS-1994-01, Department de Genie Civil, Section Structures, Ecole Polytechnique, Montreal, Canada, Mont-real, Canada.

[9] Narouka. M. H., I. and Yamaguti, T. (1955). Measurement of the Temperature of the Interior of the Reinforced Concrete Slab of the Shigita Bridge and Presumtion of Thermal Stress, Symposium of the Stress Measurements for Bridge and Structures, Japanese Society for the Promotion of Science, Proc., Tokyo, Japan.

[10] Barber, E. S. (1957). Calculations of Maximum Pavement Temperatures from Weather Reports, Highway Research Board Bulletin 168, pp. 1-8.

[11] Zuk,W. (1965). Thermal Behavior of Composite Bridges Insulated and Uninsula- ted, Highway Research Record 76, National Research Council, pp. 231-253.

[12] Maher, D. R. H. (1970). The effect of Differential Temperature on Continuous Prestresses Concrete Bridges, *Civil Engineering Transaction*, **12**, Part l, pp. 29-32.

[13] New Zealand Ministry of Works and Developments. (1970). Bridge Design Tem- perature Gradient, New Zealand, Wellington.

[14] Emerson, M. (1973). The Calculation of the Distribution of Temperature in Bridges, TRRL Laboratory Report 561, Department of the Environment, Crowthome, Berkshire, England.

[15] Lanigan, A. G. (1973). The Temperature Response of Concrete Box-Girder Bridges, Ph.D. Thesis, Report No. 94, School of Engineering, University of Auckland, Auckland, New Zealand.

[16] Reynolds, J. and Emanuel, J. H. (1974). Thermal Stresses and Movements in Bridges, *Journal of the Structural Engineering*, **100**, pp. 63-78.

[17] Radolli, M. and Green, R. (1975). ThermalStressesin Concrete Bridge Super-structures under Summer Conditions, Transportation Research Record 547, Transportation Research Board.

[18] Hunt B. and Cooke, N. (1975). Thermal Calculations for Bridge Design, *Journal of Structural*, **101**, ST9, pp. 1763-1781.

[19] Hambly, E., (1978). Temperature Distributions and Stresses in Concrete Bridges, *The Structural Engineer*, **56A**, (5), pp. 143 - 148.

[20] Emerson, M. (1979). Bridge Temperature for Setting Bearings and Expansions Joints, TRRL Supplementary Report, No. 479, Department of the Environment, Department of Transport, Crowthome, Berkshire, England.

[21] Dilger, W. H. and Ghali, A. (1980). Temperature-Induced Stresses in Composite Box-Girder Bridges, Research Report Submitted to the Department of Supplies and Services, Ottawa, Canada.

[22] Elbadry, M. M. and Ghali, A. (1983b). Nonlinear Temperature Distribution and its Effects on Bridges, ETH-Honggerberg, Zurich, Switzerland. IABSE Peridica 3/1983, No. P66/83, pp. 169-191.

[23] Elbadry, M. M. and Ghali, A. (l983a). Temperature Variations in Concrete Bridges, *Journal of Structural Engineering*, **109**, (10), pp. 2355-2374.

[24] Dilger, W. H., Ghali, A., Cheung, M. S. and Maes, M. (1983). Temperature Stresses in Composite Box Girder Bridges, *Journal of the Structural Engineering*, **109**, (6), pp. 1460-1478.

[25] Clark. H. (1989). Evaluation of Thermal Stresses in a Concrete Box Girder Bridge, Ph.D. thesis, University of Washington, United States.

[26] Hirst, M. J. S. and Dilger, W. H. (1989). Prediction of Bridge Temperatures, ETH-Honggerberg, Zurich, Switzerland. IABSE Peridica, No. P66/83.

[27] Elbadry, M. M. and Ghali, A. (1982). User's Manual and Computer Program FETAB: Finite Element Thermal Analysis of Bridges, Research Report No. CE82-10, Department of Civil Engineering, The University of Calgary, Calgary, Alberta.

[28] Potgieter, I.C. and Gamble, W. L. (1989). Nonlinear temperature distribution in bridges at different locations in the United States, *PCI Journal*, pp. 80- 103.

[29] Mirambell, E.Aguado, A. (1990). Temperature and stress distributions in concrete box girder bridges, *Journal of Structural Engineering*, **116**, (9), pp. 2388- 2409.

[30] Waldron, P., Ramezankhani, M. and Woodman, N. (1990). Differential Temperature Effects in Concrete Box Girder Bridges, içinde Proceedings of the 3rd International Conference on Developments in Short and Medium Span Bridge Engineering 90, Toronto, Canada.

[31] Fu, H., Ng, S. and Cheung, M. (1990). Thermal Behavior of Composite Bridges, *Journal of Structural Engineering*, **116**, (12), pp. 3302-3323.

[32] Branco, F.A. and Mendes, P.A. (1993). Thermal actions for concrete bridge, *Journal of Structural Engineering,* **199**, 9, pp. 2313-2331.

[33] Molesini, P. and Massicotte, B. (1993). Thermal Behaviour Modeling of a Deep Concrete Box Girder Bridge, içinde Canadian Society for Civil Engineering Annual Conference Proceedings, June 8-11, 1993.

[34] Saetta, A., Scona, R. and Vitaliani R. (1995). Stress Analysis of Concrete Structures Subjected to Variable Thermal Loads, *Journal of Structural Engineering*, **121**, (3), pp. 446-457.

[35] Al-Kerwi, Z. N. R. (2000). Thermal Loading and Stresses in Reinforced concrete Bridge Decks, M.Sc Thesis, Iraq, Baghdad, University of Nahrain.

[36] Barber, E. S. (1957). Calculations of Maximum Pavement Temperatures from Weather Reports, Highway Research Board Bulletin **168**, pp. 1-8.

[37] Jun Suzuki, Yoshito Ohba, Yoshiyuki Uchikawa, Kazutoshi Hoshikawa and Kazuhiro Kimura. (2007). Monitoring Temperatures on a Real Box-Girder Bridge and Energy Budget Analysis for Basic Information on Bridge Cooling and Surface Freezing, *Journal of Bridge Engineering*, **12,** (1), no. 1084-0702, pp. 45-52.

[38] Wang, J. and Fang, Z. (2009). Temperature Variation of Concrete Box Girder Bridge, *Front. Archit. Civ. Eng.*, **4**, pp. 407-413.

[39] Larsson, O. (2009). Modelling of temperature profiles in a concrete slab under climatic exposure, *Structural concrete*, **10**, pp. 193-201.

[40] Wang, B.,Wang, W. and Zeng, X. (2010). Measurements and Analysis of Temperature Effects on Box Girders of Continuous Rigid Frame Bridges, *World Academy of Science, Engineering and Technology*, **70**, pp. 732-738.

[41] Jong-Han Lee and llker Kalkan. (2012). Analysis of Thermal Environmental Effects on Precast, Prestressed Concrete Bridge Girders: Temperature Differentials and Thermal Deformations, *Advances in Structural Engineering*, **15**, pp. 447-459.

[42] Larsson, O. and Thelandersson, S. (2011). Estimating Extreme Values of Thermal Gradients in Concrete Structures, Material and Structures, 44, pp. 1491-1500.

[43] Jong-Han Lee. (May 2012). Investigation of Extreme Environmental Conditions and Design Thermal Gradients during Construction for Prestressed Concrete Bridge Girders, *Journal of Bridge Engineering*, **17**, (3), pp. 547-556.

[44] Zhang, L., Wu, L. and Yang, L. (2012). Analysis of Temperature Field of Concrete Box Girder and Secondary Development of Program, *Journal of Convergence Information Technology,* **7.**

[45] Carboni, B. and Lacarbonara, W. (2012). A Three-Dimensional Continuum Approach to The Thermoelastodynamics of Large Scale Structures, *Engineering Structures*, **40,** pp. 155-167.

[46] Emerson, M. (1968). Bridge temperature movements in the British Isles, TRRL Report No LR.228, Transport and Road Research Laboratory, England.

[47] Emerson, M. (1977).Temperature differences in bridges: basis of design equire-ments,TRRL Report No LR 765, Transport and Road Research Laboratory, England.

[48] Roberts-Wollman, C.L., Breen, J.E. and Cawrse, J. (2002, May). Measurements of thermal gradients and their effects on segmental concrete bridge, *Journal of Bridge Engineering*, **27**, (3), pp. 166-174.

[49] AASHTO. (1989). AASHTO Guide specifications: Thermal effects in concrete bridge superstructures, Washington, DC: American Association of State highway and Transportation Officials.

[50] AASHTO. (2007). AASHTO LRFD bridge design specifications: 2008 interim revisions (4th ed.), Washington, DC: American Association of State Highway and Transportation Officials.

[51] Emanuel, J. H. and Hulsey, J. L. (1978) Temperature Dismbutions in Composite Bridges, *Journal of the Srmctural Divisiorl*, **104**, pp. 65-78.

[52] Ibrahim, A. M. M. (1995). Three-Dimensional Thermal Analysis of Curved Con- crete Box Girder Bridges, Master’s Thesis, Concordia University.

[53] Kehlbeck F. (1975). Effect of solar radiation on bridge structures, Technical University of Hannover, Werner-Verlag, Dusseldorf. In German.

[54] Mendes, Pedro António Martins. (1989). Thermal Action in concrete bridges, Lisbon: Instituto Superior Técnico.

[55] Silveira, António Paulo Campos. (1996). The influence of thermal actions on the behavior of reinforced concrete bridges and prestressed, Lisbon, LNEC.

[56] COMSOL Multiphysics v 4.3a. (2012). Heat Transfer Module User's Guide, Stockholm, Sweden.

[57] Sveinson, T.N. (2004). Temperature effects in concrete box girder bridges, PhD Thesis, University of Calgary, Canada.

[58] Priestly, M. J. N. and Buckle, I.G. (1979). Ambient Thermal Response of Concrete Bridges, Road Research Unit Bulletin 42, National Roads Research Board, New Zealand State Highways, Wellington.

[59] Emerson, M. (1982). Influence of environment on concrete bridge temperatures, Comite' Euro-International du Beton, Bulletin d'lnformation, No 154. In German.